Applied Computational Electromagnetics Society

Journal

July 2013 Vol. 28 No. 7

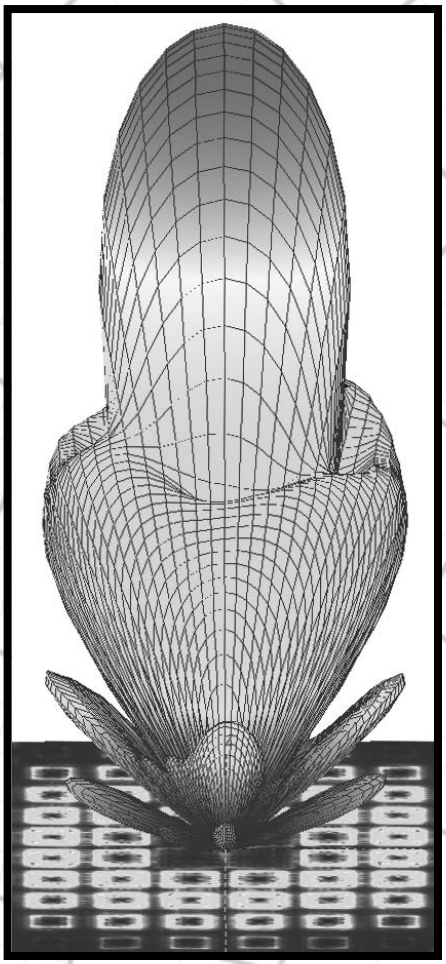

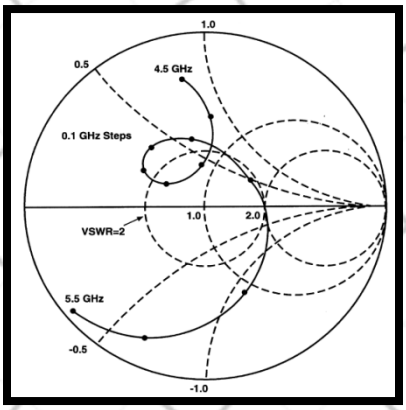

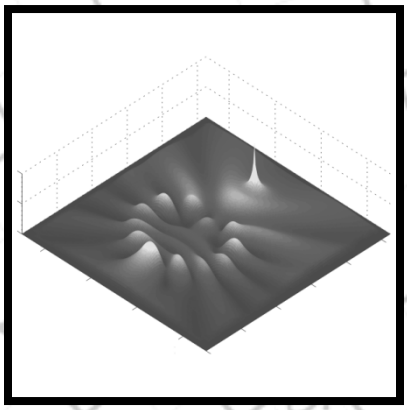

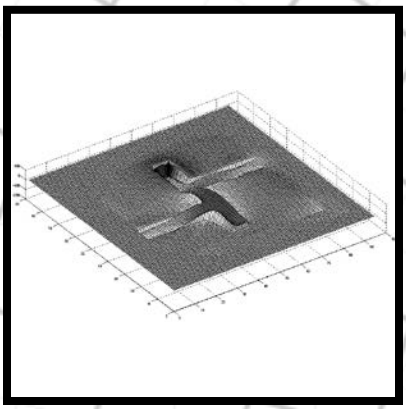

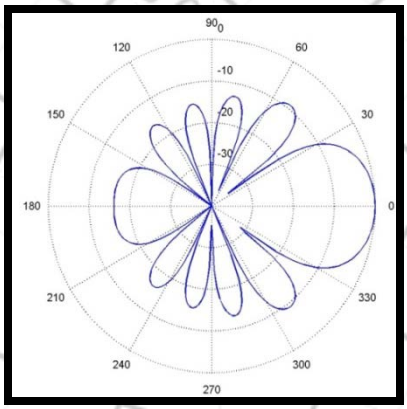

ISSN 1054-4887

GENERAL PURPOSE AND SCOPE: The Applied Computational Electromagnetics Society ***(ACES)*** Journal hereinafter known as the ***ACES Journal*** is devoted to the exchange of information in computational electromagnetics, to the advancement of the state-of-the art, and the promotion of related technical activities. The primary objective of the information exchange is to inform the scientific community on the developments of new computational electromagnetics tools and their use in electrical engineering, physics, or related areas. The technical activities promoted by this publication include code validation, performance analysis, and input/output standardization; code or technique optimization and error minimization; innovations in solution technique or in data input/output; identification of new applications for electromagnetics modeling codes and techniques; integration of computational electromagnetics techniques with new computer architectures; and correlation of computational parameters with physical mechanisms.

SUBMISSIONS: The ***ACES Journal*** welcomes original, previously unpublished papers, relating to applied computational electromagnetics. Typical papers will represent the computational electromagnetics aspects of research in electrical engineering, physics, or related disciplines. However, papers which represent research in applied computational electromagnetics itself are equally acceptable.

Manuscripts are to be submitted through the upload system of ***ACES*** web site http://www.aces-society.org See "Information for Authors" on inside of back cover and at ***ACES*** web site. For additional information contact the Editor-in-Chief:

Dr. Atef Elsherbeni
Department of Electrical Engineering
The University of Mississippi
University, MS 386377 USA
Phone: 662-915-5382
Email: atef@olemiss.edu

SUBSCRIPTIONS: All members of the Applied Computational Electromagnetics Society are entitled to access and download the ***ACES Journal*** any published journal article available at http://www.aces-society.org. Printed issues of the ***ACES Journal*** are delivered to institutional members. Each author of published papers receives a printed issue of the ***ACES Journal*** in which the paper is published.

Back issues, when available, are $50 each. Subscription to ***ACES*** is through the web site. Orders for back issues of the ***ACES Journal*** and change of address requests should be sent directly to ***ACES*** office at:

Department of Electrical Engineering
The University of Mississippi
University, MS 386377 USA

Allow four weeks advance notice for change of address. Claims for missing issues will not be honored because of insufficient notice, or address change, or loss in the mail unless the ***ACES*** office is notified within 60 days for USA and Canadian subscribers, or 90 days for subscribers in other countries, from the last day of the month of publication. For information regarding reprints of individual papers or other materials, see "Information for Authors".

LIABILITY. Neither ***ACES***, nor the ***ACES Journal*** editors, are responsible for any consequence of misinformation or claims, express or implied, in any published material in an ***ACES Journal*** issue. This also applies to advertising, for which only camera-ready copies are accepted. Authors are responsible for information contained in their papers. If any material submitted for publication includes material which has already been published elsewhere, it is the author's responsibility to obtain written permission to reproduce such material.

APPLIED COMPUTATIONAL ELECTROMAGNETICS SOCIETY JOURNAL

July 2013
Vol. 28 No. 7
ISSN 1054-4887

The ACES Journal is abstracted in INSPEC, in Engineering Index, DTIC, Science Citation Index Expanded, the Research Alert, and to Current Contents/Engineering, Computing & Technology.

The illustrations on the front cover have been obtained from the research groups at the Department of Electrical Engineering, The University of Mississippi.

JULY 2013 REVIEWERS

Ahmed Abdelrahman
Iftikhar Ahmed
Saad Alhossin
Mohamed Al-Sharkaway
Rodolfo Araneo
Aghogho Atemu
Abdul Ali Babar
Sami Barmada
Ahmed Boutejdar
Hamid Erfani
Ahmad Hosseinbeig
Jerome Glaser
Jamie Infantolino
Darko Kajfez
Albert Lysko
Mahesh Babu Narra
Lotfi Osman
Yasuhiro Tsunemitsu
Qianyin Xiang
Shaoqiu Xiao
Qiaoli Zhang

THE APPLIED COMPUTATIONAL ELECTROMAGNETICS SOCIETY

JOURNAL

Vol. 28 No. 7 July 2013

TABLE OF CONTENTS

Frequency-Domain Solution to Electromagnetic Scattering from Dispersive Chiroferrite Materials

Moamer Hasanovic, Chong Mei, Jay K. Lee, and Ercument Arvas

Department of Electrical Engineering and Computer Science
Syracuse University, Syracuse, NY 13244, USA
mhasanov@syr.edu, cmei@syr.edu, leejk@syr.edu, earvas@syr.edu

Abstract ─ Main purpose of this paper is to present a solution to electromagnetic scattering by bianisotropic dispersive materials. The presented solutions provide a reference baseline that can be used for comparison reasons by other researchers dealing with scattering by bianisotropic dispersive media. The solution algorithm based on the method of moments and mixed potential equations is tested through a few cases of dispersive scatterers and first known solutions to these problems are obtained. The proposed method has an advantage over the time domain methods as it does not rely on the Z-transform of the analytical expressions necessary to be used when dispersive media are present in the problem of interest.

Index Terms ─ Chiral, chiroferrite, dispersive, electromagnetic scattering, ferrite, and method of moments.

I. INTRODUCTION

Dispersive materials belong to the category of bianisotropic media, for which the following constitutive relations apply,

$$\begin{aligned} \overline{D} &= \overline{\overline{\varepsilon}} \cdot \overline{E} + \overline{\overline{\xi}} \cdot \overline{H} \\ \overline{B} &= \overline{\overline{\zeta}} \cdot \overline{E} + \overline{\overline{\mu}} \cdot \overline{H}, \end{aligned} \tag{1}$$

where $\overline{\overline{\varepsilon}}$ is the permittivity tensor, $\overline{\overline{\mu}}$ is the permeability tensor, and $\overline{\overline{\xi}}$ and $\overline{\overline{\zeta}}$ are the magnetoelectric tensors. In this paper, the overbar "–" denotes a vector and the double overbar "=" denotes a tensor.

Let us consider an inhomogeneous bianisotropic body of arbitrary three-dimensional shape characterized by the constitutive relations shown in equation (1). As shown in Fig. 1, if the body is illuminated by a time-harmonic electromagnetic wave with $e^{j\omega t}$ dependence, the fields in the body are described by Maxwell's equations as,

$$\begin{aligned} \nabla \cdot \overline{E} &= \frac{\rho_{eb}}{\varepsilon_0} \\ \nabla \cdot \overline{H} &= \frac{\rho_{mb}}{\mu_0}, \\ \nabla \times \overline{E} &= -j\omega\mu_0 \overline{H} - \overline{J}_{mp}, \\ \nabla \times \overline{H} &= j\omega\varepsilon_0 \overline{E} + \overline{J}_{ep}, \end{aligned} \tag{2}$$

where $\overline{J}_{ep}$ and $\overline{J}_{mp}$ are the electric and magnetic polarization currents, and ρ_{eb} and ρ_{mb} are electric bound charges and magnetic bound charges, respectively, that can be related to the electric and magnetic polarizations as given in [1].

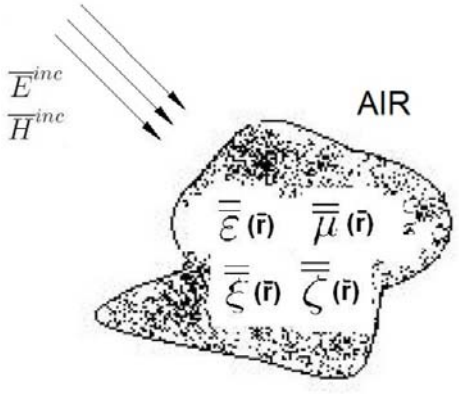

Fig. 1. Inhomogeneous bianisotropic body in free space illuminated by an electromagnetic wave.

Submitted On: Jan. 28, 2013
Accepted On: Apr. 13, 2013

Separating the total fields into the incident field component $\left(\overline{E}^{inc}, \overline{H}^{inc}\right)$ produced by the primary sources and the scattered component $\left(\overline{E}^{s}, \overline{H}^{s}\right)$ produced as a result of scattering from the bianisotropic body, and then introducing the magnetic vector potential $\overline{A}$, the electric scalar potential V, the electric vector potential $\overline{F}$, and the magnetic scalar potential U, the total fields can be written as in [1],

$$\begin{aligned} \overline{E} &= \overline{E}^{inc} - j\omega\overline{A} - \nabla V - \frac{1}{\varepsilon_0}\nabla \times \overline{F} \\ \overline{H} &= \overline{H}^{inc} - j\omega\overline{F} - \nabla U + \frac{1}{\mu_0}\nabla \times \overline{A}. \end{aligned} \tag{3}$$

The surface integrals can be calculated as follows,

$$\overline{A} = \mu_0 \int_V \overline{J}_{ep}(\overline{r}')G(\overline{r},\overline{r}')dv' \tag{4}$$

$$\begin{aligned} V &= \frac{1}{\varepsilon_0}\int_V \rho_{eb}(\overline{r}')G(\overline{r},\overline{r}')dv', \\ &+ \frac{1}{\varepsilon_0}\int_V \sigma_{eb}(\overline{r}')G(\overline{r},\overline{r}')ds', \end{aligned} \tag{5}$$

$$\overline{F} = \varepsilon_0 \int_V \overline{J}_{mp}(\overline{r}')G(\overline{r},\overline{r}')dv', \tag{6}$$

$$\begin{aligned} U &= \frac{1}{\mu_0}\int_V \rho_{mb}(\overline{r}')G(\overline{r},\overline{r}')dv', \\ &+ \frac{1}{\mu_0}\int_V \sigma_{mb}(\overline{r}')G(\overline{r},\overline{r}')ds'. \end{aligned} \tag{7}$$

If the unknown quantities $\overline{E}$ and $\overline{H}$ in the constructed integral equations are expressed in terms of $\overline{D}$ and $\overline{B}$, and then RWG basis functions [2, 3] and Galerkin's method are used. Equations (3) and (4) can be transformed into the system of linear equations,

$$\begin{bmatrix} (C_{mn}) & (Y_{mn}) \\ (Z_{mn}) & (A_{mn}) \end{bmatrix} \cdot \begin{bmatrix} (D_n) \\ (B_n) \end{bmatrix} = \begin{bmatrix} (E_m) \\ (H_m) \end{bmatrix}, \tag{8}$$

where Z_{mn}, A_{mn}, C_{mn}, and Y_{mn} are N by N matrices and D_n, B_n, E_n, and H_n are N dimensional vectors. The detailed analytical expressions for matrix elements Z_{mn}, A_{mn}, C_{mn}, and Y_{mn} are given in [1].

II. DISPERSIVE PROPERTIES OF FERRITE AND CHIRAL MEDIA

Although obtaining the analytical expressions of the material dispersion is not required by this method, the dispersion properties of the ferrites and chiral media are still given, in case researchers need to solve the problems in a time domain method for comparison in the future [4]. When the expressions modeled from the real world are evaluated, the constitutive parameters assigned to the material have some physical meaning.

When biased by a DC magnetic field $\overline{B}_0 = \hat{z}B_0$, ferrite materials, whose permittivity tensor $\overline{\overline{\varepsilon}} = \varepsilon_0 \overline{\overline{I}}$, are characterized by their permeability tensors $\overline{\overline{\mu}} = \mu_0 \overline{\overline{\mu}}_r$ where,

$$\overline{\overline{\mu}}_r = \begin{bmatrix} \mu_1 & j\mu_2 & 0 \\ -j\mu_2 & \mu_1 & 0 \\ 0 & 0 & \mu_3 \end{bmatrix}. \tag{9}$$

The elements in the permeability tensor are formulated as in [5],

$$\begin{aligned} \mu_1 &= 1 + \frac{\left(\omega_0 + j\omega\alpha\right)\omega_m}{\left(\omega_0 + j\omega\alpha\right)^2 - \omega^2} \\ \mu_2 &= \frac{\omega\,\omega_m}{\left(\omega_0 + j\omega\alpha\right)^2 - \omega^2} \\ \mu_3 &= 1, \end{aligned} \tag{10}$$

where α is the ferrite damping factor, ω_0 is the Larmor precession frequency and ω_m is the saturation magnetization frequency.

The Larmor precession frequency ω_0 and the saturation magnetization frequency ω_m are determined by the DC magnetic field bias by,

$$\begin{aligned} \omega_0 &= \gamma_m H_0 \\ \omega_m &= \gamma_m M_0, \end{aligned} \tag{11}$$

where γ_m is the gyromagnetic ratio, H_0 is the magnitude of the applied DC magnetic field, and M_0 is the magnitude of saturated magnetization vector. $\overline{M}_0$ is in the same direction as the applied magnetic field $\overline{H}_0$.

Once the Larmor precession frequency, saturation magnetization frequency, and ferrite damping factor are given, the permeability tensor

$\overline{\overline{\mu}}$ can be evaluated at any frequency. For example, if we consider a ferrite material with the parameters of $\alpha = 0.1, \omega_0 = 2\pi \times 2 \times 10^9$, and $\omega_m = 2\pi \times 2 \times 10^9$, we have, at 0.4 GHz,

$$\overline{\overline{\mu}}_r = \begin{bmatrix} 2.0412 - 0.0226j & 0.0087 + 0.2081j & 0 \\ -0.0087 - 0.2081j & 2.0412 - 0.0226j & 0 \\ 0 & 0 & 1 \end{bmatrix},$$

at 0.6 GHz,

$$\overline{\overline{\mu}}_r = \begin{bmatrix} 2.0974 - 0.0394j & 0.0217 + 0.3286j & 0 \\ -0.0217 - 0.3286j & 2.0974 - 0.0394j & 0 \\ 0 & 0 & 1 \end{bmatrix},$$

at 1 GHz,

$$\overline{\overline{\mu}}_r = \begin{bmatrix} 2.3231 - 0.1101j & 0.0879 + 0.6571j & 0 \\ -0.0879 - 0.6571j & 2.3231 - 0.1101j & 0 \\ 0 & 0 & 1 \end{bmatrix},$$

and at 1.2 GHz,

$$\overline{\overline{\mu}}_r = \begin{bmatrix} 2.5346 - 0.1951j & 0.1717 + 0.9104j & 0 \\ -0.1717 - 0.9104j & 2.5346 - 0.1951j & 0 \\ 0 & 0 & 1 \end{bmatrix}.$$

The constitutive equations for dispersive chiral media can be written as,

$$\begin{aligned} \overline{D}(\omega) &= \varepsilon(\omega)\overline{E}(\omega) - j\kappa(\omega)\sqrt{\varepsilon_0\mu_0}\,\overline{H}(\omega) \\ \overline{B}(\omega) &= \mu(\omega)\overline{H}(\omega) + j\kappa(\omega)\sqrt{\varepsilon_0\mu_0}\,\overline{E}(\omega). \end{aligned} \tag{12}$$

In most of the cases, the Lorentz model is used to characterize the dispersive nature of permittivity and permeability. The Condon model is generally used to describe the dispersive nature of chirality [6]. The Lorentz model is in the form,

$$\begin{aligned} \varepsilon(\omega) &= \varepsilon_\infty + \frac{(\varepsilon_s - \varepsilon_\infty)\omega_\varepsilon^{\,2}}{\omega_\varepsilon^{\,2} - \omega^2 + j2\omega_\varepsilon\xi_\varepsilon\omega} \\ \mu(\omega) &= \mu_\infty + \frac{(\mu_s - \mu_\infty)\omega_\mu^{\,2}}{\omega_\mu^{\,2} - \omega^2 + j2\omega_\mu\xi_\mu\omega}. \end{aligned} \tag{13}$$

The Condon model is in the form,

$$\kappa(\omega) = \frac{\tau_\kappa\omega_\kappa^{\,2}\,\omega}{\omega_\kappa^{\,2} - \omega^2 + j2\omega_\kappa\xi_\kappa\omega}. \tag{14}$$

If a chiral material with the following parameters is considered,

$$\begin{aligned} &\varepsilon_\infty = 2\varepsilon_0;\ \varepsilon_s = 5\varepsilon_0 \\ &\omega_\varepsilon = 2\pi \times 2 \times 10^9;\ \xi_\varepsilon = 0.5 \\ &\mu_\infty = 1.1\mu_0;\ \mu_s = 1.8\mu_0 \\ &\omega_\mu = 2\pi \times 2 \times 10^9;\ \xi_\mu = 0.5 \\ &\tau_\kappa = \frac{0.5}{\omega_\kappa};\ \omega_\kappa = 2\pi \times 2 \times 10^9;\ \xi_\kappa = 0.3, \end{aligned} \tag{15}$$

the constitutive parameters can be evaluated at different frequencies. We have, at 0.4 GHz,

$\varepsilon_r = 4.9950 - 0.6240j$; $\mu_r = 1.7988 - 0.1456j$; $\kappa = 0.1026 - 0.0128j$,

at 0.6 GHz,

$\varepsilon_r = 4.9735 - 0.9803j$; $\mu_r = 1.7938 - 0.2287j$; $\kappa = 0.1586 - 0.0314j$,

at 1 GHz,

$\varepsilon_r = 4.7692 - 1.8462j$; $\mu_r = 1.7462 - 0.4308j$; $\kappa = 0.2874 - 0.1149j$,

and at 1.2 GHz,

$\varepsilon_r = 4.4948 - 2.3389j$; $\mu_r = 1.6821 - 0.5457j$; $\kappa = 0.3561 - 0.2003j$.

In following sections, we will investigate the scattering fields that involve the mixtures of the ferrite and the chiral materials using the above evaluated constitutive parameters.

III. DISPERSIVE HOMOGENIZED CHIROFERITE SPHERE

When equal volume of a ferrite material and a chiral material are mixed homogeneously, although currently there is no analytic model for the constitutive parameters of such a mixture, as an engineering approximation, one may assume that the material can be described on a macroscopic scale by the constitutive parameters,

$$\overline{\overline{\varepsilon}} = \frac{1}{2}\left(\overline{\overline{\varepsilon}}_{ferrite} + \overline{\overline{\varepsilon}}_{chiral}\right), \overline{\overline{\mu}} = \frac{1}{2}\left(\overline{\overline{\mu}}_{ferrite} + \overline{\overline{\mu}}_{chiral}\right),$$

$$\overline{\overline{\xi}} = \frac{1}{2}\left(\overline{\overline{\xi}}_{ferrite} + \overline{\overline{\xi}}_{chiral}\right), \overline{\overline{\varsigma}} = \frac{1}{2}\left(\overline{\overline{\varsigma}}_{ferrite} + \overline{\overline{\varsigma}}_{chiral}\right),$$

where $\overline{\overline{\varepsilon}}_{chiral}$, $\overline{\overline{\mu}}_{chiral}$, $\overline{\overline{\xi}}_{chiral}$, and $\overline{\overline{\varsigma}}_{chiral}$ are the constitutive tensors for the chiral material, and

$\bar{\bar{\varepsilon}}_{ferrite}$, $\bar{\bar{\mu}}_{ferrite}$, $\bar{\bar{\xi}}_{ferrite}$, and $\bar{\bar{\zeta}}_{ferrite}$ are the constitutive tensors for ferrite material. Again, it is important to stress that the approximation proposed above does not have any physical or practical meaning but it is merely introduced here to test the validity of the proposed solution in the absence of a real-world material of chiroferrite nature.

For the chiral material, we have $\bar{\bar{\varepsilon}}_{chiral} = \varepsilon_0 \varepsilon_{r,chiral} \bar{\bar{I}}$, $\bar{\bar{\mu}}_{chiral} = \mu_0 \mu_{r,chiral} \bar{\bar{I}}$, $\bar{\bar{\xi}}_{chiral} = -j\kappa\sqrt{\varepsilon_0 \mu_0}\,\bar{\bar{I}}$, and $\bar{\bar{\zeta}}_{chiral} = j\kappa\sqrt{\varepsilon_0 \mu_0}\,\bar{\bar{I}}$ where $\varepsilon_{r,chiral}$ is the relative permittivity of the chiral material, $\mu_{r,chiral}$ is the relative permeability of the chiral medium, and κ is the chirality parameter of the chiral material.

For the ferrite material, we have $\bar{\bar{\varepsilon}}_{ferrite} = \varepsilon_0 \bar{\bar{I}}$, $\bar{\bar{\mu}}_{ferrite} = \mu_0 \mu_{r,ferrite}$, and $\bar{\bar{\xi}}_{ferrite} = \bar{\bar{\zeta}}_{ferrite} = 0$, where $\bar{\bar{\mu}}_{r,ferrite}$ is the relative permeability tensor of the ferrite material. Mixing homogeneously the chiral material and ferrite material mentioned in section II, the corresponding macroscopic constitutive parameters of the chiroferrite material can be evaluated at any frequency.

This section presents the results of scattering from such a dispersive homogenized chiroferrite sphere shown in Fig. 2. The sphere is of radius R = 7.2 *cm* and is illuminated by a plane electromagnetic wave propagating in the z direction, which has the electric field component in the x direction, i.e., $\bar{E}^{inc} = \hat{x} E^{inc} e^{-jk_0 z}$ and $\bar{H}^{inc} = \hat{y} H^{inc} e^{-jk_0 z}$ where $\bar{E}^{inc} = 1$ [V/m].

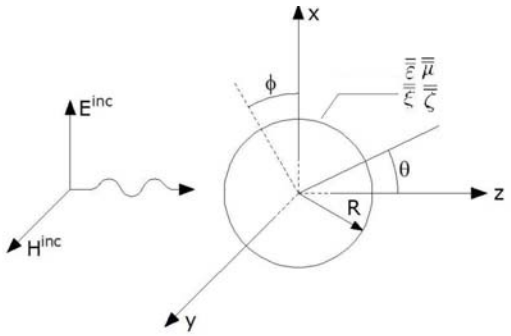

Fig. 2. A homogenized chiroferrite sphere illuminated by an EM plane wave.

A sphere of radius R is constructed and meshed by 520 tetrahedra and 1184 faces. As the first step of developing this mesh, the entire outer surface of sphere has been approximated by a grid of 72 triangles. Then a tetrahedral mesh has been grown from the outer triangulated surface into the sphere, producing a total of 256 tetrahedra and 548 faces. In order to achieve better accuracy of numerical results, refinement of the mesh in the close proximity of the outer surface has been undertaken, increasing the total number of tetrahedra to 520 and faces to 1184. At last, the radius of the sphere has been adjusted so that the total volume of the tetrahedral approximation of the sphere is equal to the actual volume of the initial sphere.

The numerical results are obtained at the frequencies of 0.4 GHz, 0.6 GHz, 1 GHz, and 1.2 GHz. The corresponding values of k_0R are 0.6032, 0.9048, 1.508, and 1.809, respectively. Figures 3 and 4 show the co-polarized and cross-polarized bistatic radar cross sections $\sigma_{\theta\theta}$ of $\phi = 0^o$ and $\sigma_{\phi\theta}$ of $\phi = 0^o$. It is noticed that the RCS of such a homogenized chiroferrite scatterer is similar to that of the two-layered chiroferrite sphere presented in [1] because they are composed of the same basic materials and dimensions.

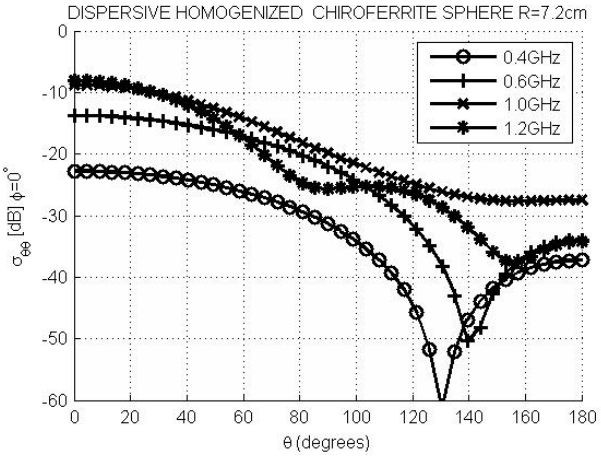

Fig. 3. Bistatic radar cross section $\sigma_{\theta\theta}$ of a homogenized chiroferrite sphere of radius R = 7.2 *cm* illuminated by an EM plane wave at frequencies of 0.4 GHz, 0.6 GHz, 1 GHz, and 1.2 GHz.

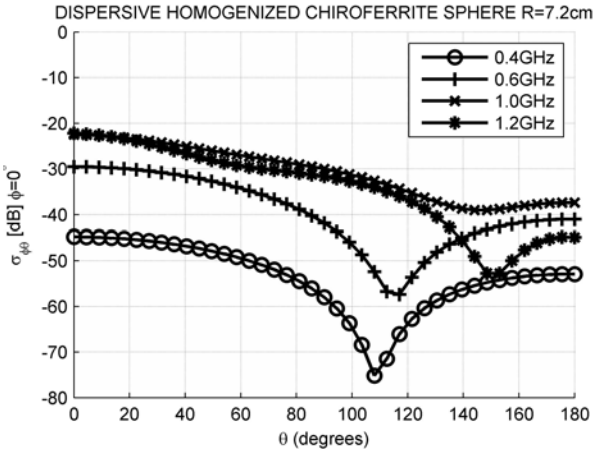

Fig. 4. Bistatic radar cross section $\sigma_{\phi\theta}$ of a homogenized chiroferrite sphere of radius R = 7.2 *cm* illuminated by an EM plane wave at frequencies of 0.4 GHz, 0.6 GHz, 1 GHz, and 1.2 GHz.

IV. DISPERSIVE HOMOGENIZED CHIROFERITE CUBE

In this section we present results for electromagnetic scattering from a dispersive homogenized chiroferrite cube illuminated by a plane electromagnetic wave. The macroscopic constitutive parameters of the chiroferrite material are obtained in section III. The length of a side of the cube is d = 14 *cm*. The dimension for the cube makes its size similar to that of the sphere investigated in section III. The incident plane electromagnetic wave propagates in the z direction, and it has the electric field component in the x direction, i.e., $\overline{E}^{inc} = \hat{x}E^{inc}e^{-jk_0z}$ and $\overline{H}^{inc} = \hat{y}H^{inc}e^{-jk_0z}$ where $\overline{E}^{inc} = 1$ [V/m], as shown in Fig. 5.

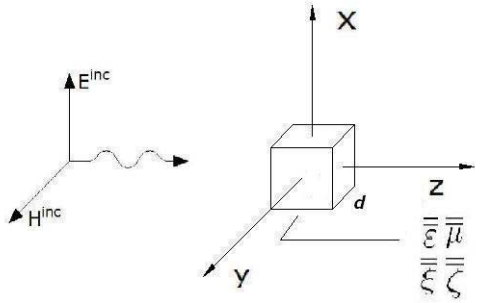

Fig. 5. A homogenized chiroferrite cube illuminated by an EM plane wave.

A meshing process similar to that in section III is realized, resulting in a total of 768 tetrahedra and 1632 faces. The numerical results are obtained at the frequencies of 0.4 GHz, 0.6 GHz, 1 GHz, and 1.2 GHz. The corresponding values of k_0d are 1.1729, 1.7593, 2.9322, and 3.5186, respectively. Figures 6 and 7 show the co- and cross-polarized bistatic radar cross sections $\sigma_{\theta\theta}$ of $\phi = 0^o$ and $\sigma_{\phi\theta}$ of $\phi = 0^o$. It is noticed that the RCS of such a cubic scatterer is at similar level of the ones of the homogenized chiroferrite sphere in section III because both cases are made of same materials and in have similar dimensions. We also note that the angular responses (dependence on θ) are different between the spherical and cubic scatterers. In particular, at f = 1.2 GHz, the difference is more pronounced.

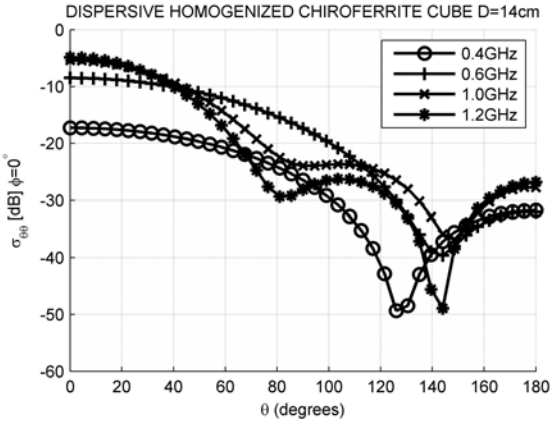

Fig. 6. Bistatic radar cross section $\sigma_{\theta\theta}$ of a homogenized chiroferrite cube of d = 14 *cm* illuminated by an EM plane wave at frequencies of 0.4 GHz, 0.6 GHz, 1 GHz, and 1.2 GHz.

V. DISPERSIVE HOMOGENIZED CHIROFERITE CYLINDER

In this section we present results for electromagnetic scattering from a finite circular cylinder of dispersive homogenized chiroferrite illuminated by an EM plane wave. The macroscopic constitutive parameters of the chiroferrite material are obtained in section III. The radius of the cylinder is R = 7 *cm* and the height of the cylinder is h = 14 *cm*. These dimensions for the cylinder make its size similar to that of the sphere investigated in section III. The incident plane wave propagates in the z direction, and it has the electric field component in the x direction, i.e., $\overline{E}^{inc} = \hat{x}E^{inc}e^{-jk_0z}$ and

$\overline{H}^{inc} = \hat{y} H^{inc} e^{-jk_0 z}$ where $\overline{E}^{inc} = 1$ [V/m], as shown in Fig. 8.

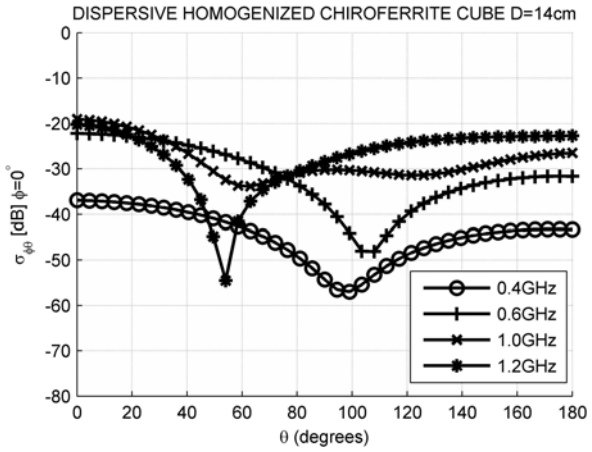

Fig. 7. Bistatic radar cross section $\sigma_{\phi\theta}$ of a homogenized chiroferrite cube of d = 14 *cm* illuminated by an EM plane wave at frequencies of 0.4 GHz, 0.6 GHz, 1 GHz, and 1.2 GHz.

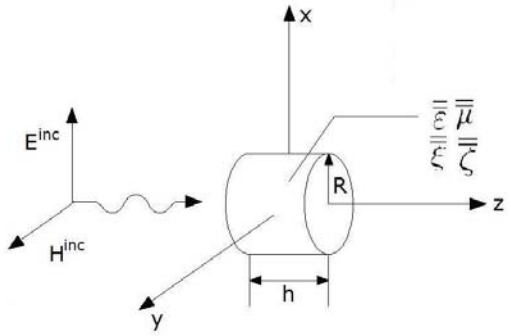

Fig. 8. A homogenized chiroferrite cylinder illuminated by an EM plane wave.

A meshing process similar to that in section III is realized, resulting in a total of 864 tetrahedra and 1920 faces. The numerical results are obtained at the frequencies of 0.4 GHz, 0.6 GHz, 1 GHz, and 1.2 GHz. The corresponding values of $k_0 h$ are 1.1729, 1.7593, 2.9322, and 3.5186, respectively. Figures 9 and 10 show the co- and cross-polarized bistatic radar cross sections $\sigma_{\theta\theta}$ of $\phi = 0^o$ and $\sigma_{\phi\theta}$ of $\phi = 0^o$. It is noticed that the RCS of such a scatterer is at similar level of the RCS of the homogenized chiroferrite sphere or cube in sections III and IV because they are made of the same materials and in have similar dimensions.

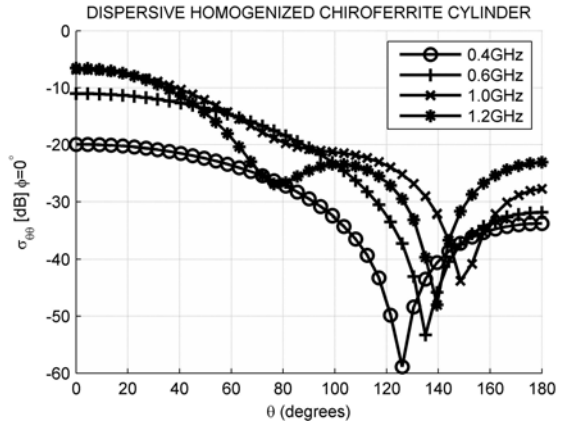

Fig. 9. Bistatic radar cross section $\sigma_{\theta\theta}$ of a homogenized chiroferrite cylinder of radius R = 7*cm* and height h = 14 *cm* illuminated by an EM plane wave at frequencies of 0.4 GHz, 0.6 GHz, 1 GHz, and 1.2 GHz.

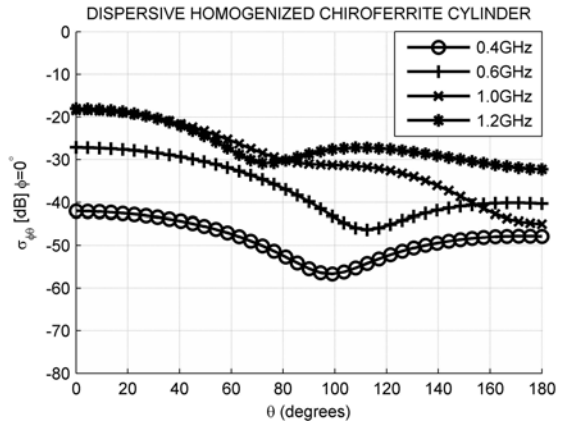

Fig. 10. Bistatic radar cross section $\sigma_{\phi\theta}$ of a homogenized chiroferrite cylinder of radius R = 7 *cm* and height h = 14 *cm* illuminated by an EM plane wave at frequencies of 0.4 GHz, 0.6 GHz, 1 GHz, and 1.2 GHz.

VI. CONCLUSION

Taking advantage of the flexibility of the method presented in [1], scattering problems that involve dispersive bianisotropic materials are solved and presented in this paper. As an example, the method is applied to investigate the scattering fields from a dispersive chiroferrite material in which chiral materials and ferrite materials are mixed. Currently, these problems are difficult to solve by conventional methods. The solutions to a few of these problems are presented in [7]. This paper represents a more comprehensive report on

the same work. The combination of chirality and anisotropic property makes these problems difficult to solve by other current frequency domain methods that may handle either chirality or the anisotropic property one at a time but not both at the same time. The ferrite material and chiral material are assumed dispersive, i.e., the constitutive relations have frequency dependency.

As discussed earlier, this method has the advantage over the time domain methods. The time domain methods rely on the Z-transform of the analytical expressions that describe the dispersion properties of the material. And these analytical expressions are in many cases very difficult to obtain. When there is more than one kind of dispersive material involved, the situation becomes even more complicated for these methods. If the material is of a periodic nature, homogenization techniques may be used to simplify the problem [8]. Corresponding computer programs need to be adapted for the different dispersion properties of the materials. The solution algorithm used in this paper is based on the method of moments. In the method of moments, problems are solved in the frequency domain, and as long as the numerical values of the material properties at the operating frequency are provided, there is no need to obtain the analytic expressions of the material dispersion over a frequency band.

The main goal of this article is not to provide a comprehensive analytical solution to the problems of interest as the analytical algorithm is described and derived in detail by the same authors in [1]. Scattering by dispersive media with mixed chiral and anisotropic properties has not been extensively studied in the past. To our best knowledge, there was no research reported that would provide solution to this type of scattering problems and that can be used as a reference to check validity of proposed algorithms. This article intends to fill that gap. With this article, the authors offered a solution to a few scenarios of scattering by mixed chiral and anisotropic media that can be used by other researchers as a baseline to confirm validity of their solutions to the problems of similar nature.

REFERENCES

[1] C. Mei, M. Hasanovic, J. K. Lee, and E. Arvas, "Comprehensive solution to electromagnetic scattering by anisotropic objects of arbitrary shape," *Progress in Electromagnetic Research (PIER) B*, vol. 42, pp. 335-362, 2012.

[2] D. H. Schaubert, D. R. Wilton, and A. W. Glisson, "A tetrahedral modeling method for electromagnetic scattering by arbitrarily shaped inhomogeneous dielectric bodies," *IEEE Trans. Antennas Propagat.*, vol. 32, pp. 77-85, Jan. 1984.

[3] D. R. Wilton, S. M. Rao, A. W. Glisson, D. H. Schaubert, O. M. Al-Bundak, and C. M. Butler, "Potential integrals for uniform and linear source distributions on polygonal and olyhedral domains," *IEEE Trans. Antennas Propagat.*, vol. 32, pp. 276-281, Mar. 1984.

[4] M. Belyamoun and S. Zouhdi, "Effective parameters of bianisotropic dispersive media in time-domain," *26th Annual Review of Progress in Applied Computational Electromagnetics (ACES)*, pp. 479-483, Tampere, Finland, April 2010.

[5] A. F. Yagli, J. K. Lee, and E. Arvas, "Scattering from three-dimensional dispersive gyrotropic bodies using the transmission line modeling (TLM) methos," *Progress in Electromagnetic Research (PIER) B*, vol. 18, pp. 225-241, 2009.

[6] V. Demir, A. Z. Elsherbeni, and E. Arvas, "FDTD formulation for dispersive chiral media using the Z transform method," *IEEE Trans. Antennas Propagat.*, vol. 53, pp. 3374-3384, Oct. 2005.

[7] C. Mei, M. Hasanovic, J. Mautz, E. Arvas, and J. Lee, "Scattering from an inhomogeneous dispersive chiroferrite body of arbitrary shape," *24th Annual Review of Progress in Applied Computational Electromagnetics (ACES)*, pp. 844-848, Niagara Falls, Canada, March 2008.

[8] M. Silveirinha, "New homogenization approach for the numerical characterization of periodic microstructured materials," *23rd Annual Review of Progress in Applied Computational Electromagnetics (ACES)*, pp. 215-220, Verona, Italy, March 2007.

Moamer Hasanovic received the B.Sc. degree from the University of Sarajevo in 1997 and the M.Sc. and Ph.D. degrees in Electrical Engineering from Syracuse University, New York (USA) in 2002 and 2006, respectively. He was an Electrical Engineer with BH Telecom Engineering Sarajevo for two years and RF Design Engineer with Anaren Microwave, Syracuse, NY. He is currently working as a Senior RF Design Engineer with EMC Technology/Florida RF Labs in Stuart, FL. He is also an Adjunct Professor at the L.C. Smith College of Engineering and Computer Science at

Syracuse University as well as an Assistant Professor at University of Sarajevo, Bosnia-Herzegovina. His research interests are in the area of computational electromagnetics, and RF/microwave devices on conventional and metamaterial platforms. Dr. Hasanovic is a member of the Applied Computational Electromagnetics Society and IEEE Antennas and Propagation Society.

Chong Mei received B.Sc. and M.Sc. degrees from Huazhong University of Science and Technology, Wuhan, China, in 1997 and 2000, respectively, and Ph.D. degree from Syracuse University, Syracuse, NY, in 2007, all in Electrical Engineering. He has been with Anaren Microwave, Inc. in East Syracuse, NY since 2002, as a Leading Engineer designing various RF/Microwave devices for the wireless infrastructure market. His research interests are in RF/microwave devices and computational electromagnetics.

Jay K. Lee received the B.Sc. degree from Seoul National University, Seoul, Korea in 1976 and the S.M. and Ph.D. degrees in Electrical Engineering from Massachusetts Institute of Technology, Cambridge, MA in 1981 and 1985, respectively. He is a Professor of Electrical Engineering and Computer Science at Syracuse University, where he served as Program Director of Electrical Engineering (2004-09). His current research interests are electromagnetic theory, waves in anisotropic media, microwave remote sensing, and antennas and propagation. He was a Research Fellow at Naval Air Development Center, Rome Air Development Center and Naval Research Laboratory and was an Invited Visiting Professor at Seoul National University in Seoul, Korea. He is a Senior Member of the IEEE. He served as Chair of IEEE Syracuse Section and as Faculty Advisor of IEEE Student Branch at Syracuse University. He has received the Eta Kappa Nu Outstanding Undergraduate Teacher Award (1999), the IEEE Third Millennium Medal (2000), and the College Educator of the Year Award from the Technology Alliance of Central New York (2002). He is the co-author of the book, {\it Electromagnetics} (by Adams and Lee, University Readers, 2012).

Ercument Arvas received the B.Sc. and M.Sc. degrees from the Middle East Technical University, Ankara, Turkey, in 1976 and 1979, respectively, and the Ph.D. degree from Syracuse University, Syracuse, NY, in 1983, all in Electrical Engineering. From 1984 to 1987, he was with the Electrical Engineering Department, Rochester Institute of Technology, Rochester, NY. In 1987, he joined the Electrical Engineering and Computer Science Department, Syracuse University, where he is currently a Professor. His research and teaching interests are in computational electromagnetic radiation and scattering, and microwave devices. He is a Member of the Applied Computational Electromagnetics Society (ACES) and a Fellow of IEEE.

Dissipative Scheme for Discontinuous Galerkin Time-Domain Method Based on a Leap-Frog Time-Stepping

Da Peng, Xingji Tang, Hu Yang, and Jianguo He

College of Electronic Science and Engineering
National University of Defense Technology, Changsha, 410073, China
da.peng.uestc@gmail.com, amani.11@163.com

Abstract ─ A dissipative scheme is proposed to improve numerical dispersion and eliminate spurious modes in the unstructured grid-based discontinuous Galerkin time-domain (DGTD) method. We introduce the dissipative terms into the centered fluxes, and a backward discretization in time is applied to the dissipative part to yield a fully explicit time-stepping scheme. In order to analyze the dispersion and dissipation properties of this scheme, we perform a numerical Fourier analysis to the normalized one-dimensional Maxwell's equations with periodic boundary conditions. In this process, the mechanism of suppression of the spurious modes is revealed for the dissipative scheme. Numerical results show that more accurate solutions can be obtained by using dissipative scheme in the DG method.

Index Terms – Backward discretization, centered fluxes, dissipative scheme, discontinuous Galerkin, fully explicit time-stepping, Fourier analysis, and periodic boundary conditions.

I. INTRODUCTION

Discontinuous Galerkin time-domain (DGTD) method is a novel numerical technique to solve time-dependent electromagnetic problems with complex geometries in which high accuracy and efficiency are required [1-4]. It employs discontinuous piecewise polynomials as basis and test functions, and then applies a Galerkin test procedure for each element to obtain the spatial discretization. The solutions are not enforced continuous across interface of any two adjacent elements. Instead, the unique fluxes are constructed to provide the coupling mechanism between elements, which gives rise to a highly parallel computation [5].

The centered fluxes coupled with a leap-frog time-stepping lead to a convergent, stable, and energy-conserving scheme [6, 12]. However, this scheme suffers from two problems: poor numerical dispersion properties and the existence of spurious modes. To improve numerical dispersion and eliminate spurious modes, a penalization of centered fluxes by dissipative terms is introduced to the DG method based on hexahedral elements [7]. With a mathematical analysis, it is shown in [7] that the dissipative scheme is less dispersive and has a better convergence than the non-dissipative one.

In practical DGTD models, the automatic mesh generation is often not feasible for building many 3D hexahedral meshes. The method of constructing an initial tetrahedral mesh and then splitting each cell into four hexahedral cells will generate a low-quality mesh [7, 8], and as a result a small time step is required due to the stability reasons. In this sense, an efficient algorithm based on tetrahedral elements may be more attractive for most problems of interest.

In this work, in order to decrease numerical dispersion error and eliminate spurious modes, the dissipative terms are introduced into the tetrahedron-based DG method as the penalization of centered fluxes. The construction of dissipative scheme is straightforward, and when employing the leap-frog algorithm, a backward discretization in time is applied to the dissipative terms to yield a fully explicit time-stepping scheme. This is distinguished from the way of directly using the upwind fluxes and employing a Runge-Kutta time-stepping method [1, 2, 10]. Numerical Fourier

Submitted On: Nov. 20, 2012
Accepted On: May 16, 2013

analysis of the fully discrete scheme is performed to investigate dispersion and dissipation relations with the mesh size per wave length. The related diagrams illustrate that the dissipative scheme is less dispersive and has the capability of suppressing spurious modes. Finally, the given examples, including metallic cavity and scattering problems, show that more accurate solutions can be obtained by using dissipative scheme in tetrahedron-based DGTD.

II. THEORY

A. Discontinuous Galerkin method

The time-domain Maxwell's curl equations for non-conducting dielectrics can be written in conservation form,

$$Q\frac{\partial \boldsymbol{q}}{\partial t}+\nabla\cdot\boldsymbol{F}=0, \tag{1}$$

where

$$Q=\begin{bmatrix}\mu & 0\\ 0 & \varepsilon\end{bmatrix},\quad \boldsymbol{q}=\begin{bmatrix}\boldsymbol{H}\\ \boldsymbol{E}\end{bmatrix},\quad \boldsymbol{F}=\begin{bmatrix}\boldsymbol{F}_H\\ \boldsymbol{F}_E\end{bmatrix}$$

and

$$\begin{bmatrix}\boldsymbol{F}_H^{\alpha}\\ \boldsymbol{F}_E^{\alpha}\end{bmatrix}=\left.\begin{bmatrix}\hat{\boldsymbol{n}}_{\alpha}\times\boldsymbol{E}\\ -\hat{\boldsymbol{n}}_{\alpha}\times\boldsymbol{H}\end{bmatrix}\right|_{\alpha=x,y,z}.$$

Here, ε and μ are respectively, the electric permittivity and magnetic permeability in materials, $\boldsymbol{E}$ and $\boldsymbol{H}$ are respectively, the electric and magnetic vector fields, $\hat{\boldsymbol{n}}_i$ signifies three Cartesian unit vectors. To solve a system of equations defined in equation (1) and pave the way for the nodal discontinuous Galerkin (DG) formulation, we assume that the computational domain Ω can be well approximated by a set Λ of non-overlapping elements $\left(\mathrm{D}^k\right)_{k=1\ldots K}$ .Define the following approximate space,

$$\mathrm{V}_h=\left\{\boldsymbol{v}(\boldsymbol{x})\in\left(L^2(\Omega)\right)^3:\forall k\in\Lambda,\boldsymbol{v}\big|_{\mathrm{D}^k}\circ\Im_k(\boldsymbol{\xi})\in\left(\mathrm{P}_p^3(\mathrm{I})\right)^3\right\}, \tag{2}$$

where $\circ$ denotes composition of functions, $\Im_k$ denotes the conform mapping $\Im_k:\mathrm{I}\to\mathrm{D}^k$, I is a standard tetrahedron defined by

$$\mathrm{I}=\left\{\boldsymbol{\xi}=(\xi,\eta,\zeta):(\xi,\eta,\zeta)\ge -1;\xi+\eta+\zeta\le -1\right\},$$

and $\mathrm{P}_p^3(\mathrm{I})$ represents the space of three-dimensional polynomials of maximum order p on the standard element I . We assume that we can approximate the solution $\boldsymbol{q}(\boldsymbol{x},t)$ by $\boldsymbol{q}_h(\boldsymbol{x},t)\in\left(\mathrm{V}_h\right)^2$. Within each element, we express $\boldsymbol{q}_h(\boldsymbol{x},t)$ in a nodal representation

$$\boldsymbol{q}_h^k(\boldsymbol{x},t)=\sum_{j=1}^{N}\boldsymbol{q}_j^k(t)L_j^k(\boldsymbol{x})=L_N^{\mathrm{T}}\boldsymbol{q}_N, \tag{3}$$

where $\boldsymbol{q}_j^k(t)$ denotes the discrete solution at space point $\boldsymbol{x}_j=\Im_k(\boldsymbol{\xi}_j)$, and $L_j^k(\boldsymbol{x})\in\mathrm{P}_p^3(\mathrm{D}^k)$ is the three-dimensional Lagrange interpolation polynomial based on N nodal points, $\boldsymbol{x}_j$, located in the interior as well as on the boundary of D^k . Furthermore, $\boldsymbol{q}_N=[\boldsymbol{q}_1^k,\ldots,\boldsymbol{q}_N^k]^{\mathrm{T}}$ and $L_N=[L_1^k(\boldsymbol{x}),\ldots,L_N^k(\boldsymbol{x})]^{\mathrm{T}}$ are the vector of the local nodal solution and the vector of Lagrange polynomials, respectively.

With the test functions $\phi_i(\boldsymbol{x})$, chosen to be the same as the basis functions $L_i(\boldsymbol{x})$, the approximate solution $\boldsymbol{q}_h$ is obtained by requiring the strong Galerkin formulation of equation (1) be satisfied over each element D^k

$$\int_{\mathrm{D}^k}\phi_i\left(Q\frac{\partial \boldsymbol{q}_h}{\partial t}+\nabla\cdot\boldsymbol{F}_h\right)d\boldsymbol{x}=\oint_{\partial\mathrm{D}^k}\phi_i\hat{\boldsymbol{n}}\cdot\left(\boldsymbol{F}_h-\boldsymbol{F}^*\right)d\boldsymbol{x}, \tag{4}$$

where $\partial\mathrm{D}^k$ is the boundary of element D^k , $\hat{\boldsymbol{n}}$ is the outward unit normal vector, and $\boldsymbol{F}^*$ is the numerical flux depends on the values of the tangential fields at both sides of $\partial\mathrm{D}^k$. Usually, for DG methods, a common choice of $\boldsymbol{F}_h^*$ is the centered flux

$$\hat{\boldsymbol{n}}\cdot\boldsymbol{F}^*=\frac{1}{2}\hat{\boldsymbol{n}}\times\begin{bmatrix}\boldsymbol{E}_h+\boldsymbol{E}_h^+\\ -(\boldsymbol{H}_h+\boldsymbol{H}_h^+)\end{bmatrix}, \tag{5}$$

where the superscript "+" refers to field values from the neighbour element.

Assuming that the materials are element wise constant, the matrix form for the semi-discrete scheme of equation (4) is obtained,

$$\begin{cases}\dfrac{d\boldsymbol{H}_N}{dt}=-\left(\mu\mathbf{M}\right)^{-1}\left(\mathbf{S}\times\boldsymbol{E}_N+\mathbf{F}\left(\hat{\boldsymbol{n}}_N\times\left(\dfrac{\boldsymbol{E}_N^+-\boldsymbol{E}_N}{2}\right)\right)\Big|_{\partial\mathrm{D}^k}\right)\\ \dfrac{d\boldsymbol{E}_N}{dt}=\left(\varepsilon\mathbf{M}\right)^{-1}\left(\mathbf{S}\times\boldsymbol{H}_N+\mathbf{F}\left(\hat{\boldsymbol{n}}_N\times\left(\dfrac{\boldsymbol{H}_N^+-\boldsymbol{H}_N}{2}\right)\right)\Big|_{\partial\mathrm{D}^k}\right),\end{cases} \tag{6}$$

where

$$\mathbf{M}_{ij} = \int_{\mathrm{D}^k} L_i(\boldsymbol{x}) L_j(\boldsymbol{x}) d\boldsymbol{x},$$
$$\mathbf{S}_{ij} = \int_{\mathrm{D}^k} L_i(\boldsymbol{x}) \nabla L_j(\boldsymbol{x}) d\boldsymbol{x},$$
$$\mathbf{F}_{il} = \int_{\partial \mathrm{D}^k} L_i(\boldsymbol{x}) L_l(\boldsymbol{x}) d\boldsymbol{s}$$

are the local mass, stiffness, and face-based mass matrices and the vectors of the local nodal solution unknowns, respectively. Since a conform mapping $\Im_K$ existed between elements D^k and I, these matrices can be conveniently constructed using the corresponding template matrices defined on I. It saves not only preprocessing time but also reduces the required storage very substantially. Efficient and accurate implementation techniques have been discussed in [1] in detail.

B. Penalization of centered flux

It is already known for time-domain problems that the centered flux can result in a non-dissipative system when combined with a leap-frog time integration scheme, where the electric fields are evaluated at the time $n\Delta t$ and the magnetic fields at the time $(n+0.5)\Delta t$. Unfortunately, the DG method based on totally centered fluxes will generate numerical spurious modes, which degrades the accuracy of the solution.

Inspired by the work of E. Montseny et al [7], we introduce a penalization of the centered flux by some dissipative terms into the nodal DG method based on tetrahedral grids. Adding the dissipative terms in the numerical scheme, the new formulation of the problem on each element becomes

$$\begin{cases} \dfrac{d\boldsymbol{H}_N}{dt} = -(\mu\mathbf{M})^{-1}\left(\mathbf{S}\times\boldsymbol{E}_N + \mathbf{F}\left(\hat{\boldsymbol{n}}_N \times \left(\dfrac{\boldsymbol{E}_N^+ - \boldsymbol{E}_N}{2} + \hat{\boldsymbol{n}}_N \times \dfrac{\boldsymbol{H}_N^+ - \boldsymbol{H}_N}{\lambda_H} \right) \right)\Big|_{\partial \mathrm{D}^k} \right) \\ \dfrac{d\boldsymbol{E}_N}{dt} = (\varepsilon\mathbf{M})^{-1}\left(\mathbf{S}\times\boldsymbol{H}_N + \mathbf{F}\left(\hat{\boldsymbol{n}}_N \times \left(\dfrac{\boldsymbol{H}_N^+ - \boldsymbol{H}_N}{2} - \hat{\boldsymbol{n}}_N \times \dfrac{\boldsymbol{E}_N^+ - \boldsymbol{E}_N}{\lambda_E} \right) \right)\Big|_{\partial \mathrm{D}^k} \right) \end{cases} \tag{7}$$

where $\lambda_E = \sqrt{\mu/\varepsilon} + \sqrt{\mu^+/\varepsilon^+}$ and $\lambda_H = \sqrt{\varepsilon/\mu} + \sqrt{\varepsilon^+/\mu^+}$. Note that this is very similar with the upwind flux [1, 2, 10, 13]. For the time derivatives in equation (7), the classical leap-frog method will lead to a globally implicit time-scheme, which is very expensive to execute for computer. Alternatively, if the penalization terms are approximated in time by a backward discretization, a fully explicit time integration scheme can be obtained,

$$\begin{cases} \dfrac{\boldsymbol{H}_N^{n+1/2} - \boldsymbol{H}_N^{n-1/2}}{dt} = -(\mu\mathbf{M})^{-1}\left(\mathbf{S}\times\boldsymbol{E}_N^n + \mathbf{F}\left(\hat{\boldsymbol{n}}_N \times \left(\dfrac{\left(\boldsymbol{E}_N^+ - \boldsymbol{E}_N\right)^n}{2} + \hat{\boldsymbol{n}}_N \times \dfrac{\left(\boldsymbol{H}_N^+ - \boldsymbol{H}_N\right)^{n-1/2}}{\lambda_H} \right)\Big|_{\partial \mathrm{D}^k} \right) \right) \\ \dfrac{\boldsymbol{E}_N^{n+1} - \boldsymbol{E}_N^n}{dt} = (\varepsilon\mathbf{M})^{-1}\left(\mathbf{S}\times\boldsymbol{H}_N^{n+1/2} + \mathbf{F}\left(\hat{\boldsymbol{n}}_N \times \left(\dfrac{\left(\boldsymbol{H}_N^+ - \boldsymbol{H}_N\right)^{n+1/2}}{2} - \hat{\boldsymbol{n}}_N \times \dfrac{\left(\boldsymbol{E}_N^+ - \boldsymbol{E}_N\right)^n}{\lambda_E} \right)\Big|_{\partial \mathrm{D}^k} \right) \right) \end{cases}. \tag{8}$$

Reference [7] has proven that the backward discretization for the time approximation of penalization terms leads to slightly more restrictive stability condition than the one obtained with the complete centered scheme. This means that more integration steps are needed to simulate the previous time.

C. Dispersive and dissipative properties

Fourier analysis [10] is carried out to investigate the dispersion and dissipation behavior of numerical scheme defined in section B. By introducing the normalized quantities $\tilde{\boldsymbol{x}} = \boldsymbol{x}/L$ and $\tilde{t} = t/(L/c_0)$, where L is a reference length and $c_0 = 1/\sqrt{\varepsilon_0\mu_0}$ represents the dimensional speed of light in vacuum, the fields are made non-dimensional as,

$$\tilde{\boldsymbol{H}} = \frac{\boldsymbol{H}}{H_0}, \quad \tilde{\boldsymbol{E}} = \frac{\boldsymbol{E}}{Z_0 H_0}, \quad \tilde{\boldsymbol{J}} = \frac{\boldsymbol{J}}{H_0/L}.$$

Here $Z_0 = \sqrt{\mu_0/\varepsilon_0}$ is the free-space intrinsic impedance and H_0 is a reference magnetic field strength. Then, we take the normalized one-dimensional formulation

$$\begin{cases} \dfrac{d\tilde{H}_N^z}{d\tilde{t}} = \mathbf{M}^{-1}\begin{pmatrix} -\mathbf{S}\tilde{E}_N^y + \dfrac{e_N}{2}\left(\tilde{E}_N^y - \tilde{E}_N^{y^+} - (1-\alpha)(\tilde{H}_N^z - \tilde{H}_N^{z^+}) \right)_{x_r} \\ -\dfrac{e_0}{2}\left(\tilde{E}_N^y - \tilde{E}_N^{y^+} + (1-\alpha)(\tilde{H}_N^z - \tilde{H}_N^{z^+}) \right)_{x_l} \end{pmatrix} \\ \dfrac{d\tilde{E}_N^y}{d\tilde{t}} = \mathbf{M}^{-1}\begin{pmatrix} -\mathbf{S}\tilde{H}_N^z + \dfrac{e_N}{2}\left(\tilde{H}_N^z - \tilde{H}_N^{z^+} - (1-\alpha)(\tilde{E}_N^y - \tilde{E}_N^{y^+}) \right)_{x_r} \\ -\dfrac{e_0}{2}\left(\tilde{H}_N^z - \tilde{H}_N^{z^+} + (1-\alpha)(\tilde{E}_N^y - \tilde{E}_N^{y^+}) \right)_{x_l} \end{pmatrix} \end{cases} \tag{9}$$

where $x \in [x_l, x_r]$ and e_i is a N long zero vector with 1 in entry i. If $\alpha = 1$, the scheme is non-dissipative, corresponding to the semi-discrete

system in equation (6). For $\alpha = 0$, it yields a dissipative scheme corresponding to equation (7).

Consider propagation of a monochromatic plane wave $e^{j(kx-\omega t)}$. If the periodic boundary conditions (PBC)

$$(u^+)_{x_r} = e^{jkh}(u)_{x_l}, \quad (u^+)_{x_l} = e^{-jkh}(u)_{x_r} \tag{10}$$

are enforced in equation (9), where $h = x_r - x_l$ and k now is the wavenumber, then the space discretized system in equation (9) can be expressed as,

$$\frac{\partial}{\partial t}\begin{bmatrix} \tilde{H}_N^z \\ \tilde{E}_N^y \end{bmatrix} = \begin{bmatrix} A_{hh} & A_{he} \\ A_{eh} & A_{ee} \end{bmatrix}\begin{bmatrix} \tilde{H}_N^z \\ \tilde{E}_N^y \end{bmatrix}. \tag{11}$$

Here A_{ee}, A_{eh}, A_{he} and A_{hh} are $N \times N$ matrices, the expressions of which are straightforward but somewhat lengthy. For the non-dimensional form of Maxwell's equations, the analytic dispersion relation is $k^2 = \omega^2$. In order to investigate numerical dispersion relationship for this fully discrete scheme, we introduce the numerical wave frequency $\tilde{\omega}$ and expect it to satisfy,

$$\begin{bmatrix} \tilde{H}_N^{z\ n+1/2} \\ \tilde{E}_N^{y\ n+1} \end{bmatrix} = e^{-j\tilde{\omega}\Delta t}\begin{bmatrix} \tilde{H}_N^{z\ n-1/2} \\ \tilde{E}_N^{y\ n} \end{bmatrix}. \tag{12}$$

In addition, we can write equation (11) as a fully explicit scheme by a backward discretized approximation in time

$$\begin{bmatrix} \tilde{H}_N^{z\ n+1/2} \\ \tilde{E}_N^{y\ n+1} \end{bmatrix} = B\begin{bmatrix} \tilde{H}_N^{z\ n-1/2} \\ \tilde{E}_N^{y\ n} \end{bmatrix}, \tag{13}$$

and

$$B = \begin{bmatrix} I + \Delta t A_{hh} & \Delta t A_{he} \\ \Delta t A_{eh}(I + \Delta t A_{hh}) & I + \Delta t A_{ee} + \Delta t^2 A_{eh} A_{he} \end{bmatrix},$$

where I is the $N \times N$ identity matrix. Substituting equation (12) into equation (13), we obtain the eigenvalue problem,

$$e^{-j\tilde{\omega}\Delta t}\begin{bmatrix} \tilde{H}_N^{z\ n-1/2} \\ \tilde{E}_N^{y\ n} \end{bmatrix} = B\begin{bmatrix} \tilde{H}_N^{z\ n-1/2} \\ \tilde{E}_N^{y\ n} \end{bmatrix}. \tag{14}$$

Solving this eigenvalue equation will produce $2N$ different values for $\tilde{\omega}_n = \tilde{\omega}_n^r + j\tilde{\omega}_n^i$. This is because an infinite set of real wavenumbers $\pm k_n$ satisfying

$$k_n = k + 2n\pi / h, \quad n = 0, \pm 1, \pm 2, \ldots \tag{15}$$

are also supported by the periodic boundary conditions in equation (10). We will refer to $\pm k_0$ as the fundamental modes while to the others as harmonic modes.

Assume that second-order polynomials are applied for the spatial discretization ($p = 2$), and for the time discretization we use

$$\Delta t = \frac{C}{2p+1} \cdot \frac{h}{p+1}, \tag{16}$$

as the time step size, which is equivalent to the setting in the $p+1$ order SSP-RK scheme [10]. The dispersion relations for the two schemes (i.e., dissipative and non-dissipative) are shown in Figs. 1 and 2, respectively. We see that for $L \ll 1$, only the numerical phase velocity of $\pm\tilde{k}_0$ is very close to the physical wave speed, but the other modes present undesired behavior on the phase speed due to the coarse discretization. These modes, which do not properly approximate any analytical one over intervals of L are treated as spurious or non-physical modes [9]. Furthermore, we also see that for the dissipative scheme, a better approximation of fundamental modes over more bandwidth is achieved than for the non-dissipative one, which exhibits unphysical behavior for the phase speed even in the well-resolved case of $L \simeq \pi / 4$.

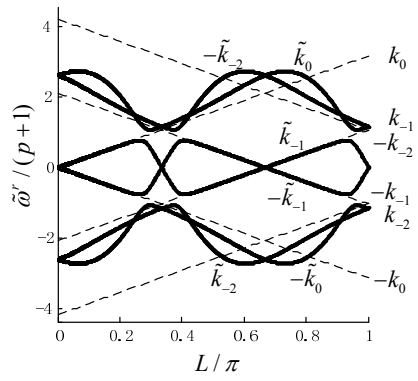

Fig. 1. Numerical dispersion relations for non-dissipative scheme of one-dimensional DGTD, $L = kh/(p+1)$, $C = h = 1$. The dashed lines represent analytical dispersion curves (equation (15)) and the solid lines reflect the dispersion characteristics for numerical modes.

For the non-dissipative scheme, the numerical modes do not attenuate in any case ($\tilde{\omega}_n^i = 0$), so the harmonics may appear together with fundamental modes in a simulation. In contrast to this, we also show in Fig. 2 the imaginary parts of all six modes for the dissipative scheme. We see

that the spurious modes are severely damped but the fundamental modes (or physical modes) are almost reserved in the interval $L<\pi/3$. This means the suppression of numerical spurious modes.

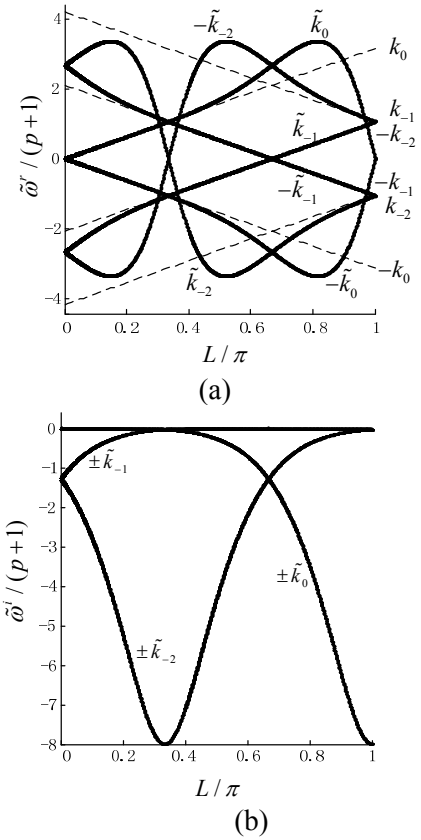

Fig. 2. Numerical dispersion (a) and dissipation (b) relations for the dissipative scheme of one-dimensional DGTD, $L=kh/(p+1)$, $C=h=1$. The solid lines reflect the dispersion or dissipation characteristics for numerical modes.

III. NUMERICAL RESULTS

To demonstrate the advantages of taking into account the dissipative terms in our scheme, we first consider the one-dimensional metallic cavity problem in the domain $x\in[-1,1]$ filled with vacuum, whose analytical solution is given by,

$$\begin{cases}\tilde{E}_y=\sin(\omega x)\sin(\omega t)\\ \tilde{H}_z=\cos(\omega x)\cos(\omega t)\end{cases} \tag{17}$$

with $\omega=n\pi$ ($n\in\mathbb{N}^+$). We choose $n=2$ and excite metallic cavity with the values at time $t=0$. There is no spurious mode arising due to this initial values setting. Figure 3 shows comparison on accuracy between the solutions obtained with the two schemes at $x=0$ in a long integration time equivalent to 40 wavelengths (only a portion of the time range is displayed in Fig. 3). Considering the backward discretization in time for the penalization terms, we restrict the time step size by $C=0.6$.

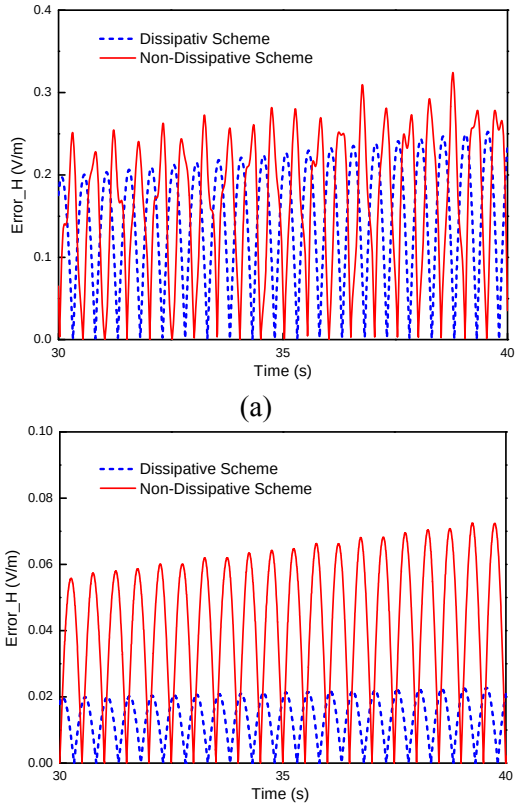

Fig. 3. Comparison on accuracy for two schemes, (a) $p=2$ with 8 equidistant elements (b) $p=4$ with 4 equidistant elements.

We note the advantage of the dissipative approach in the figure above. This benefit is mainly due to the less dispersive error than that of the non-dissipative approach. For example, in the case of $p=4$ and $K=4$, the numerical phase velocities, which can be measured by the locations of the zero crossings (in Fig. 4) are 1.0000495 and 1.0002971 for the dissipative and the non-dissipative approaches, respectively. In fact, for the dissipative scheme in Fig. 3, an important part

of the errors come from the decrease in amplitude with time ($\tilde{\omega}^i$ <0). An FDTD solution with a cell size of $\lambda/40$ is added for comparison, the numerical phase velocity of which is only 0.9989985. Furthermore, we compare results obtained with the FDTD and DG methods in Table 1. The improvement is expressed in terms of storage, CPU time and the L^2 errors, which defines the L^2 norm of the difference between the exact solution and the solutions computed for each degree of freedom (DOF) in this problem at time $t = 40$. Both DGTD approaches outperform traditional FDTD in accuracy and memory usage. It can be seen from Table 1 that the dissipative scheme is more accurate than the non-dissipative one, but more time-consuming due to the rigorous restriction on stability and the extra operations to implement the dissipative terms. How to reduce the time cost of dissipative scheme is beyond the scope of this study, and will be addressed elsewhere in the future.

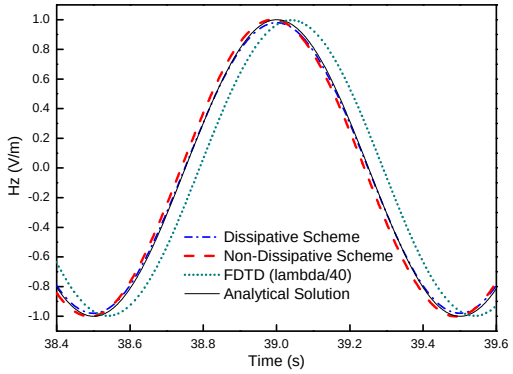

Fig. 4. Comparison of DG/FDTD results at the center of the cavity ($p = 4$ with 4 equidistant elements).

Table 1: DOF, L^2 error and CPU time costs at $t = 40$.

Method	DGTD $p = 4$, $K = 4$		FDTD $\lambda/40$
	non-dissipative	dissipative	
DOF	40	40	161
L^2 error	0.22	0.09	1.51
CPU (s)	0.88	1.16	0.455

The second example is to model the scattering of electromagnetic waves from a PEC sphere of radius $a = 10/2\pi$, whose analytical solution can be achieved with infinite series of Legendre and spherical Hankel functions [11]. The sphere is illuminated by a plane wave given by $\hat{k}_{inc} = (0,0,1)$ and $E_x(t) = \exp(-4\pi\left(\frac{t - 4.466\times10^{-9}}{2.233\times10^{-9}}\right)^2)$. The mesh size on the surface of the sphere is 0.3 m. One observation point is located outside the sphere at (0,0,-2.2) m (the origin is at the sphere center). In Fig. 5, we compare the results obtained by using or not the dissipative terms in the DG formulation. We can see the former scheme leads to a more accurate solution than the scheme without dissipative terms at the same spatial order ($p = 2$). Little oscillation appears in the solution of the latter scheme, which certainly due to the propagation of spurious modes [7]. The use of higher order ($p = 3$) in the non-dissipative scheme improves the solution but executes approximately 4.7 times slower with a 100 % increase in the required memory. The E-plane bistatic cross sections obtained from the same calculation for $ka = 10$ ($f = 300$ MHz) are also shown in Fig. 6. It is in good agreement with the exact solution.

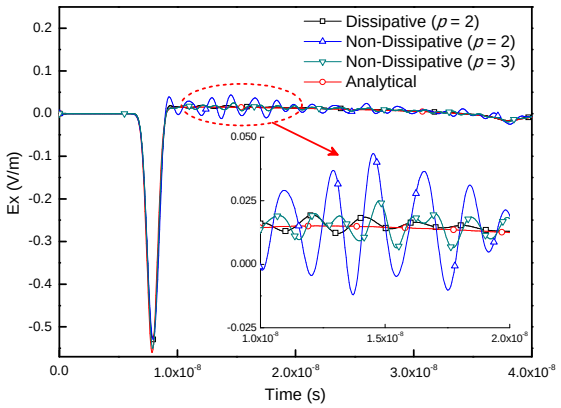

Fig. 5. Electric fields located at (0,0,-2.2) m.

The above example is not a difficult test case since the geometry of the sphere is simple and the unstructured high-quality meshes can be built with little difficulties. For complex problems, strong size-disparities and cell-distortions are usually observed in the meshes, based on which it is easier to generate numerical spurious modes for the non-dissipative scheme. The following example shows it is necessary to import the dissipative terms in

our DG scheme to obtain more accurate solutions with low spatial order approximation.

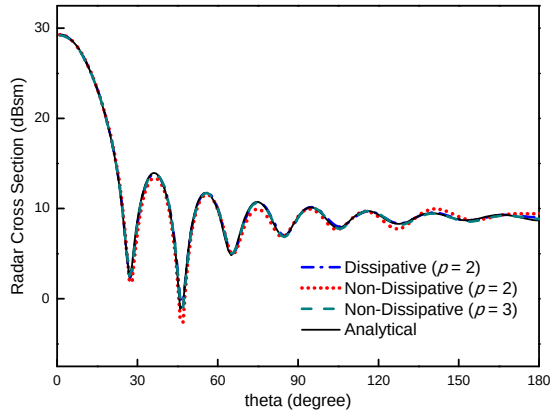

Fig. 6. Bistatic RCS for metallic sphere of $ka = 10$.

We consider plane wave scattering by a generic missile. As illustrated in Fig. 7, the thin wings of thickness 0.005 m have to be approximated by a small part of tetrahedrons with a large aspect ratio. The plane wave is given by $\hat{k}_{inc} = (0,0,-1)$ and $E_x(t) = \exp(-4\pi\left(\frac{t - 4.466\times10^{-10}}{2.233\times10^{-10}}\right)^2)$. The average mesh size on the surface of the missile is 0.02 m (1/5 wavelength at frequency 3 GHz). One observation point is located at a distance of 0.01 m from the top of the missile. Different solutions are obtained with the dissipative and non-dissipative DG methods, respectively. An FDTD solution with a cell size of 0.0025 m has been obtained as the reference solution. We can see the similar oscillation appears in the non-dissipative scheme while a convergent solution is achieved in the dissipative one. The *E*-plane bistatic cross sections obtained from the same calculation are shown in Fig. 9. It is in good agreement with the refined FDTD solution.

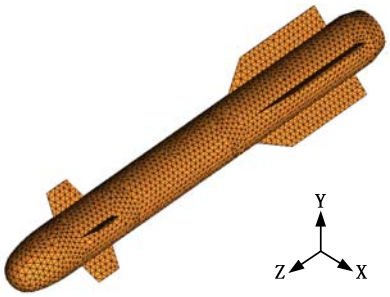

Fig. 7. Surface mesh for a generic missile.

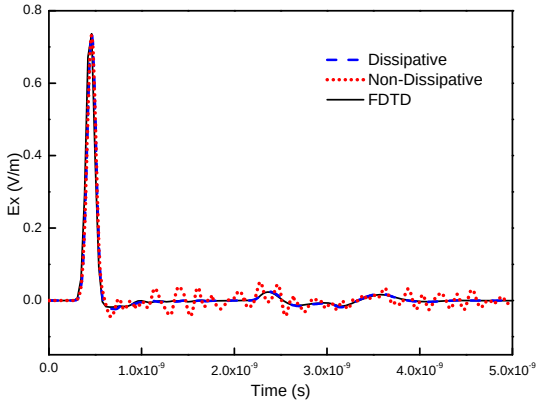

Fig. 8. Electric fields located at a distance of 0.01 m from the top of the missile ($p = 2$).

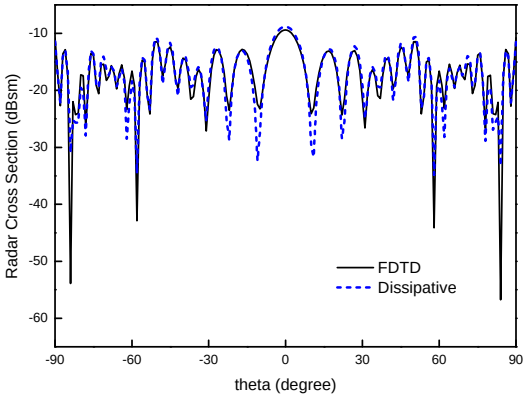

Fig. 9. Bistatic RCS of metallic missile ($p = 2$).

IV. CONCLUSION

Compared with the method proposed in [7], it is often more convenient to capture fine geometrical details of objects for the tetrahedron-based DG algorithm. In this paper, a dissipative scheme has been introduced to improve numerical dispersion and eliminate spurious modes in the tetrahedron-based DG method. We introduce the dissipative terms into the centered fluxes, and a backward discretization in time is applied to the dissipative part to yield a fully explicit time-stepping scheme. In order to analyze the dispersion and dissipation properties of this scheme, a numerical Fourier analysis is performed to the normalized 1-D Maxwell's equations with periodic boundary conditions. In this process, the mechanism of suppression of the spurious modes is revealed for the dissipative scheme. Some examples are given in the end. It shows that more accurate solutions can be obtained by using dissipative scheme in tetrahedron-based DGTD.

ACKNOWLEDGMENT

This work was supported by the National Science Foundation through grant No. 61171016.

REFERENCES

[1] J. S. Hesthaven and T. Warburton, "Nodal high-order methods on unstructured grids. I. time-domain solution of Maxwell's equations," *J. Comput. Phys.*, vol. 181, no. 1, pp. 186-221, 2002.

[2] J. S. Hesthaven and T. Warburton, *Nodal Discontinuous Galerkin Methods: Algorithms, Analysis, and Applications*, Springer, New York, 2007.

[3] M. Klemm, S. Lanteri, and C. Scheid, "Development of a DGTD method for dispersive media," *28th Annual Review of Progress in Applied Computational Electromagnetics (ACES)*, pp. 1064-1069, Columbus, Ohio, April 2012.

[4] K. Sirenko, M. Liu, and H. Bagci, "Accurate solution of Maxwell equations with exact absorbing boundary conditions for 2-D waveguide problems using time-domain discontinuous Galerkin finite element method," *28th Annual Review of Progress in Applied Computational Electromagnetics (ACES)*, pp. 1014-1018, Columbus, Ohio, April 2012.

[5] S. Dosopoulos and J. Lee, "A parallel and non-conformal interior penalty discontinuous Galerkin method for the time-domain Maxwell`s equations," *28th Annual Review of Progress in Applied Computational Electromagnetics (ACES)*, pp. 1040-1045, Columbus, Ohio, April 2012.

[6] S. Piperno and L. Fezoui, "A centered discontinuous Galerkin finite volume scheme for the 3D heterogeneous Maxwell equations on unstructured meshes," *INRIA Research Report*, no. 4733, 2003.

[7] E. Montseny, S. Pernet, X. Ferriéres, and G. Cohen, "Dissipative terms and local time-stepping improvements in a spatial high order discontinuous Galerkin scheme for the time-domain Maxwell's equations," *J. Comput. Phys.*, vol. 227, pp. 6795-6820, 2008.

[8] G. Cohen, X. Ferriéres and S. Pernet, "A spatial high-order hexahedral discontinuous Galerkin method to solve Maxwell's equations in time domain," *J. Comput. Phys.*, vol. 217, pp. 340-363, 2006.

[9] J. Alvarez, L. D. Angulo, A. R. Bretones, and S. G. Garcia, "A Spurious-free discontinuous Galerkin time-domain method for the accurate modeling of microwave filters," *IEEE Trans. Microw. Theory Tech.*, vol. 60, no. 8, pp. 2359-2369, Aug. 2008.

[10] D. Sármány, M. A. Botchev, and J. J. W. van der Vegt, "Dispersion and dissipation error in high-order Runge-Kutta discontinuous Galerkin discretizations of the Maxwell equations," *J. Sci. Comput.*, vol. 33, pp. 47-74, 2007.

[11] G. T. Ruck, D. E. Barrick, W. D. Stuart, and C. K. Krichbaum, *Radar Cross Section Handbook*, Plenum Press, New York, 1970.

[12] L. Fezoui, S. Lanteri, S. Lohrengel, and S. Piperno, "Convergence and stability of a discontinuous Galerkin time-domain method for the 3D heterogeneous Maxwell equations on unstructured meshes," *ESAIM Math. Model. Numer. Anal.*, vol. 39, no. 6, pp. 1149-1176, 2005.

[13] A. H. Mohammadian, V. Shankar, and W. F. Hall, "Computation of electromagnetic scattering and radiation using a time-domain finite-volume discretization procedure," *Computer Physics Communications*, vol. 68, pp. 175-196, 1991.

Da Peng received the B.Sc. degree in Electrical Engineering from the University of Electronic Science and Technology of China, Chengdu, China, in 2006, the M.Sc. degree in Electrical Science and Technology from the National University of Defense Technology, Changsha, China, in 2008. His primary interests include computational electrodynamics in the TD, finite element methods, and method of moments in the FD, and the application of numerical techniques for antenna and scattering problems.

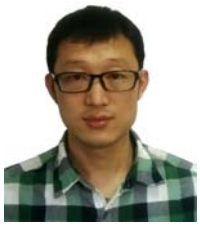

Xingji Tang received the B.Sc. and M.Sc. degrees in Electrical Science and Technology from the National University of Defense Technology, Changsha, China, in 2007 and 2009, respectively. He has been involved with shooting and bouncing ray tracing method applied to electromagnetic scattering analysis for electrically large structures.

Hu Yang received the Ph.D. degree in Electrical Science and Technology from the National University of Defense Technology, Changsha, China, in 2007. He is presently a Full Professor with National University of Defense Technology. His research interests include computational electromagnetics, microwave imaging and sensing (Synthetic Aperture Radar, SAR) and antenna design.

Simulation, Fabrication, and Performance Comparison of a GPS Antenna with Radome on the Roof of an Automobile

M. Tecpoyotl-Torres and J. G. Vera-Dimas

Centro de Investigación en Ingeniería y Ciencias Aplicadas, (CIICAp)
Universidad Autónoma del Estado de Morelos (UAEM), Cuernavaca, Mor. 62209, México
tecpoyotl@uaem.mx, gvera@uaem.mx

Abstract ─ In this work, a circularly polarized patch antenna, designed to operate at 1.57 GHz, is used for reception of GPS signals. Its analysis is carried out at first, by means of simulation, considering the following cases: antenna without radome and antenna with acrylic radome. It is shown that the radome produces a distortion of the electric field components. The antenna performance, with radome, was analyzed on several locations on the automobile, considering the effect of the complete chassis. Two cases of basic, a simplified and a more simplified advanced car models (BCM, SACM, and MSACM) were used in order to analyze the influence of chassis shape. Simulations demonstrate that the best location of the antenna is on the roof. Fabrication, experimental and practical tests are also presented. The performance analysis of the developed antenna, using it as a replacement one, is realized using a Garmin GPS and a GPS kit.

Index Terms – Axial ratio, car model, circular polarization, patch antennas, and Rogers RT/Duroid 5880.

I. INTRODUCTION

The evolution of the automobiles has answered several demands of the users. Especially in wireless communication systems, the necessity of aesthetic and efficiency has determined several proposals of antenna designed considering different types of materials and geometries. The location of the antennas constitutes also a very interesting analysis problem [1, 2].

The automotive sector has been interested in development and implementation of navigation systems [3], which are considered as one of the most important equipment of the automobile. They are formed by a global position system (GPS), with a pre-charged base of maps and highways in order to locate the vehicle. With the increase in automobile usage, accurately determining its location has become one of the growing priorities. The main advantages of the navigation systems are reduction in the time of journey, in consumption of combustible, and in the emission of contaminant gases [4]. Other application of the GPS technology is automatic location of vehicles (AVL) [5-6], as the medium to determine the geographic position of the vehicle and to transmit this information to the place where it can be used and exploited. This tool is extremely useful to the management of fleets of service vehicles, emergencies, construction, public transportation, recovery stolen vehicles, and public security [7].

The GPS satellites, often referred as SVs (for space vehicles), transmit on two frequencies in the L-band, designated as Link 1 (L1) at 1575.42 MHz, and Link 2 (L2) at 1227.60 MHz. The L1 band contains a civil signal and an encrypted military signal, and is available for commercial uses [8]; the L2 band contains another encrypted signal for military use [9, 10]. In Mexico the corresponding frequency segment is referred as 17, radio-navigation by satellite (space-earth, space-space) [11]. For the purposes of this paper, only the civil signal on L1 is of interest. Placement of a GPS antenna is critical; the roof of the automobile is considered as the most effective location to place an antenna, in terms of GPS signal reception, as it was experimentally demonstrated in [12]. The GPS antenna design has received special attention. Toyota central R&D laboratories of Japan has developed an antenna for

Submitted On: Jun. 25, 2012
Accepted On: Apr. 24, 2013

installation on the roof of an automobile [2]. They have used a dual-feed, stub loaded single patch to achieve circular polarization at the two frequencies of the satellite.

Motorola, one of the leading manufacturers of automotive GPS systems, recommends the placement of the GPS antennas at the roof, roofline or trunk [13]. On the other hand, the antenna radomes have received special attention, not only on the materials used, but also in shapes. Additionally, several companies found a niche market in the commercialization of navigation systems, because austere vehicles do not account with them [14]. The antennas contribute greatly to the total operation of the navigation systems, and they can be designed in accordance to the aesthetics and the requirements of the vehicle, to obtain totally personalized prototypes.

The satellite systems NAVSTAR-GPS [8] and Galileo [15] transmit right-hand circularly polarized signal (RHCP). Galileo provides 10 navigation signals with RHCP. Due to the antenna reciprocity, the receptor antenna must be also RCP. The main advantage of CP is that regardless of receiver orientation, it will receive a component of signal [16]. Antennas, commonly used for circular polarization, are based on corner-truncated square microstrips [17], and on square or circular patches with one or two feed points [2]. A circular polarization can, also, be obtained from a single-point square or circular patch.

In this research, the design of a circular patch antenna for GPS is realized. The interest is focused on the simulation of the antenna, due to the benefits to know the performance of the complete system. The software used for simulations is FEKO. The circular antenna is designed considering a unique feed point and a substrate of RT/Duroid 5880. Three car models, basic, simplified and more simplified advanced car models (BCM, SACM, and MSACM) were used in order to analyze also the influence of the chassis shape on simulation. In [18], two automobile similar models can be found, using monopole and multi-element antennas. The analysis of a multi-functional antenna on the automobile are carried-out in [19], using four simulation cases.

The content of this paper is organized as follows. In section II, the principles of the circular antenna design are mentioned. The simulations considering the antenna without and with acrylic radome are shown in sections III and IV. Simulations of the antenna considering three car models are presented in section V. In section VI, the fabrication process is briefly described. The simulated, experimental, and practical results are presented in section VII and discussed in section VIII. Finally, in section IX, some concluding remarks are given.

II. INDIVIDUAL PATCH ANTENNA DESIGN

A simple approximation [20] is used for the design of the circular patch antenna (CPA),

$$r = \frac{\lambda_g}{\pi}, \quad \text{with} \quad \lambda_g = \frac{c}{f_0\sqrt{\varepsilon_{reff}}}, \qquad (1)$$

where r is the patch radius, λ_g is the group wavelength, c is the speed of light in free space, ε_r is the dielectric permittivity and f_0 is the operation frequency. The length of the square ground plane side is equal to the resonator patch diameter plus $6h$, where h is the substrate thickness [21]. Equation (1) is very similar to the one used for ring resonators [22]. The calculated antenna sizes of the antenna using RT/Duroid 5880 with a thickness of 3.17 mm are: patch radio, 4.19 cm, and length of the square substrate, 10.28 cm.

Coaxial type feed is used. The location of the feed point is determined in accordance to the impedance matching. Typically the input impedance of a GPS receiver is 50 ohms [8]. The simulation of the electric far field allows us to adjust the feed point location, considering the antenna impedance as a main condition. In this case, the feed point is located near to the edge of the antenna.

III. SIMULATION OF THE INDIVIDUAL PATCH ANTENNA DESIGN

Two cases were analyzed: linear and circular polarization (Fig. 1). To observe the performance of the antenna on the circular polarization, it is not necessary to modify the established values of the antenna, it is enough to select in the main menu, the component, and the values, considering the scale that we want to observe. With the selection of circular polarization, Fig. 1 (b) was obtained. The gain values are presented in Table 1. As it can be observed, the differences between linear and circular polarization values are as expected.

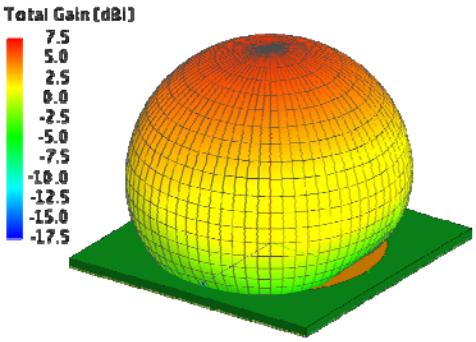

(a)

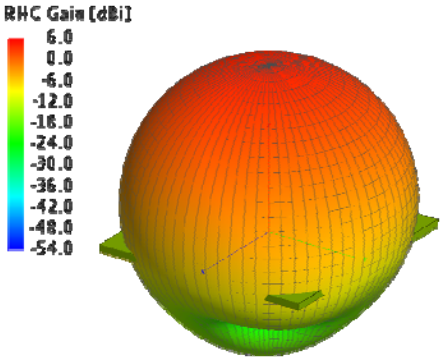

(b)

Fig. 1. Gain of the CPA considering (a) linear and (b) circular polarizations.

IV. SIMULATION OF THE ANTENNA WITH RADOME

After designing the patch antenna, it is also important to design the radome, because it prevents the early physical deterioration of the antenna and the copper oxidation, which affects lightly the performance of the antenna. It also allows easy manipulation. As a first approximation, a simple radome design of low cost, which does not affect the radiation pattern of the antenna, was chosen. Acrylic was used to implement the radome, with a thickness of 4.7 mm, due to its availability in the market. ABS (Acrylonitrile-Butadiene-Styrene) is widely used for protective housing for electronic equipment and computers, but it is more difficult to obtain and to manipulate for us. In [23], it is shown the effect of various materials on the radiation pattern of an antenna. In Fig. 2, top and cross section views of the square radome are presented. The values of the antenna gain with radome under linear and circular polarization, shown in Table 1, are slightly bigger compared to the values obtained without the radome.

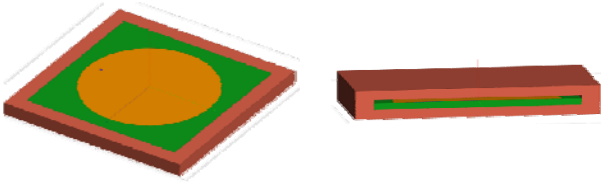

(a) (b)

Fig. 2. (a) Top and (b) cross section view of the radome containing the CPA.

Table 1: Antenna gain values.

Antenna	Gain (dB)
Without Acrylic RHC	3.957
Without Acrylic LP	6.938
With Acrylic RHC	4.198
With Acrylic LP	6.947

Simulation results of the antenna gain with acrylic radome, considering linear and circular polarization are presented in Fig. 3. The axial ratio with and without radome is shown in Fig. 4. As it can be noted, the presence of the radome produces a distortion of the electric field components.

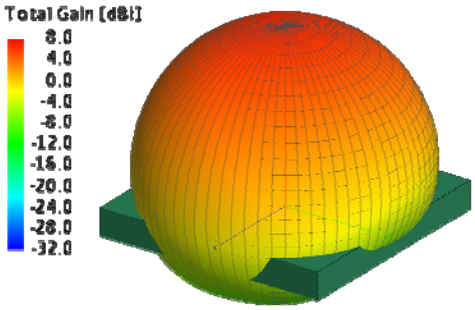

(a)

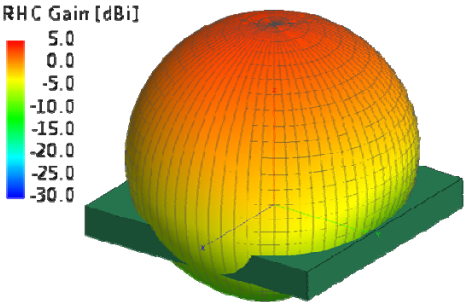

(b)

Fig. 3. 3D radiation pattern of the CPA inside the acrylic radome, with a) linear and b) circular polarizations.

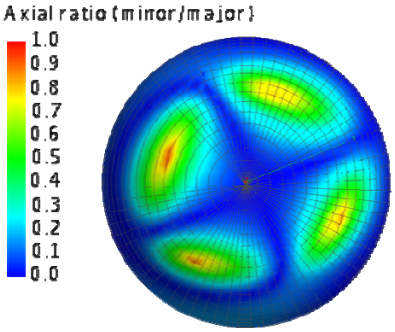

(a)

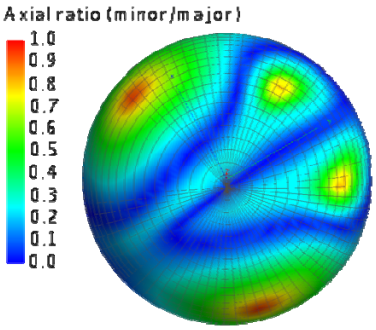

(b)

Fig. 4. Axial ratio of the antenna (a) with out and (b) with radome.

V. SIMULATION OF THE ANTENNA WITH RADOME, CONSIDERING THREE CAR MODELS

A. With a basic car model (BCM)

With the aim of observing the performance of the CPA in a more real environment, the antenna was placed on the roof of a vehicle chassis. We use a 3D drawing software that allow us to export the corresponding design in a file with extension *.x_t (parasolid files), which can be imported by CADFEKO, and after that, to realize the simulation of the complete system. The implemented car design only consists of metal layers; without doors, and other not relevant details, such as crystals, because the antenna is not closely interacting with any of them.

In order to analyze the effect of the car sizes on the antenna performance, a BCM was implemented, under two different cases (Tables 2 and 3).

Table 2: Sizes of BCMs.

BCM Features	Length (m)	Width (m)	Height (m)
Small size	4.1	1.4	1.07
Real size	4.18	1.77	1.08

Table 3: Roof sizes of BCMs.

Roof Features	Length (m)	Width (m)	Height (mm)
Small BCM	1	1.2	0.1
Real sizes BCM	1	1.6	0.1

With the vehicle design, the next step is implementing both the antenna system, and the metallic chassis in CADFEKO. In the corresponding simulations, the antenna was located on different places on the chassis (Fig. 5). The radiation patterns of the antenna gain with circular polarization considering the BCMs described in Table 2, are shown in Fig. 6. The gain values are shown in Table 4, where it can be observed that their gain values are very similar. As the gain difference between the two analyzed cases is minimal, it is possible to use any of the BCMs. We chose real size BCM in the following sections.

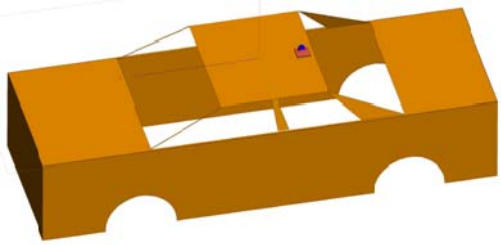

Fig. 5. View of the BCM system implemented in CADFEKO, with the patch antenna and with radome, located on the rear part of the roof.

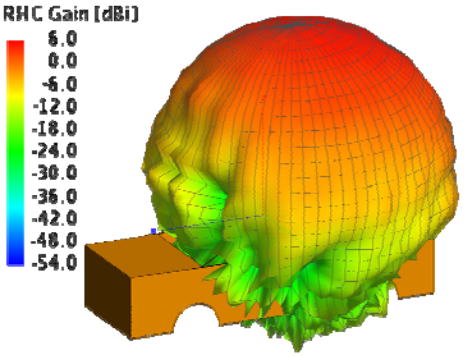

(a)

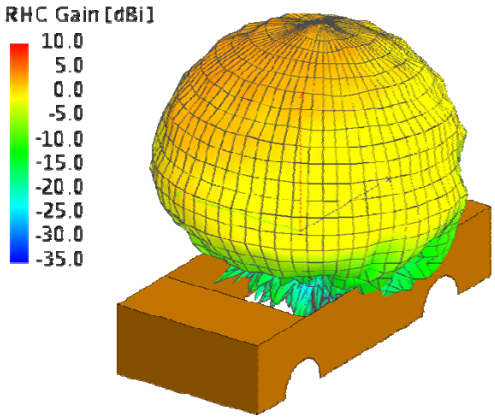

(b)

Fig. 6. Gain pattern of the CPA with acrylic radome, on the rear part of the roof of the vehicle chassis, with (a) small and (b) real size BCM.

B. With a simplified and a more simplified advanced car models (SACM and MSACM).

The model cars correspond to an AUDI R8 [24]. Due to computer limitations, we simulate a SACM (Fig. 7). The maximum width is of 1.96 m, maximum length of 4.6 m and a height of 1.09 m. The roof has a maximum and a minimum width of 1.33 m and 1.19 cm, respectively; and a maximum and a minimum length of 1.48 m and 1.28 m, respectively. The obtained gain values considering a SACM with the antenna located on several places are given in Table 5. Simulation results on the central part of the roof are shown in Fig. 8.

An MSACM was also implemented (Fig. 9). The gain when the antenna is on the central part of the roof is shown in Fig. 10, using MSACM. A summary of the gain values in other locations are also given in Table 5. In both models, the biggest gain value corresponds to the antenna located on the center of the roof.

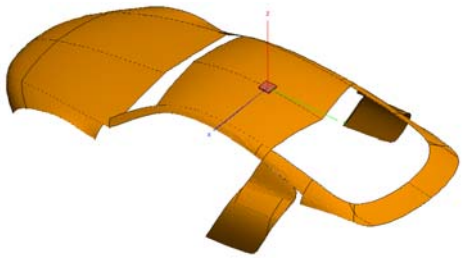

Fig. 7. SACM implemented in CADFEKO, based on an AUDI R8, with the antenna located on the central part of the roof.

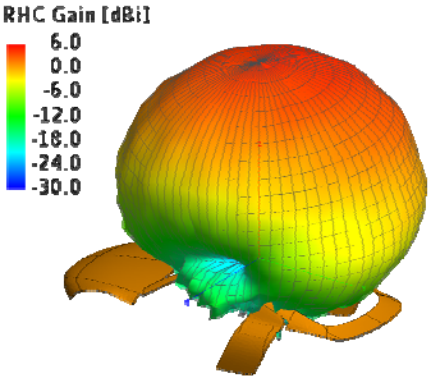

Fig. 8. Gain of the GPS antenna located on the center of the roof using SACM.

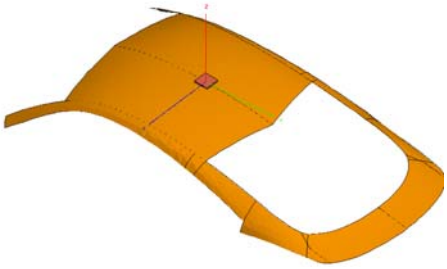

Fig. 9. View of the MSACM implemented, with the antenna located on the central part of the roof, in CADFEKO.

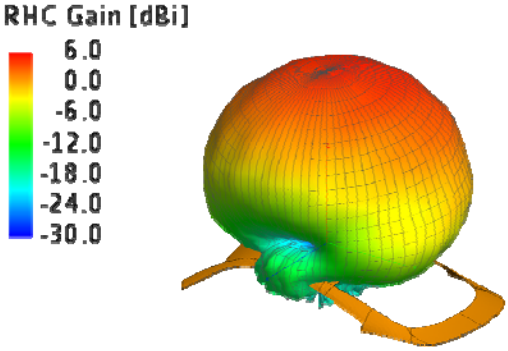

Fig. 10. Gain of the GPS antenna located on the center of the roof using MSACM.

Table 5: Gain values considering different locations of the antenna.

Position SACM	**Gain (dB)**	**Position MSACM**	**Gain (dB)**
Center	4.51	Center	4.76
Frontal	4.43	Frontal	4.7
Rear	4.4	Rear	4.44
On the trunk	4.26	On the trunk	4.34

VI. FABRICATION PROCESS

The antenna was fabricated using a PROTOMAT S-42 machine. After pattern transfer and drilling for the feeding point, the welding of the required connectors is realized (Fig. 10 (a)). For the laboratory tests, BNC female connectors of 50 Ohms to match the antenna with the experimental equipment were used. The soldering points are shown in Fig. 11. Unfortunately, the undesirable effects on the vertical profile are consequences of this feed type, which produce spurious feed radiation and poor polarization purity [2]. For experimental tests, a female MCX connector of 50 Ohms was used to couple the antenna to the GPS development kit, in order to compare its performance with the original antenna of the kit (Fig. 12) and Garmin GPS. The experimental set up is shown in Fig. 13.

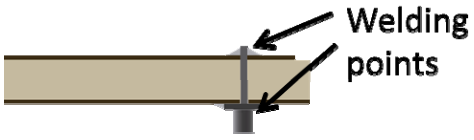

Fig. 11. Transversal section of the antenna with coaxial connector.

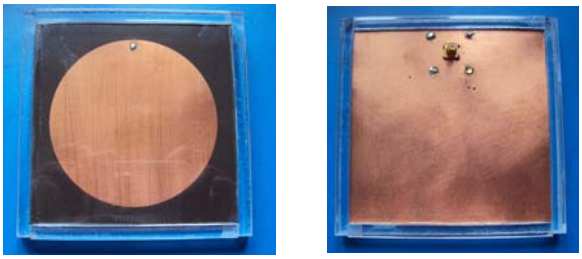

(a) (b)

Fig. 12. Front (a) and rear view (b) of the CPA with acrylic radome.

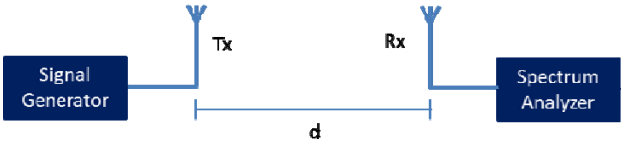

Fig. 13. Experimental set-up.

Distance d is at least of 15 cm, since the calculation of the corresponding radio of far field $\left(R > 0.62\sqrt{D^2/\lambda}\right)$, where D is the biggest size of the antenna and λ is the corresponding wavelength [25].

VII. RESULTS

A. Simulation results

In Table 6, a summary of the gain values of the antenna simulated with radome, considering the cases of sections III and IV are given.

Table 6: Gain of the circular polarization of the antenna with different car models.

Antenna location	Model	Gain (dB)
Front part, roof	BCM	5.169
Rear part, roof	BCM	5.169
Central part, roof	BCM	4.854
Central part, roof	MSACM	4.76
On trunk	MSACM	4.7
Central part, roof	SACM	4.51
On trunk	BCM	4.51
Front part, roof	MSACM	4.44
Front part, roof	SACM	4.43
Rear part, roof	SACM	4.4
Rear part, roof	MSACM	4.34
On trunk	SACM	4.26

Table 6 shows the gain values in descending order. In the BCM, the simulation results show a bigger gain values at the front and rear part of the roof. This fact can be attributed to the high symmetry in the car geometry. In the case of the antenna located at the front part of the roof in the MSACM and SACM values are very near, the same happen for the rear part. On the trunk in the MSACM, the values are almost as high as the case of the central part of the roof. The simulation of the S21 parameter of the antenna with acrylic radome is shown in Fig. 14.

B. Experimental results

The transmission-reception tests were realized using a signal synthesized generator and a spectrum analyzer (AGILENT 83732B and 8563EC, respectively). The frequency range from 1.3 GHz up to 1.8 GHz was considered to observe the antenna behavior using a constant power generated by the transmitter. The antenna separation was of 15 cm. In Fig. 14, the received power is also shown.

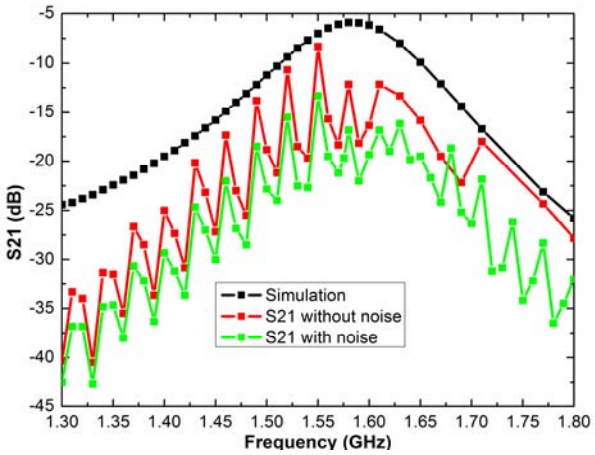

Fig. 14. Simulated and experimental S21 parameter values.

The oscillations could be attributed to the use of the connection converters to couple the laboratory equipment, and especially by the noise given by the coaxial cable.

C. Practical results

For the test of the antenna prototype as a replacement antenna, a GPS development kit was used (Fig. 15), which accounts with a GPS development card (ER-102-J, SiRF Star-II), and the NMEAgent data (this software shows the current location).

Fig. 15. GPS kit with (a) its original antenna and (b) with the replacement antenna.

The response of the antenna prototype with circular polarization can be analyzed in this case. Three measurement points were established at CIICAp parking (Fig. 16, and Table 7). Results are also compared with a Garmin GPS. Figure 17 shows the measurements trends. It can be noted, that the kit with replacement antenna provides the nearest values to the Garmin GPS measurements.

Fig. 16. Three measurement points at CIICAp parking.

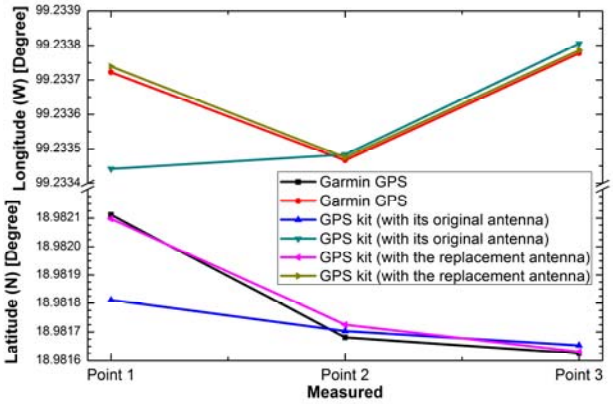

Fig. 17. Plot of points shown in Table 7.

Table 7: Measured position at 3 points in CIICAp parking.

With Garmin GPS		
Location	**Latitude (N)**	**Longitude (W)**
Point 1	18°58′5**5.6**′′	99°14′**1.4**′′
Point 2	18°58′54.**05**′′	99°14′**0.48**′′
Point 3	18°58′53.**85**′′	99°14′1.**6**′′
With GPS kit (with its original antenna)		
Point 1	18°58′5**4.52**′′	99°14′**0.39**′′
Point 2	18°58′54.**13**′′	99°14′**0.54**′′
Point 3	18°58′53.**95**′′	99°14′1.**7**′′
With GPS kit (with the replacement antenna)		
Point 1	18°58′5**5.55**′′	99°14′**1.46**′′
Point 2	18°58′54.**21**′′	99°14′**0.51**
Point 3	18°58′53.**87**′′	99°14′1.**63**′′

For the test of the antenna prototype in movement, the antenna was located on the rear roof of a Cavalier car model 95, using it as a

replacement antenna for the GPS kit (Fig. 18). The trajectory is shown in Fig. 19, and the measurement positions are points marked with arrows. The collected data are given in Table 8.

Fig. 18. Antenna location on the automobile roof.

Table 8: Measured position of several points on the university circuit.

Location	Latitude (N)	Longitude (W)
4	18°58'50.52"	99°14'2.35"
5	18°58'50.25"	99°14'5.45"
6	18°58'44.05"	99°14'9.68"
7	18°58'48.64"	99°14'14.87"
8	18°58'53.03"	99°14'21.27"
9	18°58'55.65"	99°14'25.59"
10	18°58'59.95"	99°14'19.08"
11	18°58'59.16"	99°14'12.13"
12	18°58'57.51"	99°14'5.12"

Fig. 19. Arrows indicate the place where the measurements were realized. The balloons indicate geographical locations found in Google maps.

VIII. DISCUSSION

Simulations of the antenna performance were realized considering linear and circular polarizations. For experimental tests, the available components and equipment only allow us to check the response under linear polarization. The transmission-reception test shows a peak of response in the range of GPS signals (1575.42 MHz).

It was observed in simulation of all model cases that the gain increment due to the presence of chassis is as expected without radome, with it, some variations were perceived. In the practical tests, the replacement antenna showed satisfactory results (Table 7). The measurements in fixed points, in comparison with the Garmin GPS, are nearest using the kit with the replacement antenna. In movement, as it can be observed in Fig. 19, generated using Google Maps, the measured points, except the corresponding to the CIICAp parking are located on the university circuit without invade buildings or traffic islands, which means that the measurements are useful and precise.

It is necessary to mention the following differences between the cars used in simulations and in practical tests: the model, the chassis material (in simulation, it is a perfect conductor, and in the practical tests, it was covered with black painting); and the sizes are slightly different. In experimental and practical tests, the antenna performance remains as it was expected. The symmetry influences the gain value and the pattern shape, showing in all cases a bigger gain in the central and rear part of the roof.

IX. CONCLUSIONS

Due to the presence of changes in the gain values of the antenna according to the system where it is immersed, it is desirable to perform the simulation considering the complete system elements, in order to know a more real behavior. However, it requires the combination of technological factors in order to perform these simulations and higher computer capabilities.

Surely, the antenna performance can be improved, in our BCM. This model provides a simple approximation to complex shapes. Our purpose was only to show a procedure of analysis based exclusively on the simulation results, enriching the corresponding environment, implementing a complete system.

The biggest gain values of the simulated SACM and MSACM cases generally correspond to the antenna located on the center of the roof, but

for aerodynamic behavior it is generally located on the rear part, and sometimes on the trunk. The modeling detail could be further improved, but this would increase the computer memory requirements accordingly.

The antenna performance in the reception-transmission tests shows an enough bandwidth to operate at the GPS frequency range. It was also probed that the maximum peak was very near to the designed frequency (1.57 GHz). The lightly variation can be attributed to the fabrication process. The variations in the pattern distortion of the antenna using an acrylic radome were shown. Additionally, it was possible to appreciate that the chassis contributes notably to increase the antenna gain. With the average values of the experimental tests using the GPS kit in fixed points, it can be concluded that the prototype has an adequate response as a replacement antenna, although the original antenna has a low noise amplifier.

In practical measurements on a vehicle, the result were also satisfactory, because all measured points correspond to the university circuit, as it was noted in the sampling points located using Google Maps. Some improvements could be also realized, such as: the antenna size (using alternative materials or geometries), the radome (making it with liquid acrylic or epoxy resin), and the car model (implementing additional elements or modifying shapes, but with the consequent increment of computer resources involved).

ACKNOWLEDGMENT

Authors want to thank to EM Software & Systems (USA) Inc., for FEKO license, and to Rogers Co. for the material donation for the realization of this work.

J. G. Vera-Dimas expresses his sincere thanks to CONACyT for the postgraduate scholarship under grant 270210/219230.

REFERENCES

[1] J. R. Ojha, R. Marklein, and I. Widjaja, *Technological Trends of Antennas in Cars, Advances in Vehicular Networking Technologies*, Dr. Miguel Almeida (Ed.), ISBN: 978-953-307-241-8, InTech. 2011.

[2] R. Garg, P. Bhartia, I. Bahal, and A. Ittipiboon, *Microstrip Antenna Design Handbook*, Artech House, MA, 2001.

[3] S. Nair, *A Multiple Antenna Global Positioning System Configuration for Enhanced Performance*, Thesis for the degree of Master in science, Ohio University, June 2004.

[4] http://tuning.deautomoviles.com.ar/articulos/accesorios/tecnologicos/navegadores-gps.html, Sep. 2010.

[5] http://www.aciem.org/bancoconocimiento/v/vehiculosgps/vehiculos%20gps.pdf, Sep. 2010.

[6] L. E. Frenzel, *Sistemas Electrónicos de Comunicación*, Alfaomega, México 2003.

[7] http://www.grupodeca.com.mx/productos-servicios / localizacion-automatica-vehiculos-gps/, Oct. 2010.

[8] Y. Kim, *Development of Automobile Antenna Design and Optimization for FM/GPS/SDARS Applications*, Ph.D. Dissertation, The Ohio State University, 2003.

[9] S. Alba, *Design and Performance of a Robust GPS/INS Attitude System for Automobile Applications*, Ph.D. Dissertation, Stanford University, 2004.

[10] Official U. S. Government information about the Global Positioning System (GPS) and related topics. Available at: http://www.gps.gov/systems/gps/modernization/civilsignals/, April 2013.

[11] Comisión Federal de Telecomunicaciones. *Cuadro Nacional de Frecuencias. Clasificación de Servicios* 2007.

[12] K. Yegin, "On-vehicle GPS antenna measurements," *IEEE Antennas and Wireless Propagation Letters*, vol. 6, pp. 488-491, 2007.

[13] *Engineering Notes*: OncoreTM Active Antenna, http://www. Oncore.motorola.com (April 2012).

[14] http://www.gpsenlinea.com/Vehiculos.html, Oct. 2010.

[15] J. Á. Abellán, *GNSS Array: Diseño de una Antenna con Polarización Circular*, Enginyeria de Telecomunicació. Projecte Fi de Carrera, 2009

[16] S. Murugan and V. Rajamani. "Design of wideband circularly polarized capacitive fed microstrip antenna," *International Conference on Communication Technology and System Design,* vol. 30, pp. 372-379, 2011.

[17] K. Wong, *Compact and Broadband Microstrip Antennas*, Wiley Interscience, New York, 2002.

[18] A. Rasku, *Multi-Antenna Solutions for Automotive Environment*, Master of Science Thesis, Tampere University of Technology, Nov. 2008.

[19] T. Karacolak and E. Topsakal, "Mixed order tangential vector finite elements (TVFEs) for tetrahedral and applications to multi-functional automotive antenna design," *Applied Computational Electromagnetics Society ACES Journal*, vol. 22, no. 1, pp. 117-124, 2007.

[20] M. Tecpoyotl-Torres, J. G. Vera-Dimas, R. Vargas-Bernal, M. Torres-Cisneros, A. Zamudio-

Lara, and V. Grimalsky, "Pentagonal microstrip antenna equivalent to a circular microstrip antenna for GPS operation frequency," *Memorias del 7º Congreso Internacional de Cómputo en Optimización y Software, CICOS 09*, pp. 200-208, 2009.

[21] R. H. Garg, *Microstrip Antenna Design Handbook*, Artech House, ISBN: 0-89006-513-6, 2001.

[22] J. Hong and M. J. Lancaster, *Microstrip Filters for RF/Microwave Applications*, Wiley Series in Microwave an Optical Engineering, New York, 2001.

[23] J. G. Vera-Dimas and M. Tecpoyotl-Torres, "Kit educativo para la comprensión de la propagación de ondas electromagnéticas," Memoria Técnica *ROC&C 2009. Vigésima Reunión de Otoño de Comunicaciones, Computación, Electrónica y Exposición Industrial*. Acapulco, México, 2009.

[24] http://www.audi.es/es/brand/es/Modelos/R8/r8_coupe/caracteristicas/Datos_tecnicos/Dimensiones.html, June 2012.

[25] C. A. Balanis *Antenna Theory*, 3rd edition, Wiley-Inter Science, 2005.

Margarita Tecpoyotl Torres received the Mathematician degree from the Autonomous University of Puebla (UAP), Mexico, in 1991, and the Diploma of Electronic Engineer in 1993. She received the M.Sc. and Ph.D. degrees in Electronics from INAOE, in 1997 and 1999, respectively. Dr. Tecpoyotl works, since 1999, at CIICAp of the UAEM, Mexico, where she is currently titular Professor. Her main research interest includes MEMS, antenna design, and microwave devices. She has currently two patents, conceded by Mexican Institute of Intellectual Property, IMPI, and other two under revision. She holds the status of National Researcher (SNI) level 1.

José Gerardo Vera Dimas graduated from the Technologic of Morelia as Electronic Engineer. Member IEEE since January 2005. Commit member of VII and VIII ROPEC. He received the award of "EGRETEC 2009" by the Association of Graduates from the Technological Institute of Morelia. He received the M.Sc. degree in Electronics from UAEM. Nowadays, he is a Ph. D. degree student in CIICAp at UAEM. He has currently two patents in revision.

Tunable Bandstop Filter Based on Split Ring Resonators Loaded Coplanar Waveguide

Qianyin Xiang, Quanyuan Feng, and Xiaoguo Huang

School of Information Science and Technology,
Southwest Jiaotong University, Chengdu, Sichuan, 610031, China
xiangqianyin@ieee.org, fengquanyuan@163.com, xiaoguohuang09@gmail.com

Abstract ─ In this paper, a novel electrical tunable bandstop filter based on coplanar waveguide (CPW) loaded with split ring resonators (SRRs) is proposed. The unit cell of the bandstop filter is formed by etching single SRR on the CPW back substrate side, and the SRRs can be excited by the CPW slot's magnetic field. Lumped equivalent circuit models are developed to analyze the frequency responses, and it shows that by loading the common cathode varactor diodes at the split region of the SRR outer ring, the resonant frequency of the bandstop filter can be electronically adjusted by tuning the reverse voltage of the varactor diodes. The prototype with overall size of 26.6 mm × 50 mm × 0.508 mm was designed and fabricated to validate the proposed structure. The measured tunable resonant frequency of the fabricated bandstop filter is from 2.19 GHz to 2.31 GHz while a reverse bias voltage is varying from 0 V to 30 V. It also shows that the -10 dB bandwidth is less than 45 MHz.

Index Terms ─ Coplanar waveguide, tunable bandstop filter, and varactor loaded split ring resonators.

I. INTRODUCTION

Recently, it is very popular to add tuning ability to conventional microwave components to realize electrical tunable/reconfigurable microwave components [1-9], which can well satisfy the requirements of modern multi-mode and programmable wireless systems. Bandstop filter is one of the most important microwave components to filter out the unwanted signals or nearby huge power signals, and avoid frequency aliasing in the intermediate frequency [8-11]. Therefore, tunable bandstop filters will play a key role in the future wireless systems. Split ring resonators (SRRs) are small resonant elements with a high quality factor at microwave frequency. Since SRRs can be easily implemented by planar technology, several compact microwave components using SRRs and complementary split ring resonators (CSRRs) have been proposed based on microstrip technology and coplanar waveguide (CPW) technology, i.e., lowpass and bandpass filter [12], metamateral devices [13-15], and bandstop filters [16].

In this work, a novel tunable bandstop filter based on CPW loaded with SRRs is presented. The unit cell of the bandstop filter is formed by etching a single SRR on the CPW back substrate side. By loading the common cathode varactor diodes at the split region of the resonator's outer ring, the resonant frequency of the bandstop filter can be electronically adjusted by tuning the reverse voltage of the varactor diodes.

II. FILTER DESIGN

Figure 1 shows the structure of the proposed bandstop filter with two unit cells, and a single SRR is etched in the CPW central back substrate for each unit. As a single SRR is etched in the central back substrate for each unit, it provides an opportunity for acquiring low resonant frequency by modifying the dimensions of the SRR, while the working frequency range of the conventional CPW metamaterial transmission line unit cell with a pair of SRRs is limited by the CPW strip layout [16]. To analyze the performances of this structure, Rogers 5880 substrate with a relative permittivity of 2.2, a loss tangent of 0.0009 and

Submitted On: May 27, 2012
Accepted On: May 15, 2013

thickness of 0.508 mm is chosen for our designs. Since SRR is a planar magnetic resonator, which can be excited by an axial magnetic field [17]. Therefore, the strong magnetic coupling between the CPW and the SRRs is expected in the vicinity of resonance, thereby, a stopband is generated in the frequency response. Since SRR is a sub-wavelength resonator, lumped circuit model can be used to study the characters of the filter. The proposed lumped-element equivalent circuit model for the bandstop filter is depicted in Fig. 2 (a). In this model, the SRR is modeled as the average inductance L_r, the loss resistance R_r and the average capacitance C_r. The average capacitance C_r can be approximately obtained usin equation (1); [1, 18],

$$C_r = \frac{C_g}{4} + \frac{C_o + 0.4C_i}{2\pi} \tag{1}$$

where C_g is the capacitance due to the gap of the outer and inner rings, C_o and C_i are the capacitance of the outer ring split region and the inner ring split region, respectively. The CPW is modeled as a low pass network that contains the inductance L_{sin}, L_s, and L_g, and the capacitance C_{sin} and C_s. The magnetic coupling effect is denoted by M.

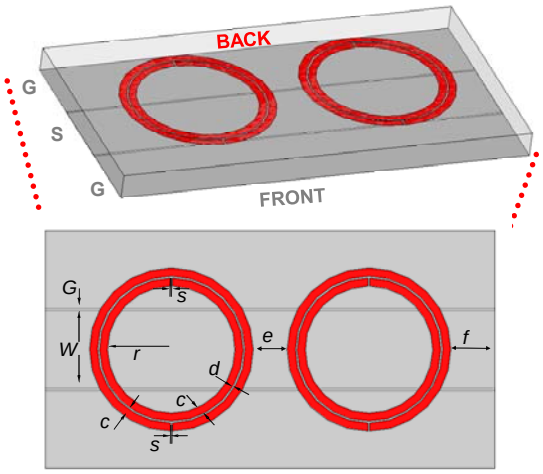

Fig. 1. Configuration of the bandstop filter. (The width of the CPW signal strip W = 8.7 mm, the gap of the CPW signal strip G = 0.2 mm, the width of the SRR strip c = 0.9 mm, the gap between the SRR inner and outer rings d = 0.2 mm, the radius of the inner ring r = 7.1 mm, the split of the SRR rings s = 0.2 mm, the distance between the SRR edge e = 3.8 mm, the distance between the SRR edge, and the CPW terminal f = 4.9 mm).

The transmission responses of the proposed bandstop filter in Fig. 1 are simulated and investigated by full-wave electromagnetics (EM) simulation software (Ansoft's HFSS10) using finite-element method and the resonant characteristics of the filter are presented in Fig. 2 (b). The simulated resonance frequency is 2.53 GHz, and a frequency bandgap is obtained profiting from the resonant of the SRRs. By using the curve-fitting technology we have extracted the parameters from the equivalent circuit model network as shown in Fig. 2 (a). The circuit model simulated results are shown as the dash curve in Fig. 2 (b), which match the EM simulated results very well. Therefore, we can conclude that the equivalent circuit model is basically correct and is fully capable of explaining the transmission characteristics of the structure. In view of this model, the lowest resonant frequency (f_r) of the bandstop filter can be written as,

$$f_r = \frac{1}{2\pi\sqrt{L_r C_r}}. \tag{2}$$

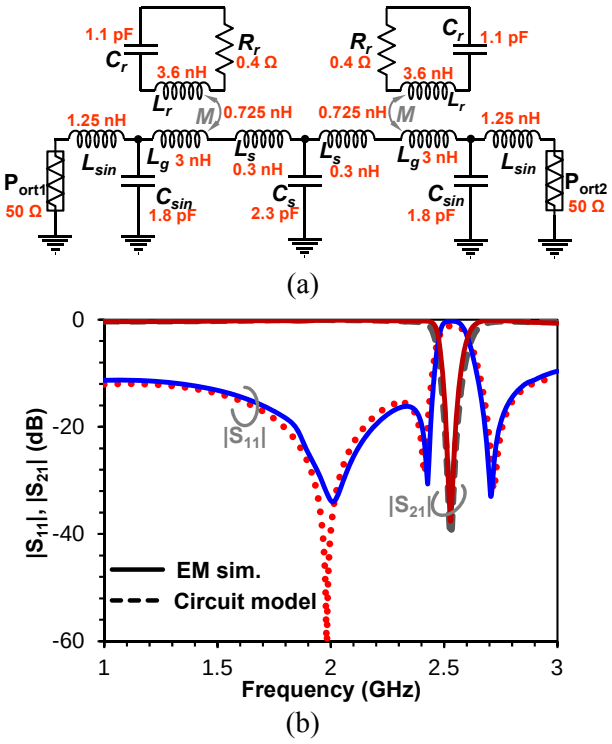

Fig. 2. EM simulated and lumped circuit model calculated results of the bandstop filter: (a) the lumped circuit model of the bandstop filter, and (b) the lumped circuit model calculated results and the EM simulated results.

Generally, the split capacitances of the SRR are ignored since they are relatively small and only the gap capacitance is taken into account when modeling the SRR. However, when a capacitor is loaded in the split region, the effect of the split capacitance gets stronger on the resonant frequency [1], and the capacitance of the SRR loaded with varactor should be written as,

$$C_{rt} = C_r + \frac{C_{\text{var}}}{2\pi} \tag{3}$$

where C_{var} is the varactor capacitance.

Figure 3 (a) shows the lumped circuit model of the tunable bandstop filter based on the SRR loaded with varactor, and the resonant frequency (f_{rt}) of the tunable bandstop filter, which can be obtained using equation (4),

$$f_{rt} = \frac{1}{2\pi\sqrt{L_r C_{rt}}} = \frac{1}{2\pi\sqrt{L_r\left(C_r + \frac{C_{\text{var}}}{2\pi}\right)}} . \tag{4}$$

Therefore, the frequency tuning radio of the circuit can be expressed as,

$$R = \frac{f_{rt(\max)}}{f_{rt(\min)}} = \sqrt{\frac{2\pi C_r + C_{\text{var}(\max)}}{2\pi C_r + C_{\text{var}(\min)}}} , \tag{5}$$

where $f_{rt(max)}$ is the maximum central frequency under the minimum varactor capacitance $C_{var(min)}$, and $f_{rt(min)}$ is the minimum central frequency under the maximum varactor capacitance $C_{var(max)}$.

It can be seen from equation (5) that the tuning ratio of the central frequency of the bandstop filter is reduced by C_r. However, for a constant central frequency, small C_r will increase the requirement of the inductance L_r, therefore leading to a large area of SRR layout. Fig. 3 (b) shows the circuit model calculated transmission characters under different value of C_{var} (0.315 pF ~ 1.335 pF), and a 158 MHz (2.316 GHz ~ 2.474 GHz) resonant frequency tunable range is obtained. It can be seen from equation (4) and Fig. 3 (b) that the frequency performance of the bandstop filter can be tuned by placing the varactor at the split region of the SRR outer ring. Figure 3 (c) shows the configuration of the proposed tunable bandstop filter loaded with semiconductor varactor diodes. Since single varactor diode can be DC shorted by the outer ring, and a DC disconnected capacitor may reduce the tune radio of the varactor. In this work, the common cathode connection of the varactor diodes is adopted to deal with this problem. A tunable reverse bias voltage source with inductor choke is connected between the cathode and anode of the varactor diodes. The resonant frequency of the proposed bandstop filter can be adjusted by tuning the reverse bias voltage.

To electronically tune the stop-band of the bandstop filter, SMV-1405 varactor diode from SKYWORKS in SC-70 package has been adopted as a tuning element, and common cathode diode connection is used to avoid DC straightforward of the circuit. The single varactor capacitance is 0.63 pF and 2.67 pF at 30 V and 0 V reverse bias voltage, respectively, and the relative capacitance change is less than 5 % while the temperature ranging from -40° C to 85° C. Figure 3 (d) shows the simulated performance of the proposed filter under different reverse bias voltages from 0 V to 30 V. The simulated tunable resonant frequency of the bandstop filter is from 2.28 GHz to 2.425 GHz.

III. MEASUREMENT

To confirm and demonstrate the tuning characteristics of the stop-band, the structure shown in Fig. 3 (c) is fabricated on a *Rogers* 5880 substrate. The photograph of the fabricated filter is proposed in Fig. 4. The overall size of the prototype is 26.6 mm × 50 mm × 0.508 mm. The measurement is accomplished with *Agilent* E5071C network analyzer and *Agilent* E3634A tunable DC power supply.

Figure 5 (a) shows the simulated and measured *S*-parameters of the bandstop filter without loading the varactors. It can be observed that the stop-band insertion loss is better than 40 dB, the central frequency is 2.458 GHz, and the retern loss of the pass-band is better than 10 dB. There is a 100 MHz frequency shift between the simulated and measured results in Fig. 5 (a) due to the inaccuracy in fabrication and implementation, and the parameters leading to skew values.

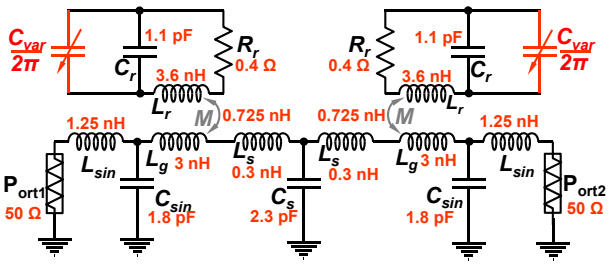

(a)

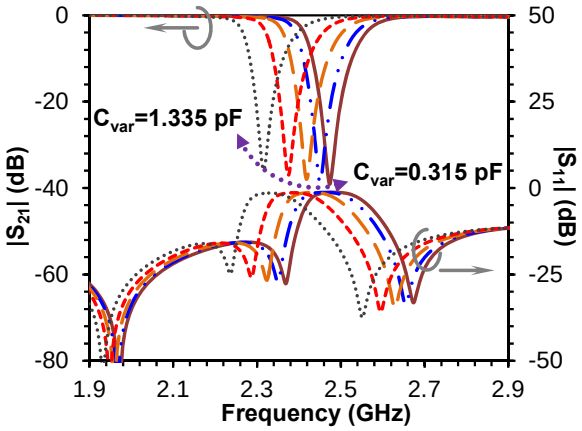

(b)

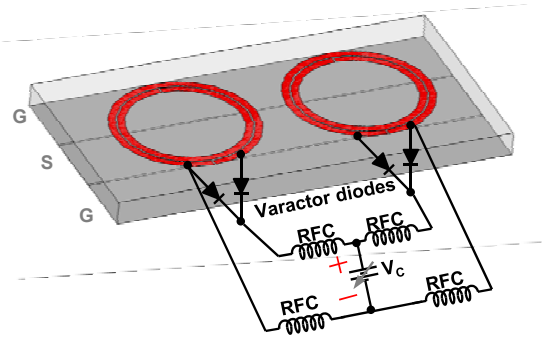

(c)

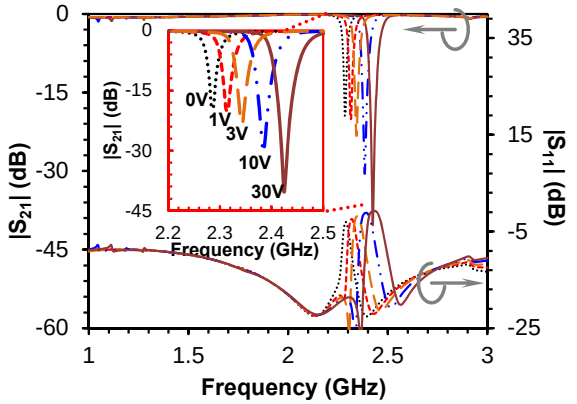

(d)

Fig. 3. Configuration and frequency responses of the tunable bandstop filter: (a) the circuit model, (b) the circuit model calculated tunable results, (c) the configuration of the tunable bandstop filter, and (d) the simulated *S*-parameters of the filter loaded with SMV1405 varactor diode under different reverse voltages.

Figure 5 (b) and (c) show the measured *S*-parameters of the fabricated tunable bandstop filter. The measured tunable resonant frequency of the bandstop filter is from 2.19 GHz to 2.31 GHz with a -10 dB bandwidth less than 45 MHz. The results show that the rejection of the stop-band is reduced when the reverse bias decreases. From equation (6), it can be seen that this is because the large capacitance or the small inductance of the SRR, which can result in a low quality value (Q) due to the parasitic resistance R_r of the SRR,

$$Q = \frac{1}{2\pi R_r}\sqrt{\frac{L_r}{C_r + C_{\text{var}}/2\pi}} \quad . \tag{6}$$

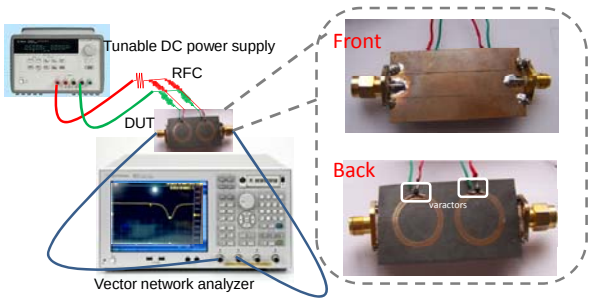

Fig. 4. The Photograph of the fabricated tunable bandstop filter.

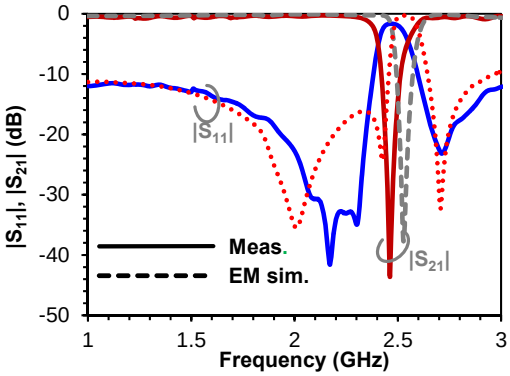

(a)

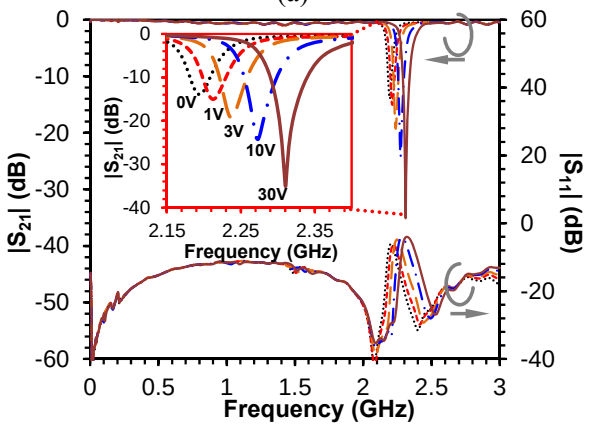

(b)

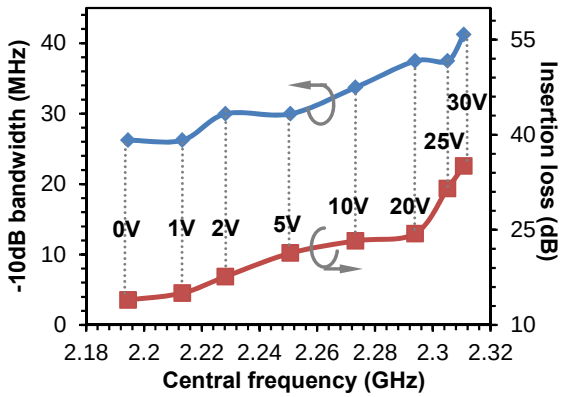

(c)

Fig. 5. The *S*-parameters of the fabricated filter: (a) the simulated and measured *S*-parameters of the bandstop filter without loading the varactors, (b) the measured *S*-parameters of the tunable bandstop filter under different reverse voltages, and (c) the -10 dB bandwidth, resonant frequency and insertion loss of the tunable stop-band under different reverse voltages.

IV. CONCLUSION

A novel tunable bandstop filter based on coplanar waveguide (CPW) loaded with split ring resonators (SRRs) is proposed, and lumped equivalent circuit analysis models are developed. The unit cell of the bandstop filter is formed by etching a single SRR on the CPW back substrate side. Comparing with the conventional CPW metamaterial transmission line unit cell with a pair of SRRs whose resonant frequency is limited by the CPW strip layout, the proposed structure provides an opportunity for acquiring low resonant frequency by modifying the dimensions. By loading common cathode varactor diodes at the split region of the SRR outer ring, the resonant frequency of the bandstop filter can be electronically tuned by adjusting the reverse voltage of the varactor diodes. The prototype with overall size of 26.6 mm × 50 mm × 0.508 mm was designed and fabricated. The tunable bandstop filter with a measured tunable resonant frequency from 2.19 GHz to 2.31 GHz under a bias voltage of 0 V to 30 V has been presented and the -10 dB bandwidth is less than 45 MHz.

ACKNOWLEDGMENT

This work was supported by the National Natural Science Foundation of China (NSFC) under Grant 60990320, 60990323, 61271090, the National 863 Project of China under Grant 2012AA012305, Sichuan Provincial Science and Technology Support Project under Grant 2012GZ0101, and Chengdu Science and Technology Support Project under Grant 12DXYB347JH-002. The authors would like to express their deep appreciations to Dr. Gaofeng Pan from Southwest University, Chongqing, China, for his valuable suggestions on this paper.

REFERENCES

[1] K. Aydin and E. Ozbay, "Capacitor-loaded split ring resonators as tunable metamaterial components," *Journal of Applied Physics*, vol. 101, no. 2, pp. 24911, Jan. 2007.

[2] B. D. Horwath and T. Al-Attar, "Simulation and design of a tunable patch antenna," *Applied Computational Electromagnetics Society (ACES) Journal*, vol. 26, no. 12, pp. 1039-1045, Dec. 2011.

[3] Q. Xiang, Q. Feng, X. Huang, and D. Jia, "Electrical tunable microstrip lc bandpass filters with constant bandwidth," *IEEE Transactions on Microwave Theory and Techniques*, vol. 61, no. 3, pp. 1124-1130, 2013.

[4] X. G. Huang, Q. Y. Feng, and Q. Y. Xiang, "Bandpass filter with tunable bandwidth using quadruple-mode stub-loaded resonator," *IEEE Microwave and Wireless Components Letters*, vol. 22, no. 4, pp. 176-178, Apr. 2012.

[5] Y. S. Li, W. X. Li, and W. H. Yu, "A switchable UWB slot antenna using SIS-HSIR and SIS-SIR for multi-mode wireless communications applications," *Applied Computational Electromagnetics Society (ACES) Journal*, vol. 27, no. 4, pp. 340-351, Apr. 2012.

[6] Q. Y. Xiang, Q. Y. Feng, and X. G. Huang, "Half-mode substrate integrated waveguide (HMSIW) filters and its application to tunable filters," *Journal of Electromagnetic Waves and Applications*, vol. 25, no. 14-15, pp. 2043-2053, 2011.

[7] Q. Y. Xiang, Q. Y. Feng, X. G. Huang, and D. H. Jia, "Substrate integrated waveguide filters and mechanical/electrical reconfigurable half-mode substrate integrated waveguide filters," *Journal of Electromagnetic Waves and Applications*. vol. 26, no. 13, pp. 1756-1766, Sep. 2012.

[8] X. Y. Zhang, C. H. Chan, Q. Xue, and B. J. Hu, "RF tunable bandstop filters with constant bandwidth based on a doublet configuration," *IEEE Transactions on Industrial Electronics*, vol. 59, no. 2, pp. 1257-1265, Feb. 2012.

[9] Q. Y. Xiang, Q. Y. Feng, and X. G. Huang, "A novel microstrip bandstop filter and its application to reconfigurable filter," *Journal of Electromagnetic Waves and Applications*, vol. 26, pp. 1039-1047, June 2012.

[10] Q. Y. Xiang, Q. Y. Feng, and X. G. Huang, "Bandstop filter based on complementary split ring resonators defected microstrip structure," *Journal of Electromagnetic Waves and Applications*, vol. 25, no. 13, pp. 1895-1908, 2011.

[11] H. Aghayari, N. Komjani, and N. M. Garmjani, "A novel integrated corrugated waveguide bandpass filter," *Applied Computational Electromagnetics Society (ACES) Journal*, vol. 27, no. 1, pp. 67-73, Jan. 2012.

[12] G. E. Al-Omair, S. F. Mahmoud, and A. S. Al-Zayed, "Lowpass and bandpass filter designs based on DGS with complementary split ring resonators," *Applied Computational Electromagnetics Society (ACES) Journal*. vol. 26, no. 11, pp. 907-914, Nov. 2011.

[13] J. C. Liu, W. Shao, and B. Z. Wang, "A dual-band metamaterial design using double SRR structures," *Applied Computational Electromagnetics Society (ACES) Journal*. vol. 26, no. 6, pp. 459-463, June 2011.

[14] M. C. Tang, S. Q. Xiao, C. J. Li, C. L. Wei, and B. Z. Wang, "Scan blindness elimination using composite defected ground structures and edge-coupled split ring resonators," *Applied Computational Electromagnetics Society (ACES) Journal*, vol. 26, no. 7, pp. 572-583, July 2011.

[15] M. C. Tang, S. Q. Xiao, D. Wang, J. Xiong, K. Chen, and B. Z. Wang, "Negative index of reflection in planar metamaterial composed of single split-ring resonators," *Applied Computational Electromagnetics Society (ACES) Journal*, vol. 26, no. 3, pp. 250-258, March 2011.

[16] F. Martin, J. Bonache, F. Falcone, M. Sorolla, and R. Marques, "Split ring resonator-based left-handed coplanar waveguide," *Applied Physics Letters*, vol. 83, no. 22, pp. 4652-4654, 2003.

[17] R. Marques, F. Mesa, J. Martel, and F. Medina, "Comparative analysis of edge- and broadside-coupled split ring resonators for metamaterial design - theory and experiments," *IEEE Transactions on Antennas and Propagation*, vol. 51, no. 10, pp. 2572-2581, Oct. 2003.

[18] A. Radkovskaya, M. Shamonin, C. Stevens, G. Faulkner, D. Edwards, E. Shamonina, and L. Solymar, "Resonant frequencies of a combination of split rings: experimental, analytical and numerical study," *Microwave and Optical Technology Letters*, vol. 46, no. 5, pp. 473-476, 2005.

Qianyin Xiang received the B.Eng. degree in Communication Engineering and Ph.D. degree in Communication and Information Systems from Southwest Jiaotong University (SWJTU), Chengdu, China, in 2005 and 2013, respectively. Dr. Xiang is a member of the *Institute of Electrical and Electronics Engineers (IEEE)* and *IEEE Microwave Theory and Techniques Society (MTT-S)*. His research interests include Analog/RF /Microwave circuits and systems, and tunable/software defined devices.

Quanyuan Feng received the M.Sc. degree in Microelectronics and Solid Electronics from the University of Electronic Science and Technology of China (UESTC), and the Ph.D. degree in Electromagnetic Field and Microwave Technology from Southwest Jiaotong University (SWJTU), Chengdu, China, in 1991 and 2000, respectively. Professor Feng has been honored as the "Excellent Expert" and the "Leader of Science and Technology" of Sichuan for his outstanding contribution. He is the Reviewer of more than 20 journals, such as *IEEE Trans. Vehic. Tech.*, *IEEE Trans. Magn.*, *IEEE Magn. Lett.*, *IEEE Microw. Wireless Compon. Lett.*, *Chinese Physics*, *Acta Physica Sinica*, etc. He is the recipient of the "First Class Award of Scientific and Technologic Progress of Sichuan Province," "Third Class Award of Scientific and Technologic Progress of Electronic Industry Ministry," "National Mao Yisheng Scientific and Technologic Award of Chinese Scientific and Technologic Development Foundation".

His research interests include power electronics, antennas and propagation, integrated circuits design, electromagnetic compatibility and environmental electromagnetics, microwave materials and devices.

Xiaoguo Huang received the B.Eng. degree in Microelectronics from Southwest Jiaotong University (SWJTU), Chengdu, China, in 2008, where he is currently working toward his Ph.D. degree. His research interests include passive circuit design, tunable filters, and metamaterials.

A Compact Planar 90° Branch Line Coupler Using S-Shaped Structure Loading for Wideband Application

M. Maleki [1], J. Nourinia [2], Y. Zehforoosh [3], and V. Rafii [3]

[1] Department of Electrical Engineering
Ahar Branch, Islamic Azad University, Ahar, Iran
mostafa.maleki.k@gmail.com

[2] Department of Electrical Engineering
Urmia University, Urmia, Iran
j.nourinia@urmia.ac.ir

[3] Department of Electrical Engineering
Urmia Branch, Islamic Azad University, Urmia, Iran
y.zehforoosh@srbiau.ac.ir, vhd.rafii@gmail.com

Abstract ─ This paper presents the design of a wideband microstrip branched branch line coupler (BLC). The wideband performance of the BLC means that it possesses equal coupling and difference of phases throughout the operating frequency band, from 4 GHz to 6 GHz (based on a 10 dB, i.e., VSWR ≤ 2). The compactness of the proposed design is depending on the replacement of the branched transmission lines (TL) instead of the ordinary TLs. Small and easy to fabricate microstrip layout topology for the BLC has been designed and constructed relying on a low cost dielectric material, the well-known FR4. In addition, the proposed coupler can be easily fabricated on the printed circuit board without any lumped element. The proposed BLC exhibits couplings and phase errors within −3.75 ± 1 dB and 4° over a 60 % bandwidth (BW) with a center frequency of 5 GHz (based on 15 dB).

Index Terms ─ Compact, coupler, microstrip, planar, and wideband.

I. INTRODUCTION

The compact BLC is an important circuit in microwave integrated circuits and can be used as a power divider/combiner or a part of a mixer [1]. The conventional BLC was composed of four quarter-wavelength TLs [2]. However, adopting the quarter-wavelength TL to design the coupler takes too much space; therefore, larger circuit area may result in higher cost. In addition, the broadband BLC takes two times more space than the normal type.

Numerous methods have been proposed to reduce the circuit size [3-7]. A number of proposed methods are as follows: based on a methodology, the asymmetrical T-structure can be exactly synthesized and then applied to implement compact planar couplers [3]. A class of the novel compact-size BLCs using the quasi-lumped elements approach with symmetrical or nonsymmetrical T-shaped structures is proposed in [5, 6]. Nevertheless, using the lumped element in the circuit design requires an empirical model, such as an inductor model, attained via precise measurement. Based on another methodology, discontinuous microstrip lines whose size is significantly reduced relative to the standard design can be used to implement a compact planar coupler [3]. By using the inter digitized capacitors shunt with the TLs, further minimization of the 3 dB branch-line hybrid coupler can be achieved compared with previously reported techniques [4].

In [3-8] microstrip lines are employed to design the compact BLC. However, only a few studies provide detailed discussion on design

Submitted On: Feb. 4, 2013
Accepted On: May 14, 2013

procedures or formulations. In this paper, a new method for designing the microstrip BLCs with predetermined compact size and BW has been proposed and implemented. Utilizing the proposed multiple shunted open stubs shown in Fig. 1 (e), which can be realized with either high or low impedance, that can easily miniaturize the TLs of branch-line. The fabricated couplers not only occupy small space, but also reveal good circuit performances compared with that of the conventional branch-line type, and it can be used as an element of broadband Butler matrix networks to feed an array antenna. Good agreements between the results of the conventional and proposed BLC are observed.

In the next section, we will provide the transformed equation, which can synthesize the equivalent quarter-wavelength TL. Then the comparison between the theoretical predictions and measurements. Finally, conclusions are given in the last section.

II. DESIGN PROCEDURE

The desired 90° BLC should have a good performance such as return loss and isolation better than 20 dB over 50 % or wider BW (total BW measured based on 10 dB), and a small size on a single-layer circuit without using any air-bridges (planar structures) [7].

In order to enhance the BW, we choose cascaded branch line, broadband BLC as a quadrature hybrid circuit. However, it requires a large circuit area. The loaded line is a popular method to reduce the size of TL circuits such as branch-line and ring hybrids, which is important for planar integrated circuits. The results using a loaded line show good efficiency with regard to size reduction [7].

A TL and its π-equivalent circuit are shown in Fig. 1, and the design equations can be defined as follows [7],

$$\frac{\tan\theta_P}{Z_P} = \frac{\cos\theta_S - \cos\theta_0}{Z_0 \sin\theta_S} \tag{1}$$

$$Z_S = \frac{Z_0 \sin\theta_0}{\sin\theta_S}, \tag{2}$$

where $0 \le \theta_S \le \theta_0 \le 90°$.

For demonstration, we select a TL of Fig. 1 (a) with the characteristic impedance Z_0 and electrical length θ_0 as a unit line section, and it can be replaced by a π-equivalent circuit in Fig. 1 (b). Then each open stub can be replaced by a folded open stub with equal characteristic impedance Z_P and total electrical length θ_P (i.e., $\theta_P = \theta_P' + \theta_P''$) as shown in Fig. 1 (c) and d, and in order to approach more size reduction one of the folded stubs can be flipped vertically (with a 45° corner) as shown in Fig. 1 (d). Finally, the approached structure is a balanced π-equivalent with S-shaped stubs as called S-shaped equivalent as shown in Fig. 1 (e). Due to the simulated and measured results, which are presented in the next section, this structure has an acceptable frequency response within the operating band width with regard to size reduction.

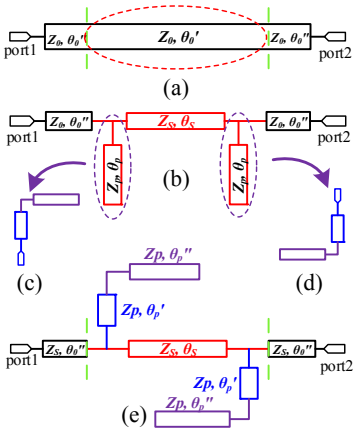

Fig. 1. Conventional TL and its S-shaped equivalent structure for (a) a conventional TL, (b) quasi π-equivalent TL of the conventional type, (c) folded equivalent structure of the open stub, (d) flipped vertically and folded equivalent structure of the open stub, and (e) the S-shaped equivalent structure of the conventional TL.

If the TLs of the conventional (broadband) BLC shown in Fig. 1 (a) are replaced by S-shaped equivalent structure shown in Fig. 1 (e). The open stubs on the corners should be merged together, in order to avoid being the stubs on the corner, one can replace a fraction of the conventional TLs of the couplers by the S-shaped equivalent structure as shown in Fig. 1 (e). Due to simulation results, presented in the next section, by an acceptable approximation, the rest fraction of each TL can be replaced by the conventional TL with the same electrical length, but with the characteristic impedance Z_S instead of Z_0. This replacement results in a flatter structure as shown in Fig. 1 (e).

The proposed circuit has been shown in Fig. 2 and each conventional TL has been replaced by an S-shaped equivalent structure. Length and width of each intersection transmission line lettered in Fig. 2 are listed in Table 1.

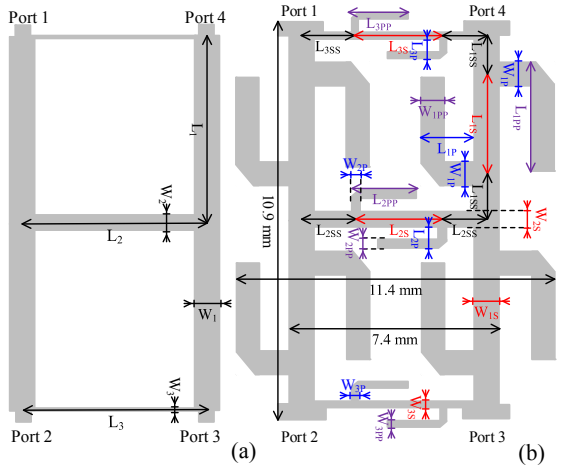

Fig. 2. (a) The conventional broadband BLC and (b) the proposed broadband BLC with S-shaped equivalent structure. (The figures are not scaled to the real size, the conventional type is larger.)

Table 1: Length and width of each intersection lettered in Fig. 2 (all values are in mm).

	L_i	W_i	L_{iSS}	L_{iS}	W_{iS}	L_{iP}	W_{iP}	L_{iPP}	W_{iPP}
i=1	8.10	1.70	0.85	3.40	0.70	2.05	0.80	3.75	0.80
i=2	10.6	0.80	1.75	3.20	0.30	0.65	0.20	2.43	0.20
i=3	10.6	0.25	1.75	3.20	0.10	0.30	0.10	1.85	0.10

III. SIMULATION AND EXPERIMENTAL RESULTS

Simulation was accomplished using EM simulation software Agilent Advanced Design System (ADS), which is an electromagnetic wave simulator that provides an integrated design environment to the designers of RF electronic products. The proposed BLC is designed on an FR4 substrate with a thickness of 0.8 mm, a dielectric constant of 4.4, and a loss tangent of 0.022. Figure 2 presents the layout of the proposed microstrip BLC with S-shaped TLs and its effective size is 10.90 mm × 7.40 mm (outer stubs are neglected [7], total size is 10.90 mm × 11.40 mm). The simulation results of the return loss, isolation, and coupling and insertion loss of the proposed BLC are shown in Fig. 4 and the phase division is shown in Fig. 5. At the designed frequency, 5 GHz, the insertion loss is -3.5 ± 0.1 dB, the isolation is about 20 dB, and the phase difference is 90°. In addition, these figures show that the performance of the proposed coupler has approximately couplings and phase errors within −3.75 ± 1 dB and 4° and return loss and isolation better than 15 dB over a 60 % BW. Table 2 summarizes the recently published branch-line hybrid couplers with reduced wavelength in TL and this work. In addition, it shows significant improvement in size reduction with regard to wide band performance.

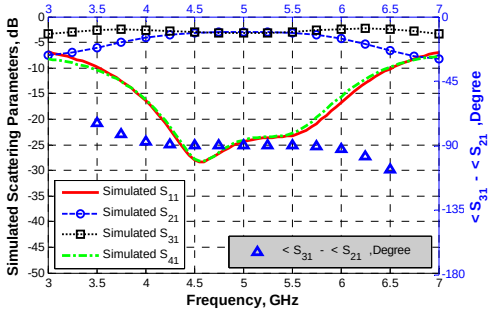

Fig. 3. Scattering parameters of the conventional BLC.

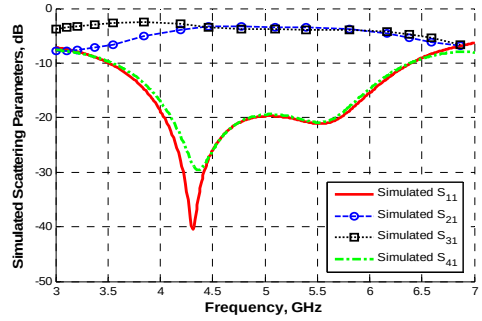

(a)

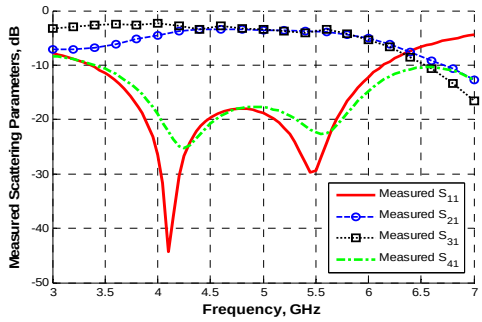

(b)

Fig. 4. Scattering parameters of the proposed BLC, (a) simulated scattering parameters and (b) measured scattering parameters.

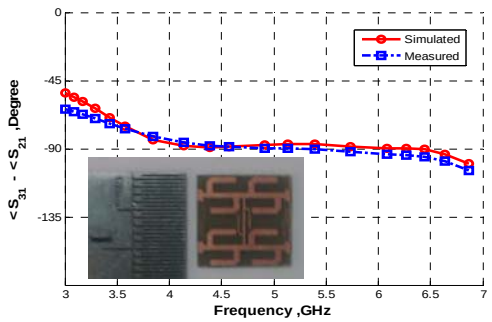

Fig. 5. Measured and simulated phase difference between S_{31} and S_{21} of the proposed BLC, and its photograph.

Table 2: Comparison of published compact BLC and this work.

Ref.	Phase Error	Substrate	f_0 (GHz)	B.W. (GHz) (based on 10dB)	Reduction Ratio
[3]	~5	RO4003	0.9	0.3 (0.75~1.05)	0.12
[4]	~2	FR4	0.825	0.15 (0.75~0.9)	0.26
[5]	>5	RO4003	2.4	0.4 (2.2~2.6)	0.76
[6]	>5	FR4	2.4	0.8 (2~2.8)	0.29
[7]	~5	RO4003	5	2 (4~6)	0.5
This Work	4	FR4	5	2 (4~6)	0.39

IV. CONCLUSION

This paper, the conventional broadband BLC (cascaded BLC) with seven sections of the quarter-wavelength TLs has been miniaturized easily by using the proposed S-shaped equivalent structure. The corresponding design equations, equivalent structures, and their simulated and measured results are presented as well. Table 2 reveals that using the proposed S-shaped equivalent structure is an effective approach to miniaturize the circuit size of a BLC (i.e., the reduction size is 61 %) with regard to wideband performance. The proposed BLC exhibits couplings and phase errors within −3.75 ± 1 dB and 4° and return loss and isolation better than 15 dB over a 60 % BW with a center frequency at 5 GHz. Moreover, these couplers can be fabricated using a standard printed circuit board process, which is easily applicable to the design of microwave integrated circuits, such as broadband Butler matrix networks.

REFERENCES

[1] S. A. Maas, *Microwave Mixers*, Norwood, MA: Artech House, 1986.

[2] D. M. Pozar, *Microwave Engineering,* 3rd Ed, New York: John Wiley & Sons, 2005.

[3] C. H. Tseng and C. L. Chang, "A rigorous design methodology for compact planar branch-line and rat-race couplers with asymmetrical T-structures," *IEEE Transactions on Microwave Theory and Techniques*, vol. 60, no. 7, pp. 2085-2092, July 2012.

[4] K. Y. Tsai, H. S. Yang, J. H. Chen, and Y. J. E. Chen, "A miniaturized 3 dB branch-line hybrid coupler with harmonics suppression," *IEEE Microwave and Wireless Components Letters,* vol. 21, no. 10, pp. 537-539, Oct. 2011.

[5] C. W. Tang, M. G. Chen, and J. W. Wu "Realization of ultra-compact planar microstrip BLCs with high-impedance open stubs," *IEEE Microwave Symposium, 2007.*

[6] S. S. Liao and J. T. Peng "Compact planar microstrip BLCs using the quasi-lumped elements approach with nonsymmetrical and symmetrical T-shaped structure," *IEEE Transactions on Microwave Theory and Techniques,* vol. 54, no. 9, Sep. 2006.

[7] C. Chen, H. Wu, and W. Wu "Design and implementation of a compact planar 4×4 microstrip Butler matrix for wideband application," *Progress in Electromagnetics Research C,* vol. 24, pp. 43-55, 2011.

[8] A. Yilmaz, E. Cetiner, and M. Hasanovic, "Sonnet modelling and simulation of broadband branchline coupler," *27th Annual Review of Progress in Applied Computational Electromagnetics (ACES),* Williamsburg, Virginia, pp. 398-402, March 2011.

Mostafa Maleki was born in Urmia, Iran, in 1985. He received the B.Sc. degree in Electrical and Communications Engineering from Urmia Azad University, Urmia, Iran, in 2008 and M.Sc. degree in Electrical Engineering from Ahar Azad University,Ahar,Iran, in 2013. He is with the Northwest Antenna and Microwave Research Laboratory (NAMRL). His current research interests include RF amplifiers, RF filters, microwave components and high-frequency networks.

Javad Nourinia was born in Urmia, Iran, in 1969. He received the M.Sc. and Ph.D. degree in Electrical Engineering from Iran University of Science and Technology, Tehran in 1995 and 2000, respectively. He is now a Professor of Electrical Engineering at the university of Urmia and head of Electronics and Communication Department.

Yashar Zehforoosh was born in Urmia, Iran, in 1981. He received his Ph.D. degree from Science and Research Branch of Islamic Azad University Tehran, Iran in 2012. His research interests include broadband antennas, electromagnetic structures and UWB systems.

Vahid Rafii was born in Urmia, Iran, in 1986. He received the B.Sc. degree in Communication Engineering from the Urmia Azad University, in 2008 and M.Sc. degree in Communication Engineering from Urmia University, Urmia, Iran, in 2013. His research interests include antenna array, array feed networks, and their antenna applications.

A Compact Stacked-Patch Endfire Antenna for WiFi Application

Yuanhua Sun[1], Guangjun Wen[1], Ping Wang[1, 2], Yongjun Huang[1], and Zhibo Du[3]

[1] Centre for RFIC and System Technology, School of Communication and Information Engineering
University of Electronic Science and Technology of China, Chengdu, 611731, China
sunyuanhua17@gmail.com

[2] College of Electronic and Information Engineering, Chongqing Three Gorges University, Chongqing, 404000,China
wangpingcqz@163.com

[3] Chengdu University of Information Technology, Chengdu, 610225, China
du139123456789@163.com

Abstract ─ The new stacked-patch endfire antenna is proposed for wireless fidelity (WiFi) access point and base station. The proposed using three copper patches is presented. The new antenna uses easily fabrication. The advantage of the endfire antenna with three patches compared to the conventional Yagi antenna is a reduction in the length of the antenna and the dimension of the antenna is 0.504 λ × 0.664 λ × 0.075 λ mm^3. The antenna has a gain of 9 dB, return loss better than -10 dB around the WiFi band from 2.4 GHz to 2.483 GHz and the front-to-back can achieve 15 dB. We described the antenna structure and presented the comparison of simulation results with experimental data. The proposed antenna is fabricated, and measured reflection coefficient, radiation patterns, and gain are presented.

Index Terms ─ Endfire antenna, stacked-patch antenna, and wireless fidelity.

I. INTRODUCTION

Wireless fidelity (WiFi) has become the standard for wireless local area network (WLAN) communication in 2.4 GHz industrial, scientific, and medical bands, with frequency ranges from 2.4 GHz to 2.483 GHz. WiFi provides wireless network communications between computers and other portable devices by fixed access points over a short distance, typically in the order of tens of meters through WLANs. The antenna is an important part in the WiFi system.

WiFi antenna can be categorized into three groups, namely, designs for mobile applications, outdoor, and indoor. For each group, the antenna design features specific requirements: antennas for mobile devices provides omnidirectional coverage with an average gain from -5 to 5 dB. The physically and electrically small antennas are required also [1-3]. Outdoor antennas include directional patch antenna arrays and highly directional Yagi antennas [4]. Indoor antennas can provide directional/omnidirectional coverage with gain from 2 dB to 6 dB. These patch or monopole antennas are usually mounted on walls and ceilings. A small-form or low-profile design is important because of the limited space and aesthetical concerns [5-7]. However, some of them do not have the directional radiation, and have low gain. The conventional directional antennas such as Yagi antennas have high gain, but they have large dimensions.

In this paper, we propose a compact endfire antenna for WiFi applications. The advantages of the proposed antenna is more compact than the conventional Yagi antenna. The proposed antenna is designed to cover the IEEE 802.n band from 2.4 GHz to 2.483 GHz with endfire performance and impedance matching. Meanwhile, the antenna configuration is simple and easy for fabrication. Also, the return loss, gain, and radiation pattern of

Submitted On: Sep. 2, 2012
Accepted On: May 16, 2013

the manufactured prototype has been measured. From the measured results, there is agreement between simulation and measurement.

II. ANTENNA CONFIGURATION

Similar to the conventional Yagi antenna, Fig. 1 shows the geometry of the proposed antenna. The final antenna parameters are optimized using the commercial electromagnetic (EM) solver HFSS 13.0, and are given in the table 1. The antenna is designed for WiFi access point and basic station in the frequency range of 2.4 GHz - 2.483 GHz

The theory of the proposed antenna is on basic of the conventional Yagi antenna. The antenna comprises of two suspended patches and a ground patch. The main radiating patch is directly fed by an SMA connector, which is connected to the RF input and simplifies the antenna structure. A parasitic patch is positioned right above the main radiating patch for enhancing the bandwidth and gain. Air substrate among three copper patches is used to achieve high gain and low cost. The main radiating patch is suspended above the ground plane. The input impendence of the patch and its resonance frequency can be tuned by adjusting the parameters of the dimension of the patches giving freedom for optimization. The antenna has directional radiation pattern, high gain, and higher terminal impedance.

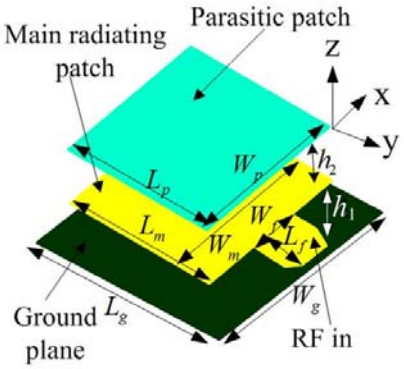

Fig. 1. The designed stacked-patch antenna geometry.

The finally chosen dimension of the proposed antenna are illustrated in table 1. The proposed antenna is designed based on the basic Yagi-Uda antenna principle, consists of two radiating patches. Both patches were shaped to fit into the available dimension while maintaining their resonant frequencies in the desired band. Key parameters in the design are their mutual spacing. The antenna was tuned to achieve 50 ohm impedance without using any external matching circuit that will occupy additional space.

For demonstration purpose in the laboratory, the proposed antenna was designed using three 0.44 mm thickness copper patches. The overall dimension of the antenna is 63 × 83 × 9.32 mm^3, or equivalently roughly 0.504 λ × 0.664 λ × 0.075 λ mm^3.

Table 1: The dimensions of the antenna (in mm).

L_g	W_g	L_m	W_m	L_p
63	83	53	56	53
W_p	L_f	W_f	h_1	h_2
43	16	18.5	5	3

III. SIMULATION AND MEASUREMENT

To verify the proposed antenna design, a prototype is fabricated as shown in Fig. 2, and the results are presented here. All the measured results are carried out in anechoic chamber using a vector network analyzer (VNA) and other microwave test instruments.

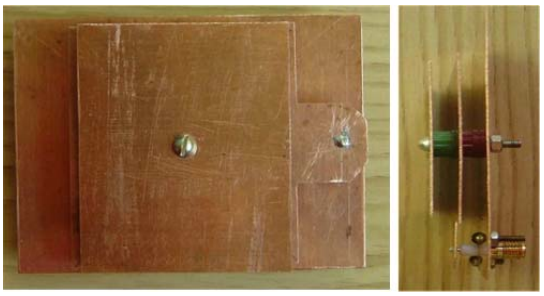

(a) (b)

Fig. 2. Stacked-patch antenna prototype; (a) top view and (b) side view.

All simulations were performed by Ansoft high-frequency structure simulation (HFSS) based on the finite-element method (FEM) [8, 9]. The simulated and measured antenna magnitude of S_{11} are shown in Fig. 3. The simulation was performed by HFSS 13.0 and the measurement was taken by an Agilent performance network analyzer.

As shown in Fig. 3, there is a good agreement between the simulation and measurement results and a bandwidth of 250 MHz is obtained. The measured resonance frequency is slightly shifted down in frequency compared to the simulation, owing to fabrication tolerances using the copper patches and soldering the connector. The measured XZ- and YZ- planes radiation pattern and 3D radiation at 2.4 GHz and 2.483 GHz are illustrated in Figs. 4 (a) and (b), respectively. The radiation patterns are measured in a 7 × 3 × 3 m^3 anechoic chamber and the measurement is performed by an Agilent network analyzer along with far-field measurement software. In the measurement the connecting cables along the Bakelite support ware carefully shielded by absorbers to reduce the multi-reflection interference. Meanwhile, the simulated -10 dB reflection coefficient bandwidths are from 2.32 GHz to 2.5 GHz and the corresponding measurement data are given by 2.35 GHz -2.5 GHz. The current distribution at 2.45 GHz is shown in Fig. 5. The experimental results demonstrate that the proposed design completely complies with the stringent requirement of impedance matching imposed on WiFi antenna, and the operating bandwidth with return loss is better than -10 dB and covers the whole allocated spectrum for WiFi applications.

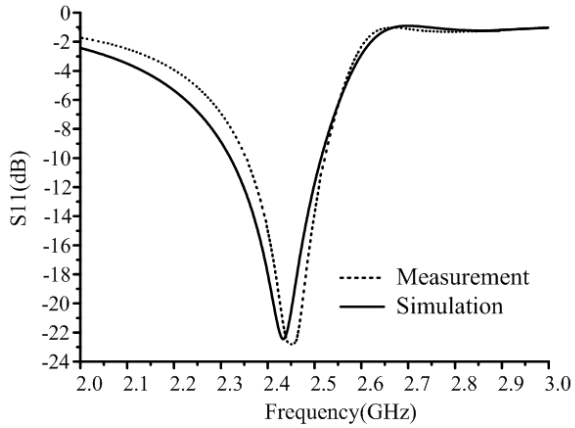

Fig. 3. S11 simulation and measurement results.

For ease of practical applications, the studies of an important parameters of the distances between patches and is also performed by simulations. One parameter is changed, while the other parameters are kept as in table 1. Figure 6 shows the return loss (S11) and gain of the proposed antenna corresponding to different distances between the radiation patch and ground patch (h_1). As shown in Fig. 6 (a), it is observed that there is one resonant frequency, and the resonant frequency is decreased from 2.49 GHz to 2.35 GHz when h_1 is increased from 3 mm to 9 mm. Figure 6 (b) shows the gain of the proposed antenna do not change when h_1 increases from 1 mm to 7 mm. As the value of the distance between the parasitic patch and the main radiating patch (h_2) increases, as shown in Fig. 7, there is one resonant frequency, the resonant frequency decreases from 2.65 GHz to 2.25 GHz when h_2 increased from 1 mm to 7 mm, and the gain decreased in range from 2.4 GHz to 2.5 GHz.

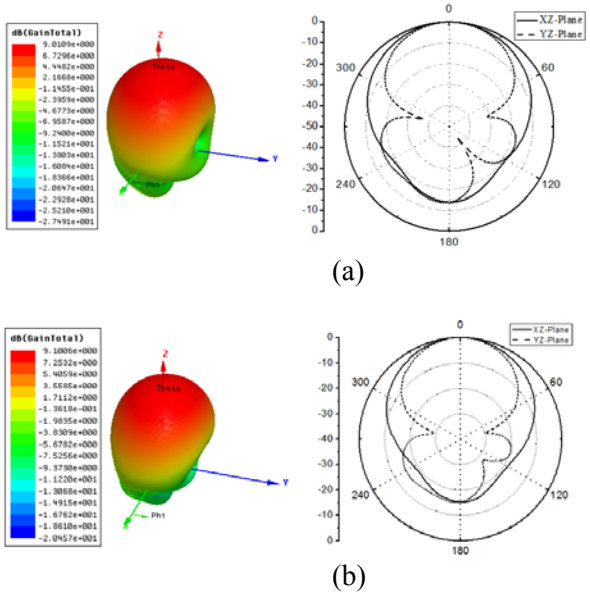

(a)

(b)

Fig. 4. The radiation pattern of the stacked-patch antenna at (a) 2.4 GHz and (b) 2.483 GHz.

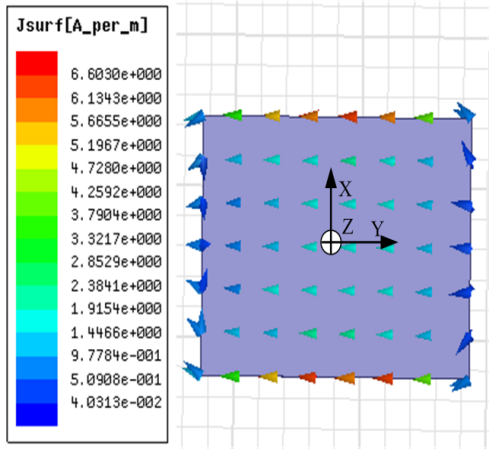

(a)

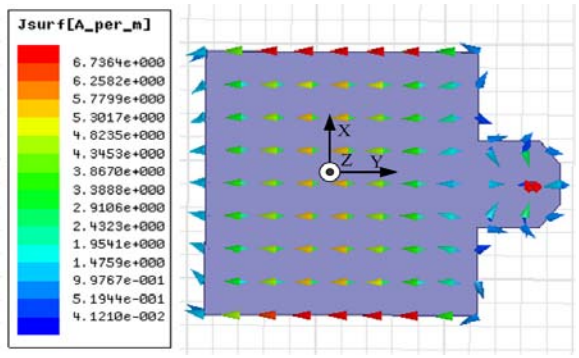

(b)

Fig. 5. The current distribution at 2.45 GHz for (a) the parasitic patch and (b) the main radiating patch.

The gain of the antenna was measured using the gain comparison method [10], where the received power of the antenna under test is compared with known gain of a standard horn antenna. The simulated and measured gain and efficiency are shown in Fig. 8, variation between the simulated and measured gain is within 0.5 dB, and this may be due to losses of patches. The referring to Fig. 3, measured results can be observed over the frequency band of interest. Clearly, Fig. 4 shows the radiation patterns similar to the conventional Yagi radiation characteristics.

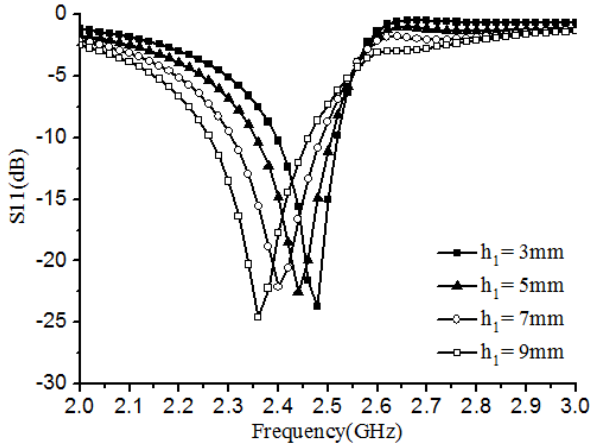

(a)

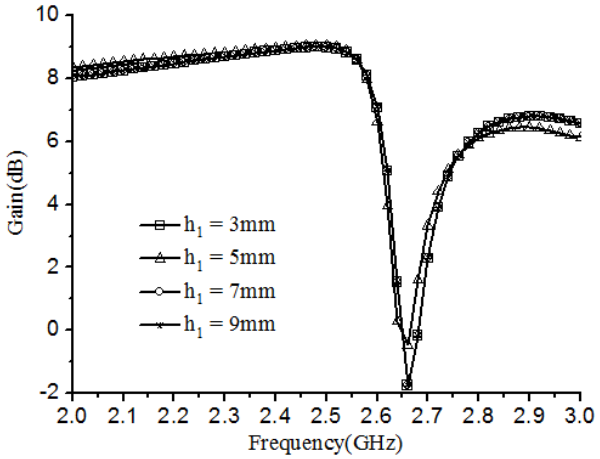

(b)

Fig. 6. Effect of the height of the main radiating patch h_1 on the antenna performance on the (a) return loss and (b) gain.

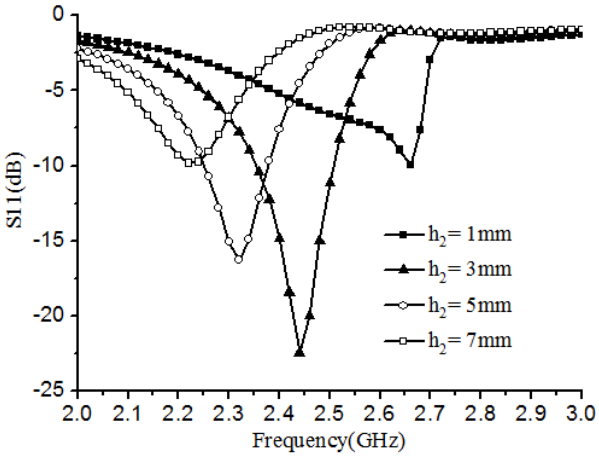

(a)

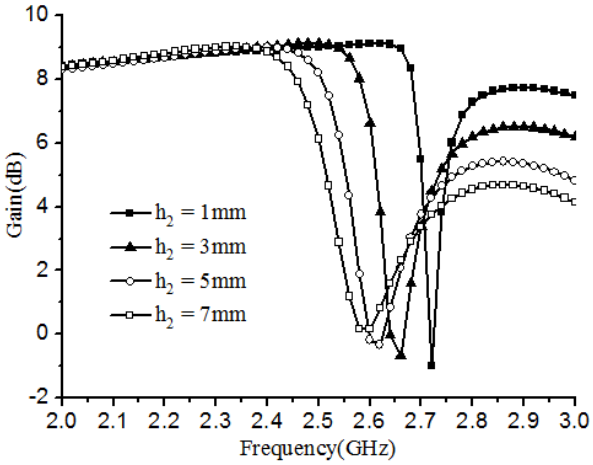

(b)

Fig. 7. Effect of the height of the parasitic patch h_2 on the antenna performance on the (a) return loss and (b) gain.

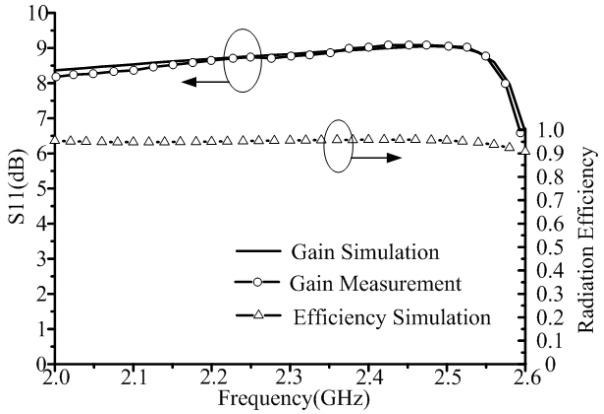

Fig. 8. Simulated, measured gain in the Z-direction and the simulated efficiency of the antenna.

The measured front-to-back ratio is at least 15 dB at 2.4 GHz and reaches 9 dB and remains better than 9 dB over the whole WiFi band from 2.4 GHz to 2.483 GHz. Adding director elements can increase the front-to-back ratio, but on the other hand they will increase the dimensions of the antenna. The measured bore sight gain is illustrated in Fig. 8. Referring to Fig. 8, the antenna gain steadily achieve 9 dB from 2.4 GHz to 2.483 GHz. The efficiency of the proposed antenna steadily achieve above 90 %.

IV. CONCLUSIONS

In this paper, we proposed a stacked-patch endfire antenna for WiFi applications. The proposed antenna is suitable for fabrication. The antenna is based on the conventional Yagi antenna, the input impendence of the antenna can be tuned by properly adjusting the distances of three patches giving freedom for optimization. The antenna configuration, design, simulated, and measured results have been well discussed. The experimental results reveal that the proposed antenna features a compact size of 0.504 $\lambda \times 0.664$ $\lambda \times 0.075$ λ, wide -10 dB return loss bandwidth can cover 150 MHz, high gain among 8.5 dB to 9 dB and have good directional radiation patterns. Good return loss and radiation pattern characteristics are obtained and measured results are presented to validate the usefulness of the proposed antenna structure for wireless fidelity (WiFi) applications.

ACKNOWLEDGMENT

This work is supported by Research Fund for the Doctoral Program of Higher Education of China (Grant No 20110185110014).

REFERENCES

[1] Z. N. Chen, *Antennas for Portable Devices*, London, U.K.: Wiley, March 2007.

[2] C. C. Lin, L. C. Kuo, and H. R. Chuang, "A horizontally polarized omnidirectional printed antenna for WLAN applications," *IEEE Trans. Antennas Propag.*, vol. 54, no. 11, pp. 3551-3556, Nov. 2006.

[3] R. A. Rahim, S. I. S. Hassan, F. Malek, M. N. Junita, M. F. Jamlos, and M. N. Azizan, "2.45 GHz harmonic suppression rectangular patch antenna," *IEEE Symposium on Computer Applications and Industrial Electronics (ISCAIE),* pp. 242-246, 2012.

[4] Z. N. Chen and K. M. Luk, *Antennas for Fixed Base-Stations in Wireless communications*, New York: McGraw Hill, May 2009.

[5] H. Nakano, H. Iwaoka, K. Morishita, and J. Yamauchi, "A wide band low-profiled antenna composed of a conducting body of revolution and a shorted parasitic ring," *IEEE Trans. Antennas Propagat.*, vol. 56, no. 4, pp. 1187-1192, Apr. 2008.

[6] P. Callaghan and J. C. Batchelor, "Dual-band pin-patch antenna for WiFi applications," *IEEE Antennas and Wireless Propagation Letters,* vol. 7, pp. 1757-1760, 2008.

[7] D. Wu, M. Zhao, Y. Fan, and Y. Zhang, "A wide band 8-elements omnidirectional array for wireless system," *Microwave and Optical Technology Letters*, vol. 49, no. 12, pp. 2944-2946, Dec. 2007.

[8] K. Elmahgoub, T. Elsherbeni, F. Yang, A. Z. Elsherbeni, L. Sydänheimo, and L. Ukkonen, "Logo-antenna based RFID tags for advertising application," *Applied Computational Electromagnetics Society (ACES) Journal*, vol. 25, no. 3, pp. 174-181, Mar. 2010.

[9] HFSS: High Frequency Structure Simulator Based on the Finite Element Method.

[10] C. A. Balanis, *Antenna Theory: Analysis and Design*, John Wiley & Sons, Inc., New York, 2nd ed., 1997.

Yuanhua Sun received the B.Sc. degree in Communication Engineering from the Liaocheng University in 2007, and M.Sc. degree in Signal and Information Processing from Chengdu University of Information Technology in 2010. He is working toward the Ph.D degree in UESTC. His research interests include analytical and numerical modeling of metamaterials and antenna theory and design and signal processing.

Guangjun Wen was born in Sichuan, China, in 1964. He received his M.Sc. and Ph.D. degrees in Chongqing University of China in 1995 and UESTC in 1998, respectively. He is currently a Professor and doctor supervisor in UESTC.

His research and industrial experience covers a broad spectrum of electromagnetics, including RF, microwave, millimeter wave integrated circuits and systems design for wireless communication, navigation, identification, mobile TV applications, RFIC/MMIC/MMMIC device modeling, system on chip (SoC) and system in package (SiC) design, RF/microwave/millimeter wave power source design, "The Internet of things" devices and system, RFID system and networks, antennas, as well as model of electromagnetic metamaterial and its application in microwave engineering area.

Ping Wang received the B.Sc. degree in Physics from Western Chongqing University of China in 2005 and the M.Sc. degree in Theoretical Physics from Chongqing University, Chongqing, in 2008. Currently, he is working toward the Ph.D. degree in UESTC. His current research interests include patch antennas, wideband antennas, and arrays.

Yongjun Huang received the B.Sc. degree in Mathematics from Neijiang Normal University of China in 2007, M.Sc. degree in Communication Engineering from University of Electronic Science and Technology of China (UESTC) in 2010, and is currently working toward a Ph.D. degree in UESTC. His research activities are electromagnetic metamaterial and its application in microwave engineering area, FDTD and CAD analysis for the metamaterial model and characteristics.

Zhibo Du received the B.Sc. degree in Computer Science and Technology from the Hebei University of Science and Technology in 2007, and M.Sc. degree in Computer Application from Chengdu University of Information Technology in 2010. He is working as assistant in Chengdu University of Information Technology. His research interests include application of antenna, and side channel attack on the security chip, for example electromagnetic attack, power attack and so on.

Compact Planar Super-Wideband Antenna with Band-Notched Function

H. Shahsavari[1], J. Nourinia[1], H. Shirzad[2], M. Shokri[3], S. Asiaban[3], Zh. Amiri[3], and B. Virdee[4]

[1]Department of Electrical Engineering,
Science and Research Branch, Islamic Azad University, Urmia, Iran
j.nourinia@urmia.ac.ir

[2]Young Researchers and Elite Club,
Urmia Branch, Islamic Azad University, Urmia, Iran
Hamedeshirzad@gmail.com

[3]Department of Electrical Engineering,
Urmia Branch, Islamic Azad University, Urmia, Iran
Majed.Shokri@gmail.com

[4]Faculty of Life Sciences and Computing,
Center for Communications Technology, London Metropolitan University, London, UK
b.virdee@londonmet.ac.uk

Abstract ─ In this paper, the design of a novel printed monopole antenna is presented that operates across a super wideband frequency range (2.39 GHz to 40 GHz) and exhibits band-notch characteristic that is necessary to eradicate interference from WLAN systems operating between 5.15 GHz ─ 5.825 GHz. The prototype antenna consists of a radiating patch in the shape of an octagonal ring structure and embedded within ring is a rectangular strip. The antenna is excited through a microstrip feed-line and includes an elliptically shaped ground-plane that is defected with a dielectric notch in the vicinity of the patch. The proposed antenna's structure is simple to design and is relatively inexpensive to fabricate. In addition, it is compact in size with overall dimensions of 30 × 30 × 1.6 mm^3. The measured results confirm the impedance bandwidth cover a super wideband frequency range from 2.3 GHz ─ 40 GHz, for VSWR ≤ 2 that corresponds to a fractional bandwidth of 178 %. The radiation characteristic of the proposed antenna is approximately omni-directional.

Index Terms ─ Band-notched antenna, monopole antenna, microstrip fed antenna, and planar structure.

I. INTRODUCTION

Recent development in wireless technology use multiple communications standards to enable various systems, e.g., satellite, ultra-wideband (UWB), and WLAN systems, to operate through a common platform. Such communication systems necessitate the integration of various sub-systems and require the use of a single antenna to enable wireless communication. The antenna therefore needs to be designed so that its impedance bandwidth is sufficiently wide enough to cover the operating frequency of multiple wireless communication systems. In fact, since the Federal Communications Commission (FCC) launched the bandwidth defined between 3.1 GHz – 10.6 GHz for UWB usage [1-12], the UWB technology has become the most promising candidate for the short-range, high-speed indoor data communications. Since printed monopole antennas have attractive features, namely: (i) relatively

Submitted On: Jan. 23, 2013
Accepted On: Apr. 7, 2013

large impedance bandwidth, (ii) ease of fabrication using conventional MIC technology, and (iii) acceptable radiation properties, hence these types of antenna find application in UWB systems [2, 3]. Unfortunately, within the UWB frequency band coexist other wireless narrowband standards such as WLAN bands (5.15 GHz – 5.35 GHz and 5.725 GHz – 5.825 GHz), which are likely to interference with the operation of UWB systems. This necessitates the need for additional functionality from UWB systems, i.e., a stop-band filter to mitigate the interference from such systems. However, this requirement would unnecessarily increase the size of UWB systems. In order to save space, the UWB antennas posses a notch function across the band 5.15 GHz – 5.825 GHz that would provide the solution. Band-notched UWB antennas with various filtering techniques have been recently proposed, which include: using H-shaped conductor-backed plane [4], cutting two modified U-shaped slots on the patch [5], inserting two rod-shaped parasitic structures [6], embedding resonant cell in the microstrip feed-line [7], using a fractal tuning stub [8], utilizing a small resonant patch [9], and using a MAM and genetic algorithm [10].

In this paper, a new single band notched super wideband (SWB) antenna is presented that uses a radiating patch consisting of an octagonal ring, in which is embedded a rectangular-shaped strip. The ring determines the center frequency of the notch band. The structure was optimized using a commercially available EM simulation tool, and the antenna was fabricated and its performance was verified.

II. ANTENNA STRUCTURE

The proposed monopole antenna was printed on a low-cost commercial FR-4 substrate with relative permittivity of 4.4, tanδ = 0.02 and thickness of 1.6 mm. Figure 1 shows the geometry of the proposed super wideband antenna. The antenna design is terminated with a 50 Ω SMA connector for signal transmission and reception. The width of the feed-line was fixed at 2.8 mm, which corresponds to a characteristic impedance of 50 Ω. The optimal dimensions of the antenna are shown in Fig. 1.

The antenna's structure includes a ground-plane with a notch in the shape of a semi-ellipse immediately below the octagonal ring patch. Within the patch is embedded a rectangular strip whose dimensions determine the frequency of the required notched band. Figure 2 shows the three steps employed to implement the antenna structure. The first step includes the radiating patch in the form of an octagonal ring, and ground-plane in the shape of a semi-circle. In the second step the ground-plane is defected with a semi-elliptical notch, which is located just below the octagonal ring. In the third step a rectangular strip is disposed vertically within the ring as shown in Fig. 2.

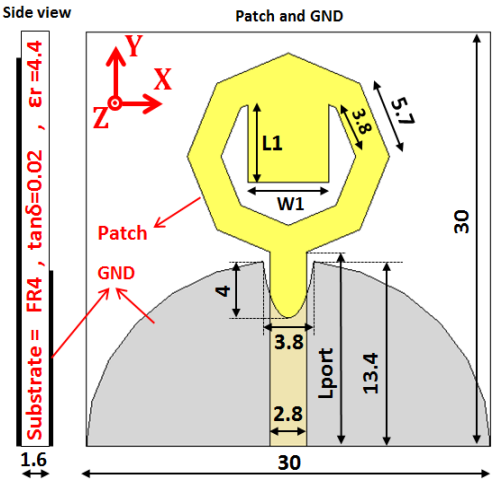

Fig. 1. Geometry of the proposed antenna (optimized dimensions in mm).

Figure 3 shows the microstrip antenna whose ground-plane is defected with a notch; provides a significantly wider impedance bandwidth match in comparison to the same antenna without the notch. In fact, super wideband impedance bandwidth is achieved between 2.39 GHz – 40 GHz, for VSWR ≤ 2. Also by inserting the rectangular strip within the octangular ring creates a narrow-band notch between approximately 5 GHz – 6 GHz.

III. SIMULATION RESULTS AND MEASUREMENTS

In this section, the affect of the various characterizing parameters on the band notched antenna are studied. Numerical and experimental results of the input impedance and radiation characteristics are presented and discussed. The parameters of this proposed antenna are studied by changing the salient parameters one at a time

while keeping all other parameters fixed. Full wave analyses of the proposed SWB antenna configuration was performed using commercial software, i.e., Ansoft HFSS (ver11.1). As shown in Fig. 4, adjusting the width (W1) of the rectangular strip can affect the antenna's notch frequency and to a lesser extend its bandwidth. The strip's length (L1) also affects the notch's center frequency as shown in Fig. 5. The change in the notch frequency is approximately 1 GHz for the length changing from 6.5 mm to 8.0 mm. Moreover, the length of the feed-line (Lport) plays an important role in the sharpness of the stop band. This effect is shown in Fig. 6, where the bandwidth and sharpness of the stop band frequency is controllable by changing Lport.

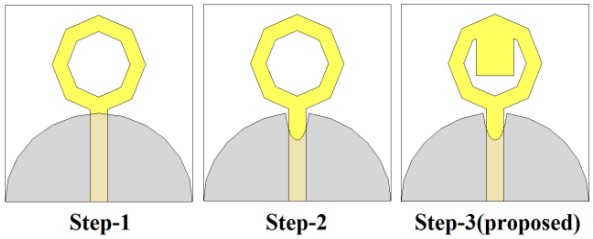

Fig. 2. Steps to create the proposed antenna structure: Step-1 is Antenna-1 with octagonal ring shaped patch and semi-circular ground-plane, Step-2 is Antenna-2 with defected ground-plane, and Step-3 is Antenna-3 with a rectangular strip embedded in the octagonal ring shaped patch.

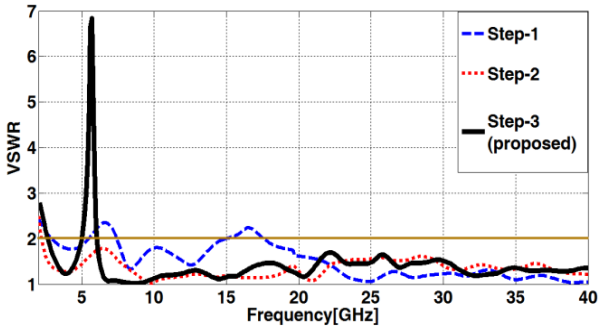

Fig. 3. Simulated VSWR characteristic of the antennas depicted in Fig. 2.

Figure 7 shows the simulated radiation patterns of the proposed antenna with the co- and cross-polarizations in the H-plane (x–z plane) and E-plane (y–z plane). It can be observed that the radiation patterns in the x–z and y-z planes are nearly omni-directional and bidirectional, respectively, at the frequencies of 5 GHz and 6.9 GHz.

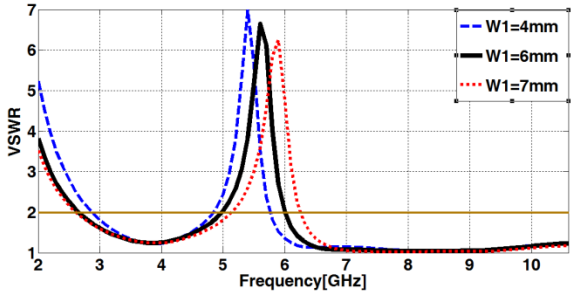

Fig. 4. Simulated VSWR characteristics of the proposed SWB antenna for various dimensions of W1.

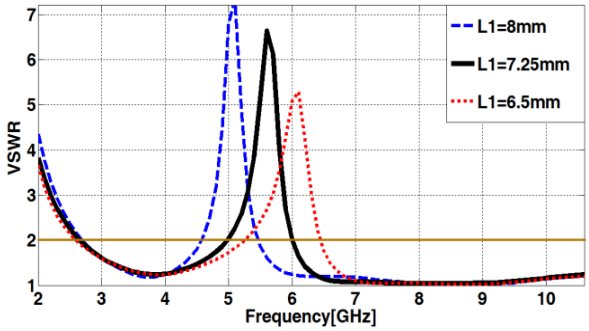

Fig. 5. Simulated VSWR characteristics of the proposed SWB antenna for various dimensions of parameter L1.

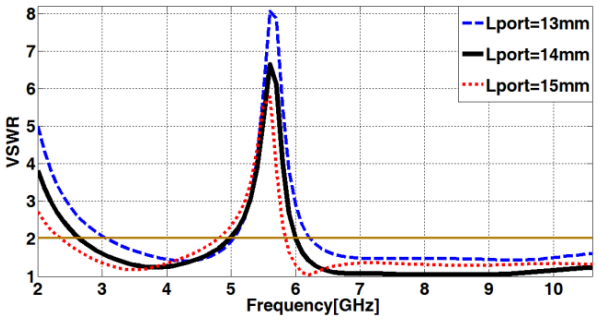

Fig. 6. Simulated VSWR characteristics of the proposed SWB antenna for various Lport lengths.

The measured and simulated gain of the proposed antenna over the antenna's operating bandwidth is shown in Fig. 8. The graph shows that the measured gain reaches a peak of around

3.5 dBi at 11 GHz. The gain as required drastically drops across the notch band.

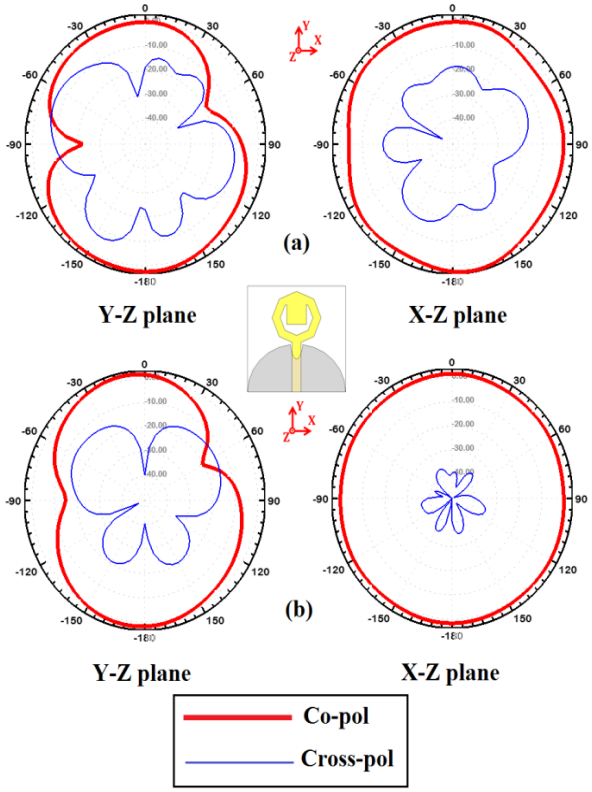

Fig. 7. Radiation patterns of the proposed antenna at (a) 5 GHz and (b) 6.9 GHz.

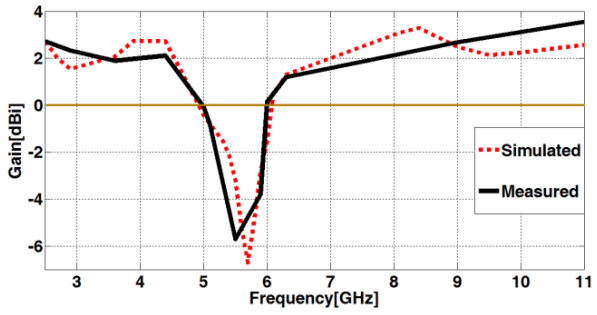

Fig. 8. Measured and simulated gain of the proposed SWB antenna.

The process contributing towards the SWB and notch band is explained by the current distribution density over the antenna. Figure 9 shows the current distribution at the notch's center frequency of 5.8 GHz, which is strong over the feed-line, the base of the octangular ring and the rectangular strip. The concentration is also strong over the defected ground-plane in the vicinity of the feed-line. The photograph of the proposed SWB antenna is shown in Fig. 10. The measured reflection-coefficient, shown in Fig. 11, verifies its outstanding performance up to 40 GHz. Both the impedance bandwidth and radiation patterns were measured by using the Agilent 8722ES network analyser in its full operational span (500 MHz – 40 GHz).

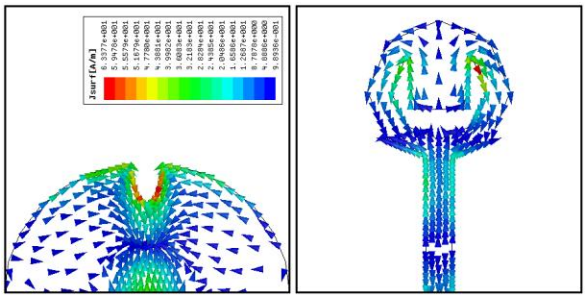

Fig. 9. Surface current density distribution of the proposed SWB antenna at 5.8 GHz over the defected ground- plane, feed-line, and the patch.

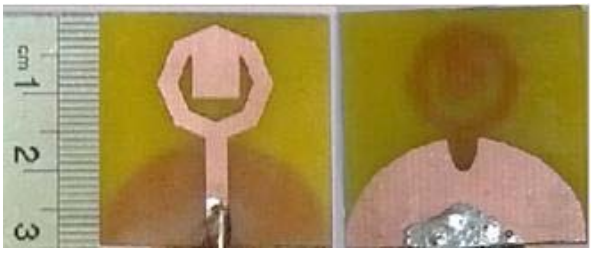

Fig. 10. Photograph of the front and back side of the SWB monopole antenna.

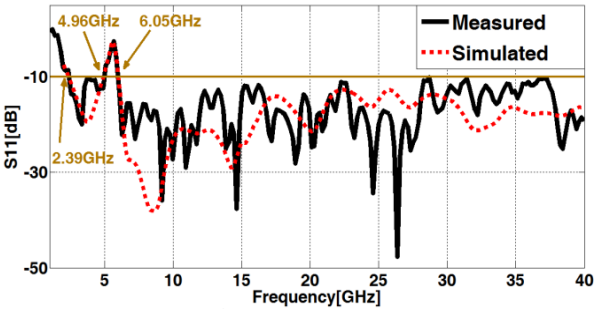

Fig. 11. Measured and simulated return-loss of the proposed antenna.

IV. CONCLUSION

Proof of concept is reported of a novel compact printed monopole antenna for super wideband applications. The antenna possesses a single band-notch characteristic necessary to mitigate interfering signals from WLAN systems. The proposed antenna has advantages of low-cost, compact size, and ease of fabrication. The measured results show an excellent 5 GHz – 6 GHz rejection band feature, super wideband performance (2.39 GHz – 40 GHz) and good radiation patterns in the UWB operating band. These characteristics make the antenna a viable choice for future SWB wireless applications.

REFERENCES

[1] Federal Communications Commission: First report and order, revision of part 15 of the Communication's rules regarding ultra-wide-band transmission system, 2002.

[2] R. Azim, M. T. Islam, and N. Misran, "Design of a planar UWB antenna with new band enhancement technique," *Appl. Comp. Electro. Society* (ACES) *Journal*, vol. 26, no. 10, pp. 856-862, Oct. 2011.

[3] J. Pourahmad azar, C. Ghobadi, J. Nourinia, and H. Shirzad, "Multiband ring fractal monopole antenna for mobile devices," *IEEE Antennas and Wireless Propagation Letters*, vol. 9, pp. 863-866, 2010.

[4] R. Zaker, C. Ghobadi, and J. Nourinia, "Novel modified UWB planar monopole antenna with variable frequency band-notch function," *IEEE Antennas and Wireless Propagation Letters*, vol. 7, pp. 112-114, 2008.

[5] M. Ojaroudi, G. Ghanbari, N. Ojaroudi, and C. Ghobadi, "Small square monopole antenna for UWB application with variable frequency band-notch function," *IEEE Antennas and Wireless Propagation Letters*, vol. 8, pp. 1061-1064, 2009.

[6] M. Rostamzadeh, S. Mohamadi, J. Nourinia, Ch. Ghobadi, and M. Ojaroudi, "Square monopole antenna for UWB applications with novel rod-shaped parasitic structures and novel V-shaped slots in the ground plane," *IEEE Antennas and Wireless Propagation Letters*, vol. 11, pp. 446-449, 2012.

[7] S. W. Qu, J. L. Li, and Q. Xue, "A band-notched ultra wide band printed monopole antenna, " *IEEE Antennas and Wireless Propagation Letters*, vol. 5, pp. 495-498, 2006.

[8] W. J. Lui, C. H. Cheng, Y. Cheng, and H. Zhu, "Frequency notched ultra-wideband microstrip slot antenna with fractal tuning stub," *Electronic Letters*, vol. 41, no. 6, pp. 294-296, March 2005.

[9] K. G. Thomas and M. A. Sreenivasan, "A simple ultra wideband planar rectangular printed antenna with band dispensation," *IEEE Transactions on Antennas and Propagation*, vol. 58, no. 1, pp. 27-34, Jan. 2010.

[10] J. Pourahmadazar, H. Shirzad, C. Ghobadi, and J. Nourinia, "Using a MAM and genetic algorithm to optimize UWB microstrip monopole antenna with FEM," *International Symposium on Telecommunications*, pp. 115-119, 2010.

[11] J. Pourahmadazar, Ch. Ghobadi, J. Nourinia, N. Felegari, and H. Shirzad, "Broadband CPW-fed circularly polarized square slot antenna with inverted-L strips for UWB applications," *IEEE Antennas Wireless Propagation Letters* vol. 10, pp. 369-372, 2011.

[12] J. Pourahmadazar, C. Ghobadi, and J. Nourinia, "Novel modified pythagorean tree fractal monopole antennas for UWB applications," *IEEE Antennas Wireless Propagation Letters*, vol. 10, pp. 484-487, 2011.

Hasan Shahsavari was born in 1977 in Iran. He received the B.Sc. degree in Electrical Engineering from IAU. He is currently working toward the M.Sc. degree in Electrical and Telecommunication Engineering in the Science and Research Branch of I A U, Urmia branch.

Javad Nourinia received his B.Sc. in Electrical and Electronic Engineering from Shiraz University and M.Sc. degree in Electrical and Telecommunication Engineering from Iran University of Science and Technology, and Ph.D. degree in Electrical and Telecommunication from University of Science and Technology, Tehran Iran in 2000. From 2000, he was an Assistant Professor and now he is an Associate Professor in the Department of Electrical Engineering of Urmia University, Urmia, Iran. His primary research interests are in antenna design, numerical methods in electromagnetic, and microwave circuits.

Hamed Shirzad was born on March, 1985 in Iran. He received the B.Sc. and M.Sc. degrees in Electrical Engineering from the IAU, and Urmia University in 2008, and 2012, respectively.

Majid Shokri was born on February, 1979 in Iran. He received the B.Sc. and M.Sc. degrees from the IAU, and Urmia University in 2001, and 2012, respectively, all in Electrical Engineering.

Somayeh Asiaban was born on September, 1984 in Iran. She received the B.Sc. degree from Urmia Branch, IAU in Electrical Engineering in 2008.

Zhaleh Amiri was born on January, 1981 in Iran. She received the B.Sc. degree from Urmia Branch, IAU in Electrical Engineering in 2005.

Bal Virdee is a Professor of Microwave Communications Technology in the Faculty of Life Sciences and Computing at London Metropolitan University where he Heads the Center for Communications Technology and is the Director of London Metropolitan Microwaves.

Ultra-Wideband Modified CSRR Antenna with Reconfigurable Notch Band

Di. Jiang, Bo. Yan, and Ruimin Xu

School of Electronic Engineering, University of Electronic Science and Technology of China,
Chengdu 611731, China
merryjiangdi@163.com

Abstract – A novel technique of realizing notches for a compact ultra-wideband (UWB) antenna is proposed based on a modified complementary split ring resonator (CSRR). The UWB slot antenna is in the swallow shape of a modified CSRR. The notched band centered at 5.8 GHz for upper WLAN and 3.9 GHz for C-band satellite communication systems. The proposed antenna has a compact size of 25 × 27.9 mm^2. The measured results show that the proposed antenna can guarantee a wide bandwidth from 2 GHz to 12 GHz (VSWR < 2) with dual unwanted band-notches successfully. The antenna demonstrates omnidirectional and stable radiation patterns across all the relevant bands. Moreover, a prototype of the dual-band-notched UWB antenna is fabricated and measured results are compared with simulated results.

Index Terms – Monopole antenna, multi-band antenna, and ultra-wideband (UWB) antenna.

I. INTRODUCTION

Ultra-wideband (UWB) links have been shown increasing applications in short-range and high-bandwidth communication and surveillance links [1]. Due to interference from other services, it is often desirable to block out narrow frequency bands from the UWB spectrum. The antenna is often tasked with providing both the wide frequency range and narrowband notch, which should be tunable within a certain range. Quarter-wavelength transmission lines or slots have been primarily used within antenna structures, ground plane or feed lines to suppress unwanted narrow-band signals [2-5]. In this paper, we present a compact printed antenna with 90 degrees rotation angle quadrilateral complementary split ring resonator (CSRR), which has an UWB operating bandwidth with a tunable dual-band-notched frequency at 3.9 GHz and 5.8 GHz [6]. Band-notched operation is achieved by embedding 90 degree rotation angle quadrilateral CSRR slots on radiated patch [7]. The CSRR under investigation can be used to implement left-hand materials. The 90 degrees rotation angle quadrilateral CSRR is promising for UWB antennas for ensuring multiple notched bands. Both dual-band-notched characteristics and compact size are achieved. The antenna has promising features, including good impedance matching performance over the whole operating frequency band, stable radiation patterns and flexible frequency notched function [8-10].

II. ANTENNA DESIGN

The proposed band-notched monopole antenna is shown in Fig. 1. The antenna consists of a notched swallow radiation patch and a trapezoidal ground plane that plays an important role in the broadband characteristics of this antenna because the electromagnetic coupling effects between the patch and the ground plane and improve its impedance bandwidth can be adjusted without any cost of size or expense [11]. To fabricate swallow-shaped antenna, a half ellipse is cut from a rectangle radiating patch firstly and then moved into the bottom side of the radiating patch. This new shape with a gradient structure has the same area as the rectangle shape radiating patch [12]. In addition, the ground of the antenna has a trapezoidal-like shape so that the ground also has a gradient structure. Since both the radiating patch and the ground have a gradient structure, the antenna can ensure a smooth transition from one

Submitted On: Oct. 31, 2012
Accepted On: May 19, 2013

mode to another. In this case, the antenna has an excellent impedance matching within a broad bandwidth rang [13]. The proposed antenna fed by a microstrip line is printed on RT5880 substrate with thickness of 0.508 mm and permittivity of 2.2. The width and length of the microstrip feed are fixed at 1.5 mm and 10.25 mm, respectively. The size of the inner-square (R_1, R_2) should be adjusted to determine the dual-band-notched frequency of antenna. With other parameters being fixed, the dual-band-notched frequency increases with decreasing R_1 and R_2. For fixed R_1 and R_2, the resonance frequency could be enhanced by increasing slit width of squares (g). For the convenience of optimization, the width of squares (d_1, d_2) and distance between squares are set to be the same as (g). Then, the distance (C_1, C_2) between these two CSRRs can also be optimized. These optimization works were managed by using commercial 3-D electromagnetic software HFSS [14].

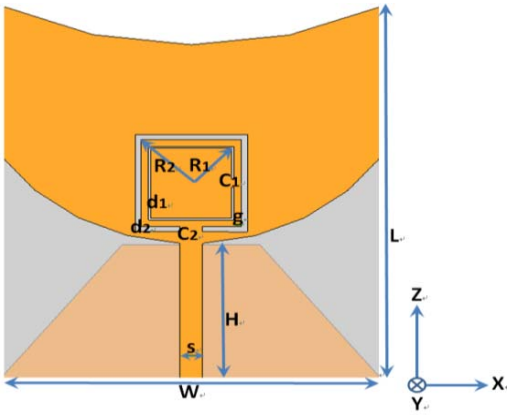

Fig. 1. Geometry of the antenna, with dimensions, R_1 = 3.75 mm, R_2 = 4.65 mm, C_1 = 0.6 mm, C_2 = 1.5 mm, S = 1.5 mm, H = 10.2 mm, W = 25 mm, L = 27.9 mm.

Figure 2 shows the current distributions at dual center notched bands. The dimensions of two 90 degrees rotation angle quadrilateral CSRR are corresponding to dual notched bands [15]. When the antenna is working at the center of lower notched band near 3.9 GHz, the outer CSRR functions as a separator in Fig. 2 (a), which is almost in dependent of the other band-notches. Similarly, from Fig. 2 (b), the upper notched band near 5.8 GHz is ensured by the inner CSRR [16].

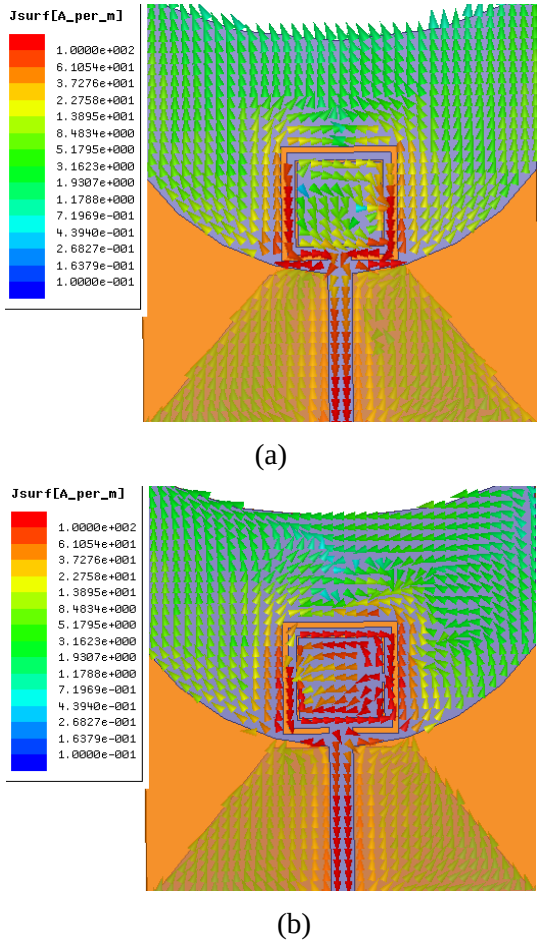

Fig. 2. The current distribution at (a) 3.9 GHz and (b) 5.8 GHz.

III. RESULTS AND DISCUSSION

The proposed novel 90 degrees rotation angle quadrilateral CSRR shows distinct double band gaps due to the weaker mutual coupling between inner and outer rings even though the two band gaps are adjacent [17]. Thus, 90 degrees rotation angle quadrilateral CSRR is selected to obtain adjacent dual notched bands for C-band (3.7 GHz–4.2 GHz) satellite communication systems and upper WLAN [18]. Figure 3 shows the photographs of the dual band-notch UWB antenna. It is noted that the inner opening ring and outer opening ring have just 90 degrees. Figure 4 shows the measured and simulated VSWRs versus frequency. The results show that the proposed antenna can offer sufficiently wide impedance bandwidth covering 2 GHz – 12 GHz or more with the dual notched bands. The measured dual notched bands include 3.65 GHz – 4.18 GHz and

5.7 GHz – 6.06 GHz, covering C-band satellite communication systems and upper WLAN, respectively. Therefore, by loading 90 degrees rotation angle quadrilateral CSRR with different centers, the CSRR can provide good dual band-notch performance. Owning to its dual band-notch structure, the CSRR can reduce the design space to achieve dual notched bands in comparison with the complementary edge-coupled SRR. The radiation characteristics of the frequencies across the band have also been studied [19]. Figures 5 and 6 show the simulated and measured 2-D radiation patterns, respectively at frequencies 3.5 GHz, 5 GHz, and 7.5 GHz for the proposed UWB antenna. Measurements of the radiation patterns of the prototype are carried out in an anechoic chamber. It can be seen that the radiation patterns in the xy-plane (H-plane) are almost omni-directional and the radiation patterns in the yz-plane (E-plane) are monopole alike. Clearly, the dual notch UWB antenna has an excellent radiation performance when it operates at 3.5 GHz, 5 GHz, and 7.5 GHz. By comparing with Figs. 5 and 6, the measured radiation patterns show slight deterioration in the co- and cross-polarization electric fields. To some extent, this is due to the measurement environment. Especially, the SMA feeding connector may have interference to radiation field in the test. Distortions in the E-plane patterns begin to occur at higher frequencies because the radiating elements are no longer small relative to those wavelengths. Figure 7 shows measured gains of the proposed antenna. It is observed that the antenna keeps a stable antenna gain about 3-4 dBi, which decreases significantly to about -10 dBi and -3 dBi at the dual notched bands. This demonstrates that the antenna has great dual band-notched characteristics.

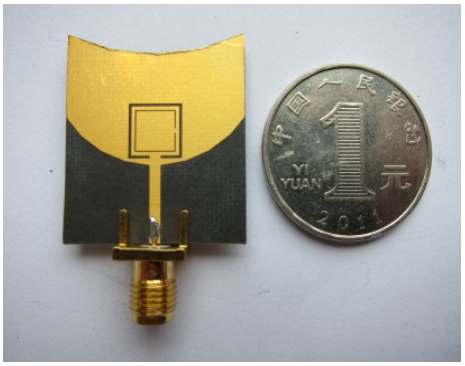

(a)

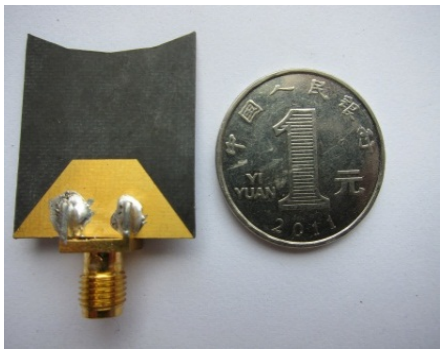

(b)

Fig. 3. Photographs of the proposed antenna; (a) front view and (b) bottom view.

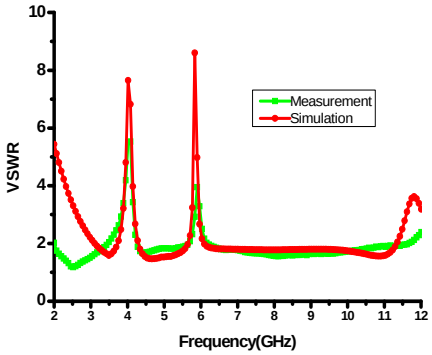

Fig. 4. Comparison between the simulated and measured VSWR of the proposed antenna.

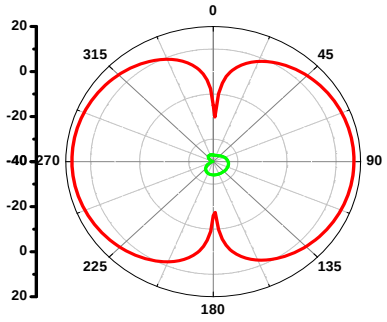

f = 3.5 GHz

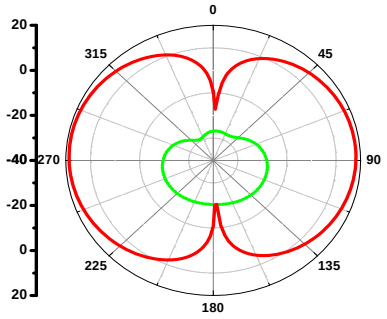

f = 5 GHz

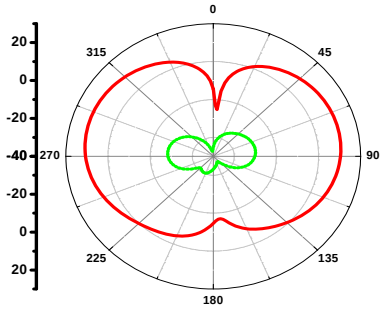

f = 7.5 GHz

(a)

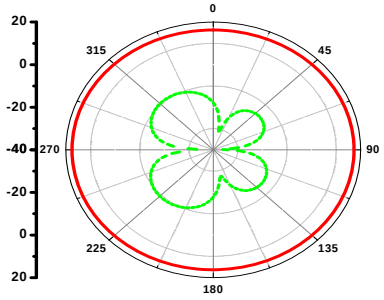

f = 3.5 GHz

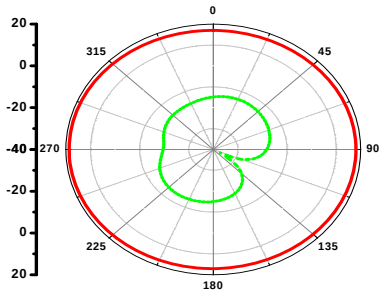

f = 5 GHz

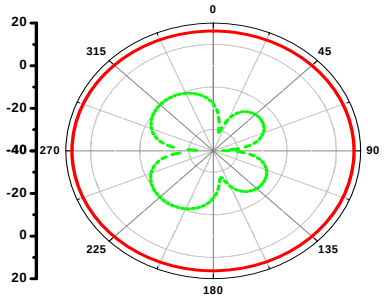

f = 7.5 GHz

(b)

Co-polar: Cross-polar:

Fig. 5. Simulated radiation patterns at (a) yz -plane and (b) xy-plane.

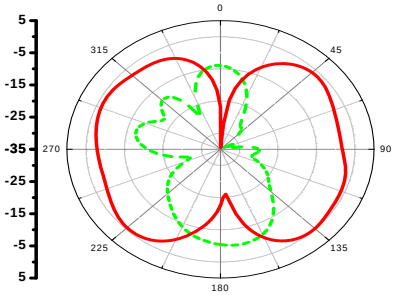

f = 3.5 GHz

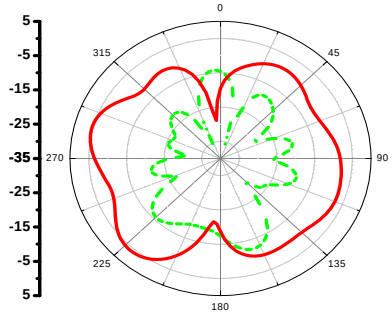

f = 5 GHz

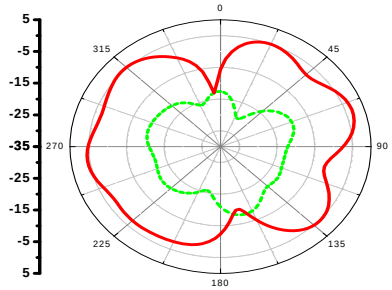

f = 7.5 GHz

(a)

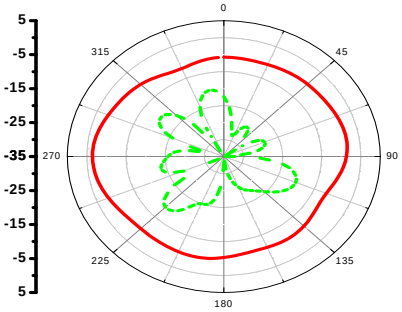

f = 3.5 GHz

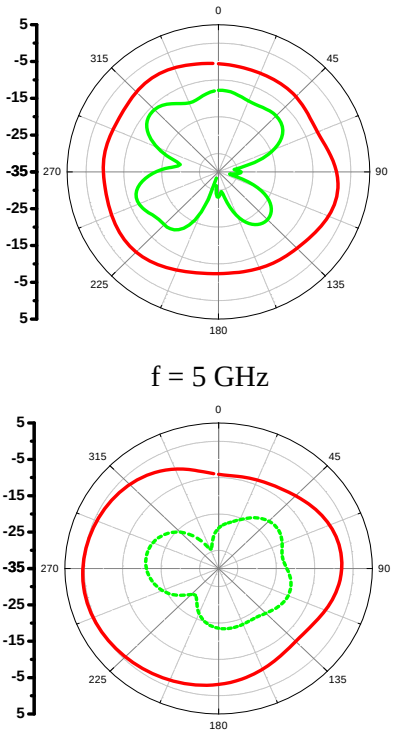

Fig. 6. Measured radiation patterns at (a) yz -plane and (b) xy-plane.

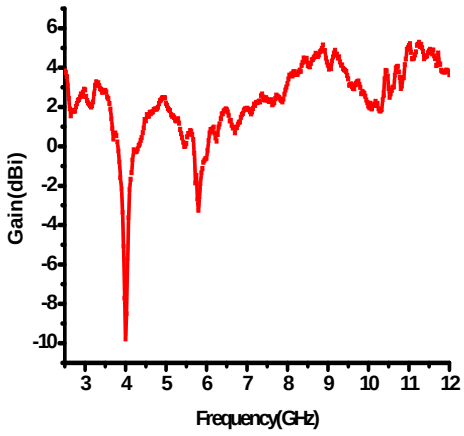

Fig. 7. Measured gain of the proposed antenna.

IV. CONCLUSION

A swallow shaped microstrip patch antenna with narrow loops leading to a small size multi-band planar monopole antenna has been presented. The swallow shaped patch antenna covers the UWB frequency range. By changing the length of the added resonant loops in the notched region, the center frequency of the multi resonances below the UWB frequency can be finely tuned. Furthermore, broad bandwidth and good monopole-like radiation patterns are obtained with a rather compact antenna size. Also, the prototype has been constructed and measured to show an excellent agreement with the simulated results. Therefore, the proposed antenna is extremely useful for short-range wireless communication systems.

ACKNOWLEDGMENT

This work is supported by the National Natural Science Foundation of China (Grant No.61106115 and 60971037) and the Fundamental Research Funds for the Central Universities (ZYGX2011J018).

REFERENCES

[1] Batra, "Multiband OFDM physical layer proposal for IEEE 802.15 task group 3a," *IEEE Document* 802.15-04-0493r1, 2003.

[2] R. Kohno, M. McLaughlin, and M. Welborn, "DS-UWB physical layer submission to 802.15 task group 3a," *IEEE Document* 802.15-04-0137r4, 2005.

[3] Z. N. Chen, T. S. P. See, and X. Qing, "Small printed ultra wideband antenna with reduced ground plane effect," *IEEE Trans. Antennas Propag.*, vol. 55, no. 2, pp. 383-388, Feb. 2007.

[4] G. Zhang, J. S. Hong, B. Z. Wang, and G. Song, "Switched band-notched UWB/WLAN monopole antenna," *Applied Computational Electromagnetics Society (ACES) Journal*, vol. 27, no. 3, pp. 256-260, March 2012.

[5] J. R. Verbiest and G. A. E. Vandenbosch, "A novel small-size printed tapered monopole antenna for UWBWBAN," *IEEE Antennas Wireless Propag. Lett.*, vol. 5, pp. 377-379, 2006.

[6] J. Wang, S. Qu, Z. Xu, H. Ma, Y. Yang, and C. Gu, "A controllable magnetic metamaterial: resonator with rotated inner ring split-ring," *IEEE Trans. Antennas Propag.*, vol. 56, no. 7, pp. 2018-2022, Feb. 2008.

[7] C.-C. Lin, P. Jin, and R. W. Ziolkowski, "Single, dual and tri-band-notched ultra-wide band(UWB) antennas using capacitively loaded loop (CLL) resonators," *IEEE Trans. Antennas Propag.*, vol. 60, no. 1, pp. 102-109, Feb. 2012.

[8] S. Radiom, H. Aliakbarian, G. A. E. Vandenbosch, and G. G. E. Gielen, "An effective technique for symmetric planar monopole antenna miniaturization," *IEEE Trans. Antennas Propag.*, vol. 57, no. 10, pp. 2989-2996, Oct. 2009.

[9] M. T. Partovi, N. Ojaroudi, and M. Ojaroudi, "Small slot antenna with enhanced bandwidth and band-notched performance for UWB applications," *Applied Computational Electromagnetics Society (ACES) Journal*, vol. 27, no. 9, pp. 772-778, Sep. 2012.

[10] D. Valderas, R. Alvarez, J. Melendez, I. Gurutzeaga, J. Legarda, and J. I. Sancho, "UWB staircase-profile printed monopole design," *IEEE Antennas Wireless Propag. Lett.*, vol. 7, pp. 255-259, 2008.

[11] M. Gopikrishna, D. D. Krishna, C. K. Anandan, P. Mohanan, and K. Vasudevan, "Design of a compact semi-elliptic monopole slot antenna for UWB systems," *IEEE Trans. Antennas Propag.*, vol. 57, no. 6, pp. 1834-1837, June 2009.

[12] A. M. Montaser, K. R. Mahmoud, and H. A. Elmikati, "Integration of an optimized E-shaped patch antenna into laptop structure for bluetooth and notched-UWB standards using optimization techniques," *Applied Computational Electromagnetics Society (ACES) Journal*, vol. 27, no. 10, pp. 786-794, October 2012.

[13] A. M. Abbosh and M. E. Bialkowski, "Design of ultra wideband planar monopole antennas of circular and elliptical shape," *IEEE Trans. Antennas Propag.*, vol. 56, no. 1, pp. 17-23, Jan. 2008.

[14] M. Ojaroudi, N. Ojaroudi, and Y. Ebazadeh, "Dual band-notch small square monopole antenna with enhanced bandwidth characteristics for UWB applications," *Applied Computational Electromagnetics Society (ACES) Journal*, vol. 27, no. 5, pp. 420-426, May 2012.

[15] A. Nouri and G. R. Dadashzadeh, "A compact UWB band-notched printed monopole antenna with defected ground structure," *IEEE Antennas and Wireless Propag. Lett.*, vol. 10, pp. 1178-1181, 2011.

[16] B. H. Siahkal-Mahalle, M. Ojaroudi, and N. Ojaroudi, "Enhanced bandwidth small square monopole antenna with band-notched functions for UWB wireless communications," *Applied Computational Electromagnetics Society (ACES) Journal*, vol. 27, no. 9, pp. 759-765, Sep. 2012.

[17] D. Jiang, Y. Xu, R. Xu, and W. Lin, "Compact dual-band-notched UWB planar monopole antenna with modified CSRR," *Electronics Letters*, vol. 48, no. 20, pp. 1250-1257 Sep. 2012.

[18] C.-M. Wu, Y.-L. Chen, and W.-C. Liu, "A compact ultra-wideband slotted patch antenna for wireless USB dongle application," *IEEE Antennas and Wireless Propag. Lett.*, vol. 11, pp. 596-599, 2012.

[19] F. Wei, Z. D. Wang, F. Yang, and X. W. Shi, "Compact UWB BPF with triple-notched bands based on stub loaded resonator," *Electronic Letters*, vol. 49, no. 2, Jan. 2013.

Di jiang received the B.Sc. degree in Communication Engineering from the Gui Lin University of Electronic Technology (GLIET), China, in 2004, and is currently pursuing the Ph.D. degree in Electromagnetic Field and Microwave Technology at the University of Electronic Science and Technology of China (UESTC), Chengdu, China. His research interest includes miniature antenna, RF circuit, and metamaterial design and its application.

Bo Yan received the B.Sc., M.Sc., and Ph.D. degrees in 1991, 1994, and 1998 in Electromagnetic Field and Microwave Technology from the University of Electronic Science and Technology of China (UESTC), respectively. He has been an Associate Professor in UESTC since 2000. His research interests include microwave and millimeter wave circuit designing.

Ruimin Xu received the Ph.D. degree in Electrical Engineering from the University of Electronic Science and Technology of China (UESTC), Chengdu, China. At present as a university of electronic science and technology extremely high frequency complex system, deputy director of the national defense key discipline laboratory. The main research fields including microwave millimeter-wave circuits and systems, microwave monolithic integrated circuit.

Bandwidth Enhancement of Small Square Monopole Antennas by Using Defected Structures Based on Time Domain Reflectometry Analysis for UWB Applications

Mohammad Ojaroudi and Esfandiar Mehrshahi

Faculty of Electrical and Computer Engineering,
Shahid Beheshti University, Tehran, Iran
m_ojaroudi@sbu.ac.ir and mehr@sbu.ac.ir

Abstract ─ In this paper a simple printed monopole antenna with enhanced bandwidth by using defected structures for UWB applications is presented, which is designed due to time domain designing method. The proposed antenna consists of a square radiating patch with a defected mircostrip feed-line by a pair of T-shaped slits and a defected ground plane by a pair of rectangular slots with a T-shaped strip protruded inside the slots, which provides a wide usable fractional bandwidth of more than 130 % (3.06 GHz - 14.27 GHz). By cutting two modified T-shaped slits with variable dimensions on the feed-line and also by inserting a pair of rectangular slots with T-shaped protruded strip inside the slots on the ground plane, additional resonances are excited and hence much wider impedance bandwidth can be produced. This large operating bandwidth is obtained by choosing suitable dimension for the proposed defected structures. To verify the validation of the proposed antenna, the equivalent circuit based on time domain reflectometry analysis is presented. Detailed simulation and numerical investigations are conducted to understand their behaviors and optimize for broadband operation. The designed antenna has a small size of 12 × 18 mm^2, about $0.15\lambda \times 0.25\lambda$ at 4.2 GHz. The proposed antenna exhibits almost omnidirectional radiation patterns with low cross polarization level.

Index Terms ─ Defected microstrip structure (DMS), defected ground structure (DGS), square monopole antenna, and time domain reflectometry (TDR).

I. INTRODUCTION

Commercial UWB systems require small low-cost antennas with omnidirectional radiation patterns and large bandwidth [1]. It is a well-known fact that planar monopole antennas present really appealing physical features, such as simple structure, small size, and low cost. Due to all these interesting characteristics, planar monopoles are extremely attractive to be used in emerging UWB applications, and growing research activity is being focused on them.

In UWB communication systems, one of the key issues is the design of a compact antenna while providing wideband characteristic over the whole operating band. Consequently, a number of planar monopoles with different geometries have been experimentally characterized [2-3] and automatic design methods have been developed to achieve the optimum planar shape [4-5]. Moreover, other strategies to improve the impedance bandwidth have been investigated [6-8].

In this paper, a simple method for designing a novel and compact microstrip-fed monopole antenna with multi resonance performance based on time domain refelectometry for UWB applications has been presented and discussed. In this paper, for the first time, based on defected microstrip structures (DMS) and defected ground structures (DGS), for bandwidth enhancement we use a pair of T-shaped slits in the microstrip feed-line and two rectangular slots with a T-shaped strip protruded inside the slots in the ground plane (unlike other UWB antennas reported in the literature to date [4-7], this structure has an

Submitted On: Jul. 13, 2012
Accepted On: Mar. 16, 2013

ordinary square radiating patch configuration). Furthermore, the circuit model of different parts of the antenna based on time domain reflectometry analysis is achieved and presented. The size of the designed antenna is smaller than the UWB antennas with band-notched function reported recently [2-8]. Good return loss and radiation pattern characteristics are obtained in the frequency band of interest. Simulated and measured results are presented to validate the usefulness of the proposed antenna structure for UWB applications.

II. ANTENNA DESIGN

The square monopole antenna fed by a 50 Ω microstrip line is shown in Fig. 1, which is printed on an FR4 substrate with the width of W_{sub} = 12 mm and the length of L_{sub} = 18 mm, thickness of 0.8 mm, permittivity of 4.4, and loss tangent of 0.018. The basic antenna structure consists of a square patch, a feed line, and a ground plane. The square patch has a width of W = 10 mm. The patch is connected to a feed line with the width of W_f = 1.5 mm and the length of L_f = 7 mm, as shown in Fig. 1. On the other side of the substrate, a conducting ground plane with the width of W_{sub} = 12 mm, and the length of L_{gnd} = 4 mm, is placed. The proposed antenna is connected to a 50 Ω SMA connector for signal transmission. In order to design a novel antenna, we proposed a new compact monopole antenna with a defected microstrip feed-line and defected ground structure. In this structure, by cutting the two T-shaped slit of suitable dimensions at the microstrip feed-line, it is found that much enhanced impedance bandwidth can be achieved for the proposed antenna. In addition, the defected microstrip structure is playing an important role in the broadband characteristics of this antenna, because it can adjust the electromagnetic coupling effects between the patch and the ground plane, and improves its impedance bandwidth without any cost of size or expense. This phenomenon occurs because, with the use of a defected structure in transmission line distance, additional coupling is introduced between the bottom edge of the square patch and the ground plane [9].

Regarding defected ground structures (DGS), creating slots in the ground plane provide an additional current path. Moreover, this structure changes the inductance and capacitance of the input impedance, which in turn leads to a change in the bandwidth. The DGS applied to a microstrip line causes a resonant character of the structure transmission with a resonant frequency controllable by changing the shape and size of the slot [10]. Therefore, by cutting two T-shaped slots at the ground plane and carefully adjusting its parameters, much enhanced impedance bandwidth may be achieved.

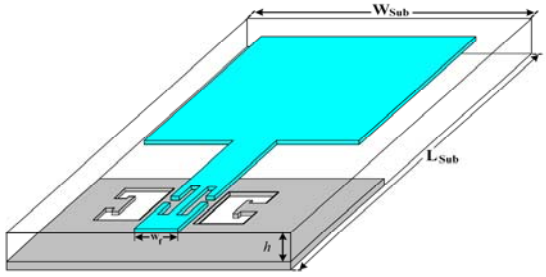

(a)

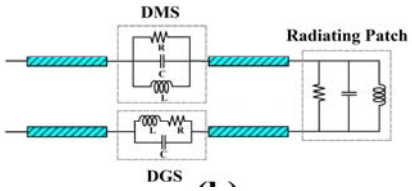

(b)

Fig. 1. (a) Geometry of the proposed square monopole antenna with defected structures and (b) the proposed antenna equivalent circuit.

III. DEFECTED TRANSMISSION LINE

A. Defected structures (DGS and DMS) and its equivalent circuit models

Recently, the defected ground plane structures (DGS) and defected microstrip structure (DMS) have been proposed for suppression of spurious response in the microstrip structures [11-12]. These configurations provide band-stop characteristics. The proposed DMS and DGS with their equivalent circuit models are shown in Figs. 2 and 3, respectively, which is printed on an FR4 substrate of thickness 0.8 mm, permittivity 4.4, and loss tangent 0.018. The corresponding geometrical parameters of the proposed structures are denoted in Figs. 2 (a) and 3 (a). In this study, the defected structure on the ground plane and

feed-line will perturb the incident and return current and induce a voltage difference on the ground plane and microstrip feed-line. These two effects can be modeled as a parallel LC circuit [13]. The resistance in equivalent circuits represents the loss of the slot and slit, which is small in general. In the proposed DMS equivalent circuits, R is the series resistance due to conductor losses and dissipation arising from current flowing in the silicon substrate, also in the proposed DGS equivalent circuits, R is the parallel resistance due to substrate dissipation. The shunt parasitic results from a combination of capacitances are due to the gap distance between defected structures edges and underlying substrate. If there are multiple conducting edges, then there should be one C corresponding to each gap distance.

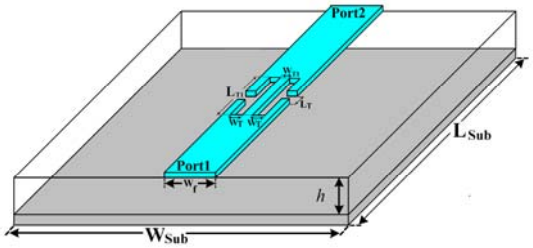

(a)

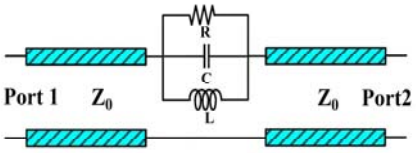

(b)

Fig. 2. (a) Geometry of the proposed DMS, with W_T = 0.3 mm, W_{T1} = 0.4 mm, L_T = 0.4 mm, and L_{T1} = 3 mm and (b) equivalent circuit model.

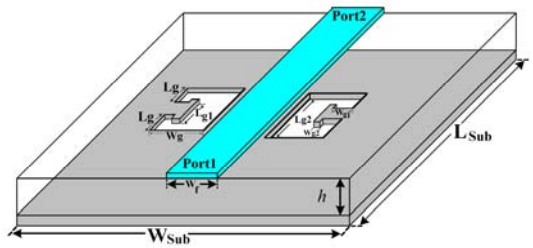

(a)

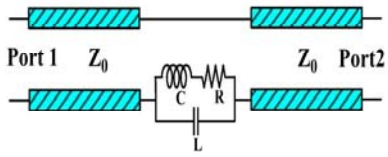

(b)

Fig. 3. (a) Geometry of the proposed DGS, with W_g = 3 mm, W_{g1} = 1 mm, W_{g2} = 1 mm, L_g = 2.6 mm, L_g = 1 mm, and L_{g2} = 2 mm and (b) equivalent circuit model.

In this work, the final step in the design is to choose the length of the DGS and DMS resonators. A good starting point is to choose it to be equal to $\lambda_m/4$, where λ_m is the guided wavelength in the microstrip line. In this design, the optimized length $L_{resonance}$ is set to resonate at 0.25 $\lambda_{resonance}$, where $L_{resonance\ DGS} = W_g + W_{g1} + W_{g2} + 0.5\ L_{g2} + L_g$ and $L_{resonance\ DMS} = 0.5\ W_{T1} + W_T + L_{T1} + 0.5\ (L_{T1} - L_T)$. $\lambda_{resonance\ DGS}$ and $\lambda_{resonance\ DMS}$ correspond to the DGS resonance frequency (12 GHz) and the DMS resonance frequency (13.9 GHz), respectively. Simulated insertion and return loss characteristics for the proposed DMS and DGS shown in Figs. 2 (a) and 3 (a), with their resonances frequencies are shown in Fig. 4.

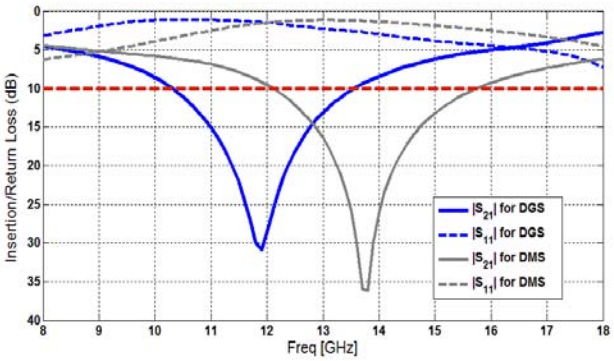

Fig. 4. Simulated insertion and return loss characteristics for the proposed DMS and DGS shown in Figures 2 (a) and 3 (a).

B. Time domain reflectometry analysis

In this section, the proposed defected structures with mentioned design parameters were simulated, and then the TDR results of their input impedance are presented and discussed, in both equivalent circuit and full-wave analysis cases.

The simulated full-wave TDR results are obtained using the Ansoft simulation software high-frequency structure simulator (HFSS) [15].

In order to calculate the TDR results for the proposed equivalent circuits, the impedance of these circuits in Laplace domain can be represented as in equations (1) and (2),

$$Z_{DGS} = \frac{Ls + R}{LCs^2 + RCs + 1} \quad (1)$$

$$Z_{DMS} = \frac{RLs}{RLCs^2 + Ls + R}. \quad (2)$$

Assuming that the characteristic impedance of the microstrip line is Z_0, we can write the reflection coefficient through a defected structure as in equation (3), which is observed at the source end, i.e., port 1,

$$\Gamma_Z(s) = \frac{Z(s)}{Z(s) + 2Z_0}. \quad (3)$$

Therefore, the reflected waveform for the proposed DGS and DMs can be written as,

$$\Gamma_{DGS}(s) = \frac{Ls + R}{2Z_0LCs^2 + (2Z_0RC + L)s + R + 2Z_0} \quad (4)$$

$$\Gamma_{DMS}(s) = \frac{RLs}{2Z_0RLCs^2 + (2Z_0C + RL)s + 2Z_0R}. \quad (5)$$

A step voltage source with rise time τ_r and amplitude V_0, can be expressed as in [13],

$$V_{in}(s) = \frac{V_0}{2\tau_r}\frac{1}{s^2}\left(1 - e^{-\tau_r S}\right). \quad (6)$$

Therefore, the reflected waveform in Laplace domain can be written as,

$$V_{TDR}(s) = V_{in}(s).\Gamma_{DGS,DMS}(s). \quad (7)$$

In TDR measurements, the impedance follows as,

$$Z_{TDR} = Z_0 \times \left(V_{in}(t) + V_{TDR}(t)\right)/\left(V_{in}(t) - V_{TDR}(t)\right). \quad (8)$$

In which Z_0 is the characteristic impedance of the transmission line at the terminal.

Figures 4 and 5 show the simulated reflection waveform observed at port 1 of the defected structures, as shown in Figs. 2 and 3, and with a 50 termination on port 2. The excitation source is a step wave with amplitude of 1 V and rise time of 15 psec. The corresponding result predicted by the equivalent circuit model is also shown in these figures and good agreement is seen. As shown in Figs. 5 and 6, TDR curves have started from t = 0.4 nsec, with an impedance just under 50 Ω. This is indeed the characteristic impedance of the microstrip line. At impedance discontinuities, part of the input signal is reflected. These reflections, after traveling back, reach terminal port1 and are observed there [13]. From these observations, the characteristic impedances along the transmission line can be computed. The optimal dimensions of the equivalent circuit models parameters are specified in Table 1.

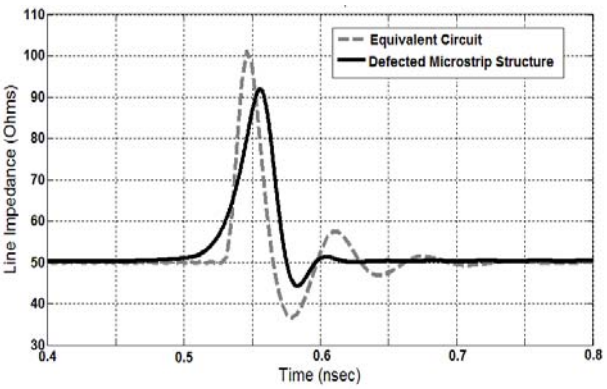

Fig. 5. The reflected waveforms simulated by HFSS and predicted by equivalent circuit model of the proposed defected microstrip structure shown in Fig. 2.

Table 1: Equivalent circuit model parameters.

Element	DMS	DGS
L	4.8 (nH)	0.75 (nH)
C	2.05 (pF)	15.75 (pF)
R	2.5 (Ω)	1.35 (Ω)

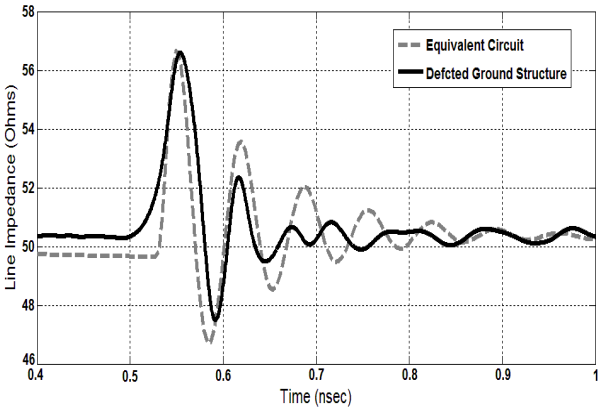

Fig. 6. The reflected waveforms simulated by HFSS and predicted by equivalent circuit model of the proposed defected ground structure shown in Fig. 3.

IV. RESULTS AND DISCUSSION

The planar monopole antenna with various design parameters were constructed, and the numerical and experimental results of the input impedance and radiation characteristics are presented and discussed. The parameters of this proposed antenna are studied by changing one parameter at a time while others are kept fixed. Figure 7 shows the structure of various antennas used for simulation studies. Return loss characteristics for ordinary square patch antenna (Fig. 7 (a)), with two modified T-shaped slits with variable dimensions on the feed-line (Fig.7 (b)), and with two modified T-shaped slits with variable dimensions on the feed-line and a pair of rectangular slots with T-shaped protruded strip inside the slots on the ground plane (Fig. 7 (c)) are compared in Fig. 8. As shown in Fig. 8, it is observed that by using this modified element including two modified T-shaped slits with variable dimensions on the feed-line and a pair of rectangular slots with T-shaped protruded strip inside the slots on the ground plane, additional third and fourth resonances are excited, respectively, and hence the bandwidth is increased**.**

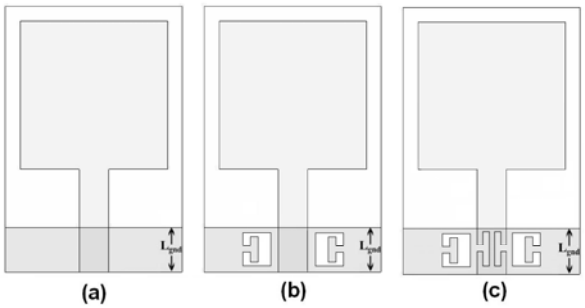

Fig. 7. (a) The ordinary square monopole antenna, (b) the square antenna with defected ground structure, and (c) the proposed antenna.

As shown in Fig. 8, in the proposed antenna configuration, the ordinary square monopole can provide the fundamental and next higher resonant radiation band at 4.2 GHz and 8.1 GHz, respectively, in the absence of these defected structures. The upper frequency is affected by using the rectangular slots with T-shaped protruded strip inside the slots on the ground plane. This behavior is mainly due to the change of surface current path by the dimensions of T-shaped slits at third resonance frequency (12.05 GHz), as shown in Fig. 9 (a). In addition, by inserting two modified T-shaped slits with variable dimensions on the feed-line the impedance bandwidth is effectively improved at the upper frequency [13]. As shown in Fig. 9 (b), the current concentrated on the interior and exterior edges of the two modified T-shaped slits at fourth resonance frequency (13.91 GHz). Therefore, the antenna impedance changes at this frequency, due to the resonant properties of the T-shaped slits. It is found that by using these slits, the fourth resonance occurs at 13.91 GHz in the simulation. Also input impedance of the various monopole antenna structures that shown in Fig. 7, on a Smith chart is shown in Fig. 10.

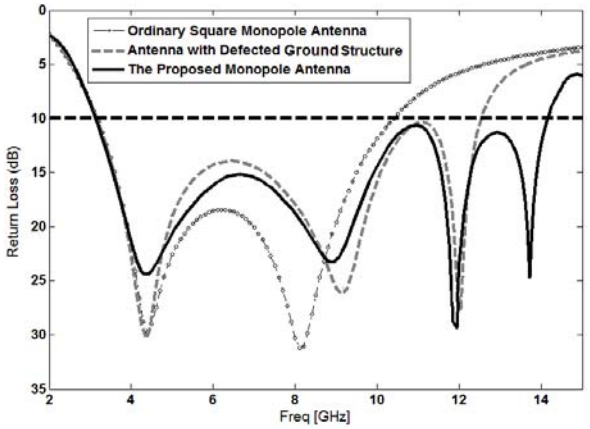

Fig. 8. Simulated return loss characteristics for the antennas shown in Fig. 6.

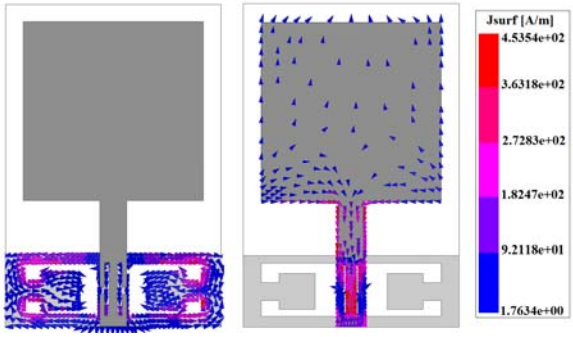

Fig. 9. Simulated surface current distributions plane for the proposed monopole antenna (a) on the ground at the third resonance frequency (12.05 GHz) and (b) on the radiating patch at the fourth resonance frequency (13.91 GHz).

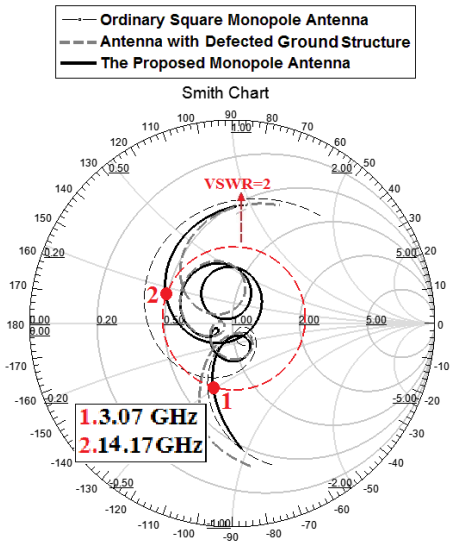

Fig. 10. The simulated input impedance on a Smith chart of the various antenna structures shown in Fig. 6.

The proposed antenna with optimal design, as shown in Fig. 11, was built and tested. Figure 12 shows the measured and simulated return loss characteristics of the proposed antenna. The fabricated antenna has the frequency band of 3.06 GHz to over 14.27 GHz. As shown in Fig. 12, there exists a discrepancy between the measured data and the simulated results. This discrepancy is mostly due to a number of parameters such as the fabricated antenna dimensions as well as the thickness and dielectric constant of the substrate on which the antenna is fabricated and the wide range of simulation frequencies. In order to confirm the accuracy of return loss characteristics for the designed antenna, it is recommended that the manufacturing and measurement processes need to be performed carefully, besides, SMA soldering accuracy, and the FR4 substrate quality needs to be taken into consideration.

Figures 13 and 14 show the measured radiation patterns at resonance frequencies including the co-polarization and cross-polarization in the *H*-plane (*x*-*z* plane) and *E*-plane (*y*-*z* plane). The main purpose of presenting the radiation patterns is to demonstrate that the antenna actually radiates over a wide frequency band. It can be seen that the radiation patterns in *x*-*z* plane are nearly omnidirectional even at higher frequencies, and also the cross-polarization level is low for the four frequencies.

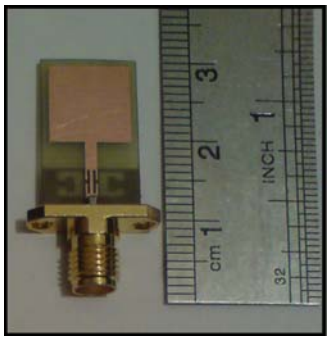

Fig. 11. Photograph of the realized printed square monopole antenna.

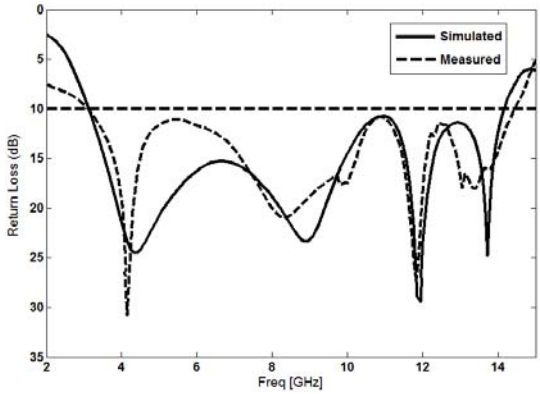

Fig. 12. Measured and simulated return loss for the proposed antenna.

V. CONCLUSION

In this paper, a novel compact printed monopole antenna with multi resonance characteristics with a novel time domain method to extract the RLC equivalent circuits of the defected structures has been proposed for UWB applications. The analytic formulations for the equivalent circuit models are obtained based on time-domain reflectometry theory, Laplace transform. The fabricated antenna covers the frequency range of UWB systems between 3.06 GHz to 14.27 GHz. The proposed antenna has a simple configuration and is easy to fabricate. Experimental results show that the proposed antenna could be a good candidate for UWB application.

ACKNOWLEDGMENT

The authors are thankful to Microwave Technology (MWT) Company staff for their beneficial and professional help (www.microwave-technology.com).

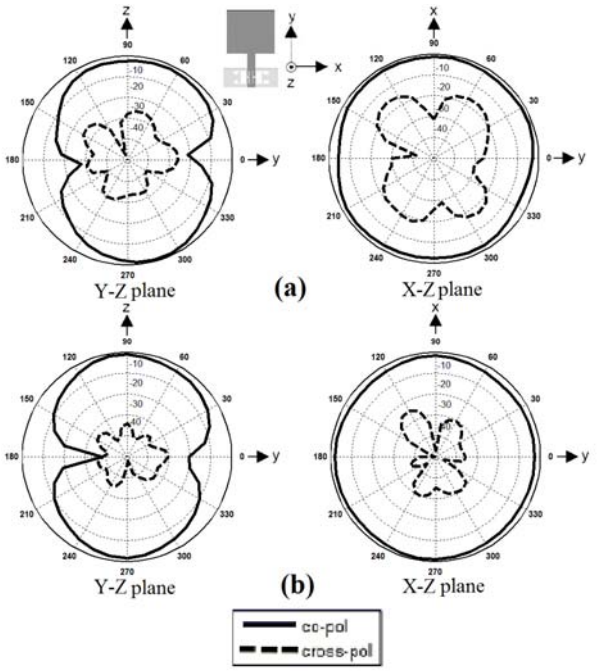

Fig 13. Measured radiation patterns of the proposed antenna; (a) first resonance frequency (4.13 GHz) and (b) second resonance frequency (9.35 GHz).

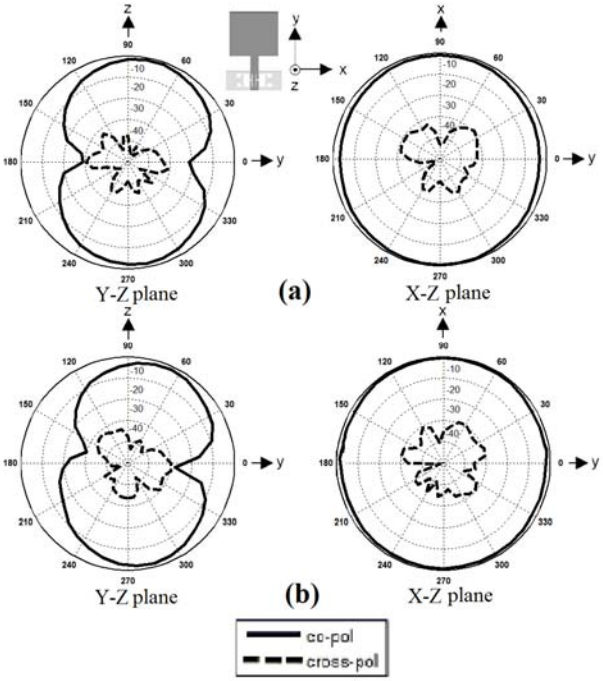

Fig 14. Measured radiation patterns of the proposed antenna; (a) third resonance frequency (12.05 GHz) and (b) fourth resonance frequency (13.91 GHz).

REFERENCES

[1] H. Schantz, *The Art and Science of Ultra Wideband Antennas*, Artech House 2005.

[2] M. J. Ammann, "Impedance bandwidth of the square planar monopole, " *Microwave and Optical Tech. Letters*, vol. 24, no. 3, Feb. 2000.

[3] J. A. Evans and M. J. Ammann, "Planar trapezoidal and pentagonal monopoles with impedance bandwidths in excess of 10:1, " *IEEE Antennas and Propagation Society International Symposium*, vol. 3, pp. 1558-1561, July 1999.

[4] R. Azim, M. T. Islam, and N. Misran, "Design of a planar UWB antenna with new band enhancement technique," *Appl. Comp. Electro. Society (ACES) Journal*, vol. 26, no. 10, pp. 856-862, Oct. 2011.

[5] B. H. Siahkal-Mahalle, M. Ojaroudi, and N. Ojaroudi, "Enhanced bandwidth small square monopole antenna with band-notched functions for UWB wireless communications," *Appl. Comp. Electro. Society (ACES) Journal*, vol. 27, no. 9, pp. 759-765, Sep. 2012.

[6] M. T. Partovi, N. Ojaroudi, and M. Ojaroudi, "Small slot antenna with enhanced bandwidth and band-notched performance for UWB applications," *Appl. Comp. Electro. Society (ACES) Journal*, vol. 27, no. 9, pp. 772-778, Sep. 2012.

[7] N. Ojaroudi, M. Ojaroudi, and Sh. Amiri, "Enhanced bandwidth of small square monopole antenna by using inverted U-shaped slot and conductor-backed plane," *Appl. Comp. Electro. Society (ACES) Journal*, vol. 27, no. 8, pp. 685-690, August 2012.

[8] Z. Chen, X. Wu, H. Li, N. Yang, and M. Y. W. Chia, "Considerations for source pulses and antennas in UWB radio systems," *IEEE Trans. Antennas Propag.*, vol. 52, no. 7, pp. 1739-1748, July 2004.

[9] G. Zhang, J. S. Hong, B. Z. Wang, and G. Song, "Switched band-notched UWB/ WLAN monopole antenna," *Appl. Comp. Electro. Society (ACES) Journal*, vol. 27, no. 3, pp. 256-260, March 2012.

[10] W. C. Weng, "Optimal design of an ultra-wideband antenna with the irregular shape on radiator using particle swarm optimization," *Appl. Comp. Electro. Society (ACES) Journal*, vol. 27, no. 5, pp. 427-434, May 2012.

[11] A. B. Abdel-Rahman, A. K. Verma, A. Boutejdar, and A. S. Omar, "Control of bandstop response of Hi-Lo microstrip low-pass filter using slot in ground plane," *IEEE Trans. Microw. Theory Tech.*, vol. 52, no. 3, pp. 1008-1013, March 2004.

[12] A. Boutejdar, A. Elsherbini, H. Liu, and A. S. Omar, "Improvement of microstrip lowpass filters characteristics using an optimized number of new multi-ring defected ground structures," *Microwave*

and Optical Tech. Letters, vol. 49, pp. 3074-3078, 2007.

[13] C. H. Cheng, C. H. Tsai, and T. L. Wu, "A novel time domain method to extract equivalent circuit model of patterned ground structures," *IEEE Microw. Wireless Compon. Lett.*, vol. 17, no. 11, Nov. 2010.

[14] X. Zeng, J. He, M. Wang, and M. Abdulla, "New closed-form formula for series inductance and shunt capacitance based on measured TDR impedance profile," *IEEE Microw. Wireless Compon. Lett.*, vol. 17, no. 11, Nov. 2007.

[15] Ansoft High Frequency Structure Simulation (HFSS), Ver. 13, Ansoft Corporation, 2011.

[16] Z. Chen, X. Wu, H. Li, N. Yang, and M. Y. W. Chia, "Considerations for source pulses and antennas in UWB radio systems," *IEEE Trans. Antennas Propag.*, vol. 52, no. 7, pp. 1739-1748, July 2004.

Mohammad Ojaroudi was born on 1984 in Germi, Iran. He received his B.Sc. degree in Electrical Engineering from Azad University, Ardabil Branch and M.Sc. degree in Telecommunication Engineering from Urmia University. From 2010, he is working toward the Ph.D. degree at Shahid Beheshti University. From 2007 until now, he is a Teaching Assistant with the Department of Electrical Engineering, Islamic Azad University, Ardabil Branch, Iran.

Since March 2009, he has been a Research Fellow (Chief Executive Officer) in the Microwave Technology Company (MWT), Tehran, Iran. From 2012, Mr. Ojaroudi is a member of the IEEE Transaction on Antennas and Propagation (APS) reviewer group and the Applied Computational Electromagnetic Society (ACES). From 2013 he is a student member of the IEEE. His research interests include analysis and design of microstrip antennas, design and modeling of microwave structures, radar systems, and electromagnetic theory. He is author and coauthor of more than 100 journal and international conferences papers. His papers have more than 350 citations with 10 h-index.

Esfandiar Mehrshahi was born in Tehran, Iran, in 1964. He received the B.Sc. degree from the Iran University of Science and Technology, Tehran, Iran, in 1987, and the M.Sc. and Ph.D. degrees from the Sharif University of Technology, Tehran, Iran, in 1991 and 1998, respectively. Since 1990, he has been involved in several research and engineering projects at the Iran Telecommunications Research Center (ITRC). He is currently an Associate Professor at Shahid Beheshti University, Tehran, Iran. His main areas of interest are the nonlinear simulation of microwave circuits and microwave oscillator's spectrum.

Novel Varactor-Tuned Balanced Bandpass Filter with Continuously High Common-Mode Suppression

Qing-Yuan Lu, Jian-Xin Chen, Li-Heng Zhou, and Hui Tang

School of Electronics and Information
Nantong University, Nantong, 226019, China
jjxchen@hotmail.com

Abstract ─ In this letter, a novel balanced varactor-tuned bandpass filter (BPF) designed by using the half-wavelength microstrip resonators is proposed. The frequency-tuning mechanism of the resonator is analytically investigated for designing the proposed balanced BPF. By adding a tunable capacitor to the center of the resonator, it is noted that the common mode can be suppressed to a great extent in the frequency-tuning range of the differential-mode passband. Also, it has no effect on the differential-mode response. For demonstration, a balanced BPF is designed and fabricated. The simulated and measured results with good agreement show that the center frequency of the differential-mode passband can be tuned from 0.725 GHz to 0.811 GHz, while the common-mode suppression in this frequency range is always more than 25 dB.

Index Terms – Balanced bandpass filter (BPF), common-mode suppression, half-wavelength resonator, and tunable filter.

I. INTRODUCTION

Balanced technologies are becoming more and more attractive in the designs of RF/microwave circuits and systems because of their many advantages such as superior response performance, noise immunity and harmonic suppression. Many reports presented the effort [1-6], which was paid to achieve the desired bandpass response in differential operation and to decrease the level of common-mode noise in balanced bandpass filters (BPFs). Some of the common-mode suppression methods such as coupled-line and multi-section resonators, double-sided parallel-strip line (DSPSL), and coupled stepped-impedance resonators were reported in [1-6]. However, all of the designed filters were not tunable.

Tunable resonators and BPFs are in great demand by the current and emerging reconfigurable communication systems. The half-wavelength ($\lambda_g/2$) resonator has been widely studied for designing tunable circuits [7, 8]. Since the differential-mode frequency response of the $\lambda_g/2$ resonator corresponds to the fundamental resonance, it is highly suitable for applications in balanced tunable BPF [7]. In this case, the conventional methods can be utilized for analyzing the differential- and common-mode responses.

In this paper, the tunable $\lambda_g/2$ resonator is investigated for designing a balanced BPF. By adding a few tunable capacitors to the ends and center of the $\lambda_g/2$ resonator, the proposed BPF can be made not only tunable in its differential-mode passbands, but it has also attained high common-mode suppression in the frequency range of its differential-mode passbands. Simulated and measured results show that the center frequency of the differential-mode passband can be tuned from 0.725 GHz to 0.811 GHz, and the common-mode suppression in this frequency range is always greater than 25 dB. The input 1 dB compression point ($P_{in\text{-}1dB}$) and the input third-order intercept point (IIP_3) of the balanced tunable BPF are found to be 16 dBm and 26 dBm, respectively.

II. BALANCED TUNABLE BANDPASS FILTER

Figure 1 shows the configuration of the proposed balanced tunable BPF. It is composed of a pair of coupled tunable $\lambda_g/2$ resonator with loaded tunable admittances, as shown in Fig. 2 (a),

Submitted On: Dec. 26, 2012
Accepted On: Apr. 13, 2013

which are realized by a combination of a varactor D_i and a DC block capacitor C_i in series (where i = 1 or 2). As compared with the design in [7], the topology of the proposed BPF has a much simpler configuration, especially in the feeding scheme at the two differential ports. To simplify the analysis, the employed varactor D_i can be represented by a tunable capacitor C_{ti} and a resistance r_i in series. As a result, the loaded admittances at the center and the two ends of the $\lambda_g/2$ resonator can be obtained using,

$$Y_i = \frac{j\omega C_{ti}}{jr_i\omega C_{ti} + 1}. \quad (1)$$

In this design, the end-loaded Y_1 is used to tune the differential-mode resonant frequency f_0^d of the resonator for designing the tunable differential-mode passband of the proposed BPF. The central-loaded Y_2 is used to change the common-mode frequency response, and to ensure that the common-mode suppression in the differential passband is continuously high.

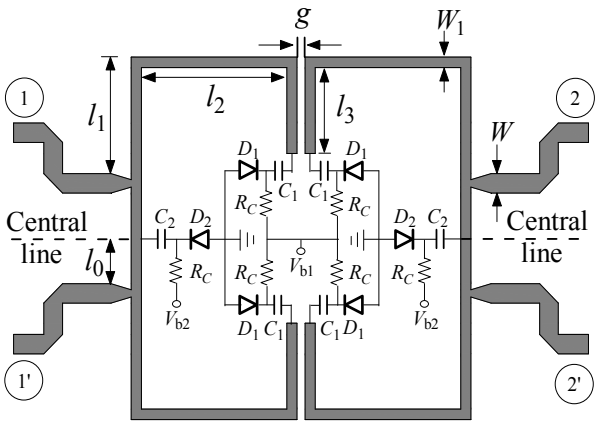

Fig. 1. Configuration of the proposed balanced varactor-tuned BPF using $\lambda_g/2$ resonators.

A. Different-mode analysis

Figure 2 (b) shows the differential-mode equivalent circuit of the tunable $\lambda_g/2$ resonator, where the central line in Fig. 1 is replaced by a short-circuited plane [8]. The central-loaded Y_2 has no effect on the differential-mode response. The differential-mode input admittance Y_{in}^d can be expressed as,

$$Y_{in}^d = -j\frac{Y_c}{\tan\theta} + Y_1 \quad (2)$$

where Y_c is the characteristic admittance, and θ is the electrical length of the transmission line. The resonant condition is that the imaginary part of Y_{in}^d is equal to 0, namely, $\mathrm{Im}\{Y_{in}^d\} = 0$, the expression of f_0^d can then be obtained as

$$f_0^d = \frac{Y_c}{2\pi C_{t1}(\tan\theta - jr_1 Y_c)}. \quad (3)$$

In this case, it is reasonable to assume $r_1 = 0$, and then it is obvious that f_0^d shifts down as C_{t1} is increased.

B. Common-mode analysis

Figure 2 (c) shows the common-mode equivalent circuit of the tunable $\lambda_g/2$ resonator, and the common-mode input admittance Y_{in}^c can be expressed as,

$$Y_{in}^c = Y_1 + Y_c\frac{Y_2/2 + jY_c\tan\theta}{Y_c + jY_2\tan\theta/2}. \quad (4)$$

Substituting equation (1) into equation (4) while assuming $r_1 = 0$,

$$\begin{aligned} Y_{in}^c = {} & j\omega C_{t1} + \frac{Y_c}{m}\times\{2Y_c r_2\omega^2 C_{t2}^2(1+\tan^2\theta) \\ & + j[2Y_c\omega C_{t2}(1-\tan^2\theta) \\ & + (4Y_c^2 r_2^2\omega^2 C_{t2}^2 + 4Y_c^2 - \omega^2 C_{t2}^2)\tan\theta]\} \end{aligned}, \quad (5a)$$

$$m = (2Y_2 - \omega C_{t2}\tan\theta)^2 + (2Y_2 r_2\omega C_{t2})^2. \quad (5b)$$

The common-mode unloaded quality factor Q_u^c can be obtained by

$$Q_u^c = \left|\frac{1}{r_2}\left(\frac{\cos(2\theta)}{\omega C_{t2}} + \frac{m\omega C_{t1} + 4Y_c^3\tan\theta}{2Y_c^2(1+\tan^2\theta)\omega^2 C_{t2}^2} - \frac{\sin(2\theta)}{4Y_c}\right) + Y_c r_2\sin(2\theta)\right|. \quad (6)$$

From equations (3) and (6), as C_{t1} is increased, f_0^d decreases; while Q_u^c increases when C_{t2} is fixed. Therefore, in the design of balanced tunable BPF, it is predictable that the suppression of dynamical common-mode can become a problematic issue when differential-mode passband is frequency agile. To solve this problem, C_{t2} should be made variable to maintain Q_u^c at a low value so that the common-mode can be always highly suppressed in the tunable differential-mode passband. For demonstration, the BPF is designed on an FR4 substrate with ε_r = 4.6 and h = 1.0 mm, and the two varactors are 1SV277 (D_1) and 1SV232 (D_2) from Toshiba, Tokyo, Japan with two

capacitors: C_1 = 1.5 pF and C_2 = 20 pF. The dimensions of the filter are: w_1 = 0.7 mm, l_0 = 4.33 mm, l_1 = 11.13 mm, l_2 = 15 mm, l_3 = 8.5 mm, g = 0.4 mm, and w = 1.84 mm is the width of the 50 Ω microstrip line.

As can be seen from the simulated results in Fig. 3, the utilization of Y_2 can decrease the Q_u^c value of the resonator, and the common-mode suppression of the balanced BPF in Fig. 1 is enhanced significantly (about 10 dB). However, as V_{b1} is decreased, i.e., C_{t1} is increased, the differential-mode passband shifts down, and the common-mode suppression gradually deteriorates when V_{b2} is fixed (C_{t2} is fixed). In the process of decreasing V_{b1} from 9 V to 0 V, the high common-mode suppression can be maintained by decreasing V_{b2} from 7 V to 4.2 V, as shown in Fig. 3.

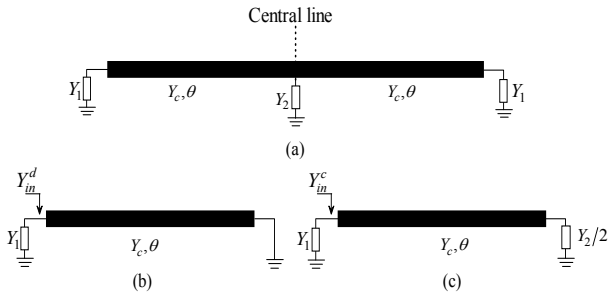

Fig. 2. (a) Equivalent model of the $\lambda_g/2$ resonator with loaded Y_1 and Y_2, (b) differential-mode equivalent circuit, and (c) common-mode equivalent circuit.

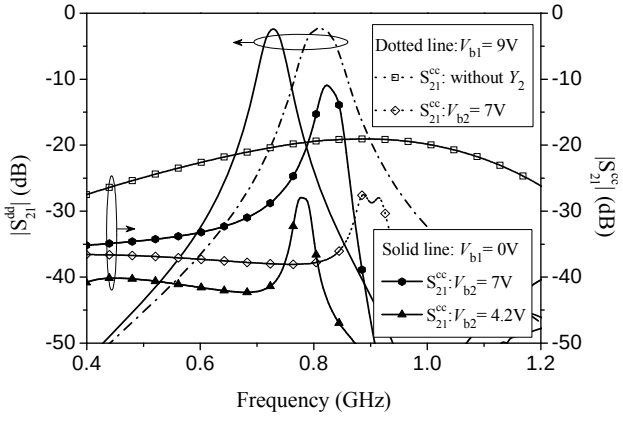

Fig. 3. The simulated results of the BPF shown in Fig. 1.

III. SIMULATED AND MEASURED RESULTS

Figure 4 shows the photo of the fabricated balanced tunable BPF, while Figs. 5 and 6 show the simulated and measured differential- and common-mode frequency responses of the balanced tunable BPF. The simulation and measurement resukts are accomplished using ADS software and network analyzer N5230C (both from Agilent). The analyzer is able to measure the two-port differential- and common-mode S-parameters directly. The center frequency of the differential passband shifts down from 0.811 GHz to 0.725 GHz as V_{b1} is decreased from 9 V to 0 V, and the insertion loss of the passband is always less than 3 dB in the entire frequency-tuning range. Meanwhile, the common-mode suppression in the differential passband can be kept greater than 25 dB by tuning V_{b2}. When V_{b1} = 6 V and V_{b2} = 5.4 V, the measured $P_{in\text{-}1dB}$ and IIP_3 are 16 dBm and 26 dBm, respectively, as shown in Fig. 7. As compared with the single-ended tunable BPFs in [9-12], the nonlinear performance of the proposed balanced tunable BPF is found to be more attractive and desirable, as shown in Table 1.

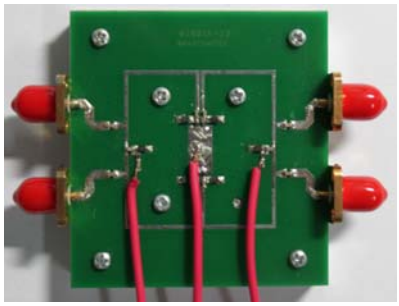

Fig. 4. Photo of the fabricated tunable balanced BPF.

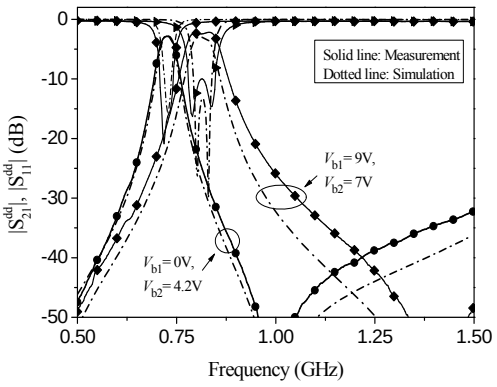

Fig. 5. Measured and simulated differential-mode responses.

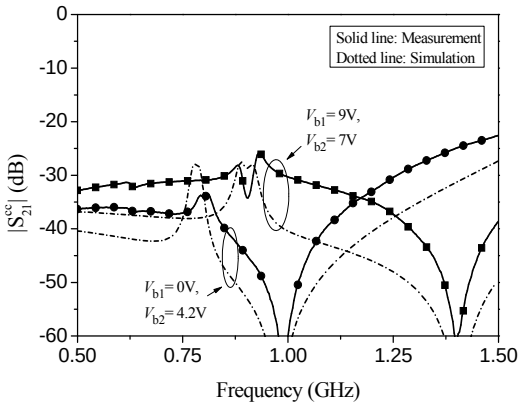

Fig. 6. Measured and simulated common-mode responses.

Table 1: Performance comparison with single-ended tunable BPFs.

Performance	$P_{in\text{-}1dB}$	IIP_3
Ref [9]	NA	10.4 dBm
Ref [10]	9 dBm	14dBm
Ref [11]	NA	15 dBm
Ref [12]	NA	19 dBm
This work	16 dBm	26 dBm

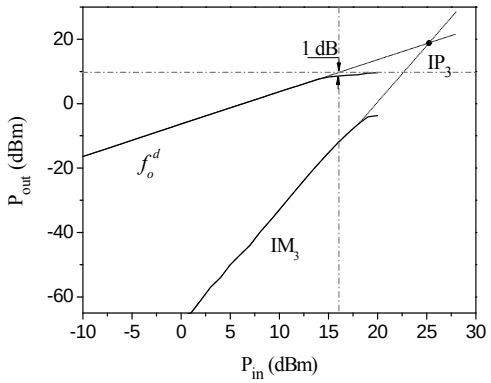

Fig. 7. Measured $P_{in\text{-}1dB}$ and two-tone IIP_3 with 1 MHz frequency spacing.

VI. CONCLUSION

A low-profile balanced tunable BPF using $\lambda_g/2$ resonator has been presented in this letter. The frequency tuning mechanism of this resonator has been studied and it has been used to design a balanced tunable BPF. Interestingly, it has been found that the common-mode suppression of the BPF can be kept at a high level by adding a varactor to the center of the resonator. The simulated and measured results are given and they show that the differential-mode passband can be tuned from 0.725 GHz to 0.811 GHz and the common-mode suppression is always higher than 25 dB in this frequency range.

ACKNOWLEDGMENT

This work was supported by the National Natural Science Foundation of China under Grants 60901041, 61071086, and 61101002, by Program for New Century Excellent Talents in University (NCET-11-0993), by the Natural Science Foundation of Jiangsu Province, China (Grant No. BK2010272), and by Graduate Research and Innovation Plan Project of the Universities of Jiangsu Province under Grant YKC12066.

REFERENCES

[1] J. Shi and Q. Xue, "Balanced bandpass filters using center-loaded half-wavelength resonators," *IEEE Trans. Microw. Theory Tech.*, vol. 58, no. 4, pp. 970-977, April 2010.

[2] K. T. Chen and S. J. Chung, "A novel compact balanced-to-unbalanced low-temperature co-fired ceramic bandpass filter with three coupled lines configuration," *IEEE Trans. Microw. Theory Tech.*, vol. 56, no. 7, pp. 1714-1720, July 2008.

[3] C. H. Wu, C. H. Wang, and C. H. Chen, "Balanced coupled-resonator bandpass filter using multi-section resonators for common-mode suppression and stopband extension," *IEEE Trans. Microw. Theory Tech.*, vol. 55, no. 8, pp. 1756-1763, Aug. 2007.

[4] C. H. Wu, C. H. Wang, and C. H. Chen, "Novel balanced coupled-line bandpass filters with common-mode noise suppression," *IEEE Trans. Microw. Theory Tech.*, vol. 55, no. 2, pp. 287-295, Feb. 2007.

[5] X. H. Wang, Q. Xue, and W. W. Choi, "A novel ultra-wideband differential filter based on double-sided parallel-strip line," *IEEE Microw. Wireless Compon. Lett.*, vol. 20, no. 8, pp. 471-473, Aug. 2010.

[6] C. H. Lee, C. I. G. Hsu, and C. C. Hsu, "Balanced dual-band BPF with stub-loaded SIRs for common-mode suppression," *IEEE Microw. Wireless Compon. Lett.*, vol. 20, no. 2, pp. 70-72, Feb. 2010.

[7] Y. C. Li and Q. Xue, "Tunable balanced bandpass filter with constant bandwidth and high common-mode suppression," *IEEE Trans. Microw. Theory Tech.,* vol. 59, no. 10, pp. 2452-2460, Oct. 2011.

[8] J. X. Chen, Z. H. Bao, C. Xu, and G. A. Zhang, "Uniplanar tunable bandpass filter using centrally-loaded slot-line resonator," *Microwave and*

Optical Tech. Lett., vol. 52, no. 12, pp. 2805-2807, Dec. 2010.

[9] S. W. Chen, J. W. Wu, J. D. Wu, and J. S. Li, "Tunable active bandpass filter design," *Electron. Lett.*, vol. 47, no. 3, pp. 1019-1021, Sept. 2011.

[10] S. R. Chandler, I. C. Hunter, and J. G. Gardiner, "Active varactor tunable bandpass filter," *IEEE Microwave Guided Wave Lett.*, vol. 3, no. 18, pp. 70-71, Mar. 1993.

[11] X. Y. Zhang and Q. Xue, "High-selectivity tunable bandpass filters with harmonic suppression," *IEEE Trans. Microw. Theory Tech*., vol. 58, no. 4, pp. 964-969, April 2010.

[12] A. Tombak, J. P. Maria, F. T. Ayguavives, J. Zhang, G. T. Stauf, A. -I. Kingon, and A. Mortazawi, "Voltage-controlled RF filter employing thin-film barium-strontium-titanate tunable capacitors," *IEEE Trans. Microw. Theory Tech*., vol. 51, no. 2, pp. 462-467, Feb. 2003.

Qingyuan Lu received the B.Sc. degree from NJU, Nanjing, China, in 2010, and is currently working toward the M.Sc. degree in Electromagnetic Field and Microwave Technology in NTU, China. His research interests include balanced circuits and antenna, etc.

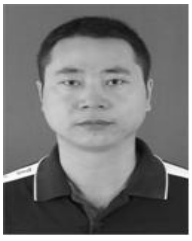

Jianxin Chen received the M.Sc. degree from UESTC, Chengdu, China, in 2004, and the Ph.D. degree from CITYU, Kowloon, Hong Kong, in 2008. He is currently a Professor with Nantong University, Jiangsu Province, China. His research interests include RF/microwave active and passive circuit designs.

Liheng Zhou received the M.Sc. degree from NJUST, Nanjing, China, in 2007. His research interests is the design of microwave circuit.

Hui Tang received the M.Sc. degree from SHU, Shanghai, China, in 2004. Her research interests is RF circuits and antennas.

A Novel Design of Reconfigurable Monopole Antenna for UWB Applications

Nasser Ojaroudi [1], Shervin Amiri [2], and Fatemeh Geran [1]

[1] Faculty of Electrical & Computer Engineering
Shahid Rajaee Teacher Training University, Tehran, Iran
n_ojaroudi@srttu.edu, geran_e@yahoo.com

[2] Scientific Member of Electrical Engineering Department
Iranian Research Organization for Science and Technology (IROST)
Tehran, Iran, amiri@irost.org

Abstract ─ In this paper, a kind of reconfigurable monopole antenna with multi-resonance and switchable band-notched function is designed and manufactured whose frequency characteristics can be reconfigured electronically to have a single-band notch function in order to block interfering signals from 5.15 GHz - 5.35 GHz HiperLAN, 5 GHz - 6 GHz WLAN or 7.25 GHz - 7.75 GHz for downlink of X-band satellite communication systems. The proposed antenna consists of a square radiating patch, feed-line, and a ground plane with a Fork-shaped conductor-backed plane. By adding an inverted T-shaped and a pair of L-shaped parasitic structures in the ground plane, additional resonances are excited and hence much wider impedance bandwidth can be produced, especially at the higher band, which provides a wide usable fractional bandwidth of more than 135% (3.05 GHz-16.51 GHz). In order to generate reconfigurable band-stop performance, we use a pair of PIN diodes within the antenna configuration. By changing the ON/OFF conditions of the PIN diodes, the antenna can be used to generate a single notch band to isolate and block any interference in the UWB frequency range. The proposed antenna has a small dimension of $12 \times 18 \times 1.6$ mm^3.

Index Terms ─ Band-notched performance, conductor-backed plane, PIN diode, reconfigurable monopole antenna, and UWB wireless communication.

I. INTRODUCTION

An ultra-wideband (UWB) system requires small low-cost antenna with omni-directional radiation patterns and large bandwidth [1]. In UWB communication systems, one of key issues is the design of a compact antenna while providing wideband characteristic over the whole operating band. Consequently, several planar monopoles with different geometries have been experimentally characterized and automatic design methods have been developed to achieve the optimum planar shape [2-3]. Moreover, other strategies to improve the impedance bandwidth have been investigated [4-6]. In [7] and [8], a coupled T-shaped strip in the bottom side of the FR-4 substrate acts as a conductor-backed plane, and it is created to enhance the gain of the monopole antenna at the lower and middle of the frequency band such that the gain of the proposed antenna over the complete bandwidth remains nearly constant.

The frequency range for UWB systems between 3.1 GHz – 10.6 GHz will cause interference to the existing wireless communication systems for example C-band (3.7 GHz – 4.2 GHz) systems or the wireless local area network (WLAN) for IEEE 802.11a operating in 5.15 GHz – 5.35 GHz or 7.25 GHz – 7.75 GHz for downlink of X-band satellite communication systems, so the UWB antenna with a band-notched function is required. Lately, to generate the frequency band-notched function,

Submitted On: Jan. 1, 2013
Accepted On: Apr. 13, 2013

modified several planar monopole antennas with band-notched characteristic have been reported [4-7]. In [4], [5] and [6], different shapes of the slots (i.e., square ring, W-shaped, and folded trapezoid) are used to obtain the desired band notched characteristics. Single and multiple [7] half-wavelength U-shaped to generate the frequency band-notch function, modified planar slits are embedded in the radiation patch to generate the single and multiple band-notched functions, respectively. In order to effectively and fully utilize the UWB spectrum and to improve the performance of the UWB system, it is desirable to design the UWB antenna with reconfigurable notch band [9-10]. It will help to minimize the interference between the systems and whenever there is no coexistence system, the structure of the antenna can be transformed in a way that leads to a whole coverage of UWB spectrum. In [9] for reconfigurable performance of rejection band, which is between 5 GHz to 6 GHz, RF MEMS is utilized while in [10] diodes are used for the same reason. That demands the use of 'smart' reconfigurable antennas capable of cancelling in-band interference. Hence, an UWB antenna with reconfigurable band-rejection characteristics at the WLAN or C-band satellite frequencies is highly desirable.

This paper focuses on a multi-resonance square monopole antenna with reconfigurable band-notched performance for UWB applications. In the proposed structure, multi-resonance characteristic is provided by using a pair of L-shaped and an inverted T-shaped conductor-backed plane. By implementing two PIN diodes across the parasitic structures and biasing these active elements, variable frequency band-notched function can be achieved. Good VSWR and radiation pattern characteristics are obtained in the frequency band of interest.

II. ANTENNA DESIGN

The square monopole antenna fed by a microstrip line is shown in Fig. 1, which is printed on an FR4 substrate of thickness 1.6 mm, permittivity 4.4, and loss tangent 0.018. The width W_f of the microstrip feed-line is fixed at 2 mm. The basic antenna structure consists of a square patch, a feed-line, and a ground plane. The square patch has a width W. The patch is connected to a feed line of width W_f and length L_f, as shown in Fig. 1. On the other side of the substrate, a conducting ground plane of width W_{sub} and length L_{gnd} is placed. The proposed antenna is connected to a 50 Ω SMA connector for signal transmission.

To design a novel reconfigurable antenna, the modified fork-shaped conductor-backed plane is embedded on the basic antenna structure, mentioned above. Based on the current distribution analysis in UWB frequency band, it is observed that the currents on the bottom edge of the monopole's radiating patch, are distributed vertically at lower frequencies, while at higher frequencies this currents are distributed horizontally [11].

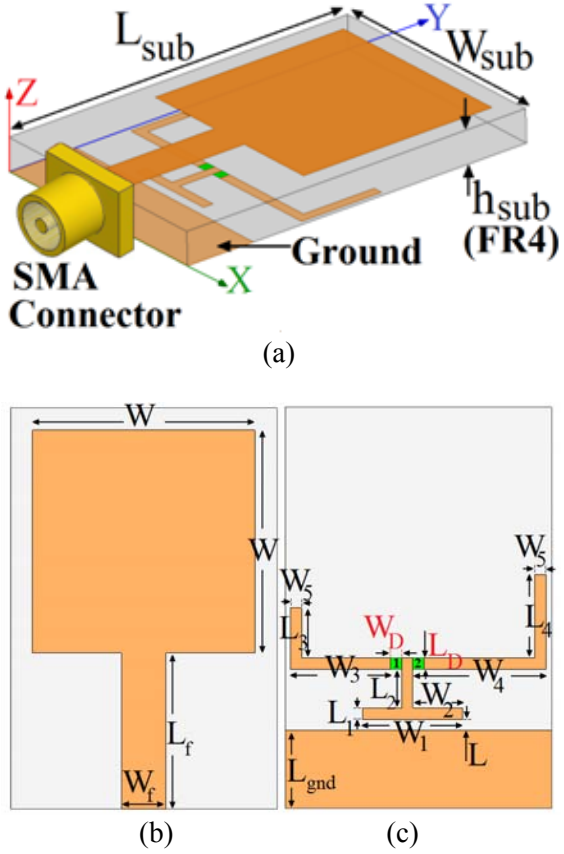

Fig. 1. Geometry of the proposed antenna; (a) side view, (b) square radiating patch, and (c) ground plane structure.

The modified T- and L-shaped parasitic structures are playing important roles in the broadband characteristics of this antenna, because these can adjust the electromagnetic coupling effects between the patch and the ground plane, and improve its impedance bandwidth without any

cost of size or expense [7-10]. This phenomenon occurs because, with the use of conductor-backed plane structures in air gap distance, additional couplings are introduced between the bottom edge of the square patch and the ground plane [2]. The final dimensions of the designed antenna are specified in Table 1.

Table 1: Final dimensions of the proposed antenna.

Param.	mm	Param.	mm	Param.	mm
W_{Sub}	12	L_{Sub}	18	L_{gnd}	3.5
W	10	L	0.5	W_f	2
L_f	7	W_1	4.5	L_1	0.5
W_2	2	L_2	12	W_3	4.75
L_3	2.75	W_4	5.75	L_4	3.5
W_5	0.5	L_D	0.5	W_D	0.5

III. RESULTS AND DISCUSSIONS

In this section, the planar monopole antenna with various design parameters was constructed and the numerical and experimental results of the input impedance and radiation characteristics are presented and discussed. The parameters of this proposed antenna are studied by changing one parameter at a time and fixing the others. The simulated results are obtained using the Ansoft simulation software high-frequency structure simulator (HFSS) [12].

A. UWB monopole antenna with multi-resonance characteristic

Figure 2 shows the structure of the various antennas used for simulation studies. VSWR characteristics for ordinary square monopole antenna (Fig. 2 (a)), with an inverted T-shaped conductor-backed plane (Fig. 2 (b)), and with inverted T-shaped and a pair of L-shaped conductor-backed plane structures (Fig. 2 (c)) are compared in Fig. 3. As shown in Fig. 3, it is observed that by using these modified parasitic structures, additional third and fourth resonances are excited respectively, and hence the bandwidth is increased.

In the proposed antenna configuration, the ordinary square monopole can provide the fundamental and next higher resonant radiation band at 4 GHz and 8 GHz, respectively, in the absence of parasitic structures in the ground plane. The upper frequency bandwidth is significantly affected by using the inverted T-shaped conductor-backed plane in the ground plane. This behavior is mainly due to the change of surface current path by the dimensions of the inverted T-shaped structure as shown in Fig. 4 (a). In addition, by adding a pair of modified L-shaped conductor-backed plane on the other side of the substrate, the impedance bandwidth is effectively improved at the upper frequency [6]. The L-shaped structures can be regarded as a parasitic resonator electrically coupled to the square monopole.

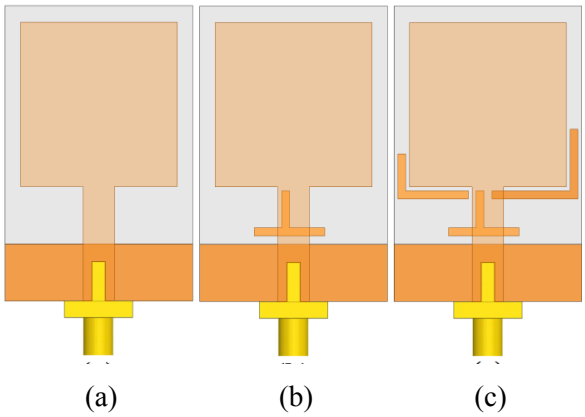

Fig. 2. (a) Ordinary square antenna, (b) the square antenna with an inverted T-shaped parasitic structure, and (c) the square antenna with inverted T-shaped and a pair of L-shaped conductor-backed plane.

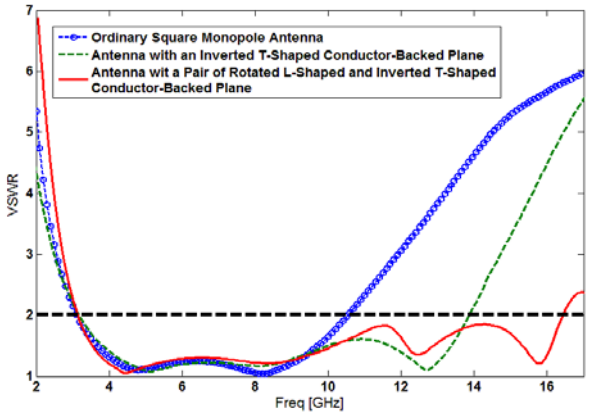

Fig. 3. Simulated VSWR characteristics for the antennas shown in Fig. 2.

As shown in Fig. 4 (b), the currents concentrated on the edges of the interior and exterior of the pair of L-shaped conductor-backed plane at fourth resonance frequency (14.3 GHz). This figure shows that the electrical current for the fourth resonance frequency (Fig. 4 (b)) does change the direction along the bottom edge of the square radiating patch. Therefore, the antenna impedance changes at this frequency, the radiating power and bandwidth will increases. Furthermore, the radiation efficiency will increase. However, the resonant resistance is decreased [9].

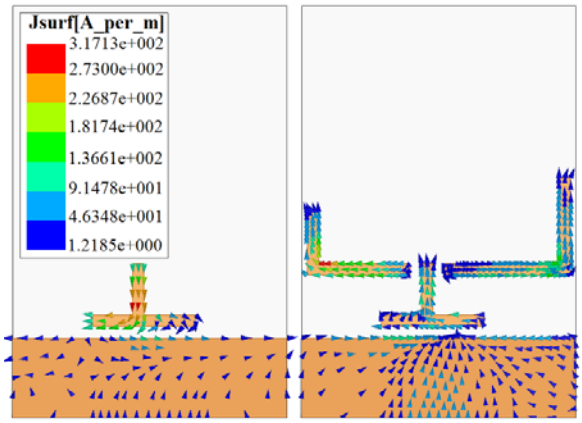

(a) (b)

Fig. 4. Simulated surface current distribution in the ground plane for (a) the square antenna with inverted T-shaped conductor-backed plane at third resonance frequency (12.5 GHz) and (b) the proposed antenna at fourth resonance frequency (14.3 GHz).

B. UWB monopole antenna with reconfigurable band-notched performance

Geometry of the proposed reconfigurable monopole antenna for D_1 and D_2 = ON (Fig. 5 (a)), D_1 = ON and D_2 = OFF (Fig. 5 (b)), and D_1 = OFF and D_2 = ON (Fig. 5 (c)) were shown in Fig. 5. VSWR characteristics for the various reconfigurable structures of the proposed antenna were shown in Fig. 6. By implementing two PIN diodes across the parasitic structures and biasing these active elements, variable frequency band-notched function can be achieved.

For applying the DC voltage to PIN diodes, metal strips with dimensions of 1.5 mm × 0.6 mm were used inside the main slot. In the introduced design, HPND-4005 beam lead PIN diodes [13] with extremely low capacitance were used. For biasing PIN diodes a 0.7 volts supply is applied to metal strips. The PIN diodes exhibit an ohmic resistance of 4.6 Ω and capacitance of 0.017 pF in the ON and OFF states, respectively. By turning diodes ON, the metal protruded *L* -shaped strips are connected to the inverted T-shaped strip and become a part of it. The desired notched frequency band can be selected by varying the states of the PIN diodes, which changes the total equivalent length of the strip.

In order to understand the phenomenon behind switching electronically between band-notched function, the simulated current distributions on the ground plane for the proposed reconfigurable antenna at notched frequencies for ON and OFF statuses of the p-i-n diodes, are presented in Fig. 7. Figure 7 (a) presents the simulated current distributions on the ground plane for D_1 and D_2 = ON at the second notched frequency (5.5 GHz). As shown in Fig. 7 (a), at the notched frequency the current flows are more dominant around of the fork-shaped conductor-backed plane structure. It is found that by changing the ON/OFF conditions of the PIN diodes the antenna can be used to generate a single notch band to isolate and block any interference in the frequency bands.

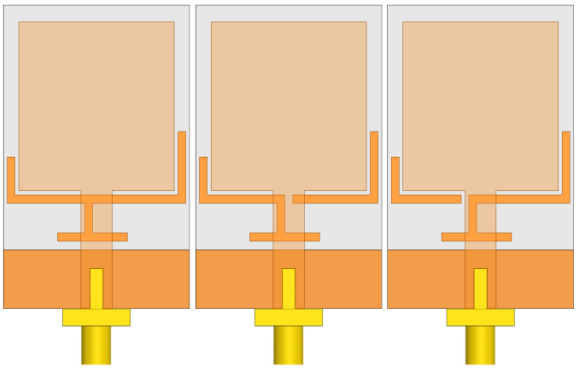

(a) (b) (c)

Fig. 5. Configuration of the proposed square antenna, (a) D_1 and D_2 = ON, (b) D_1 = ON and D_2 = OFF, and (c) D_1 = OFF and D_2 = ON.

Figures 7 (b) and (c) show the simulated current distributions on the ground plane for D_1 = OFF and D_2 = ON and D_1 = ON and D_2 = OFF at the notched frequencies (5.25 GHz and 7.5 GHz).

As shown in Fig. 7 (b), at the first notched frequency (5.25 GHz), the current mainly concentrates on the left hand L-shaped strip, and also it can be seen that the electrical current does change its direction along the left hand L-shaped strip. Finally, the current mainly concentrates on the interior and exterior edges of the right hand L-shaped strip at the third notched frequency (7.5 GHz), as shown in Fig. 7 (c). It is found that by changing the conditions of the PIN diodes we can give a variable frequency band-notched function.

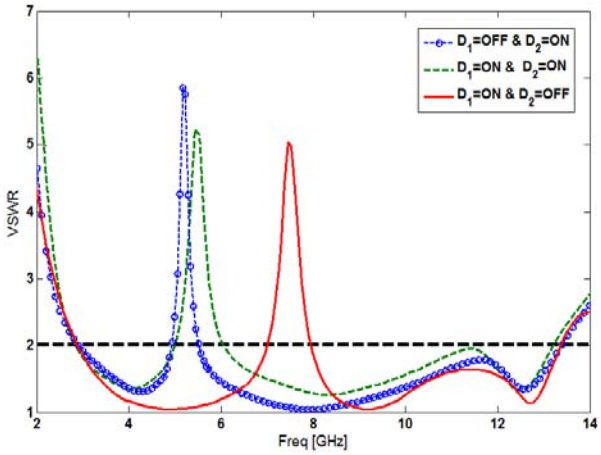

Fig. 6. Simulated VSWR characteristics for the proposed antenna with various structures shown in Fig. 5.

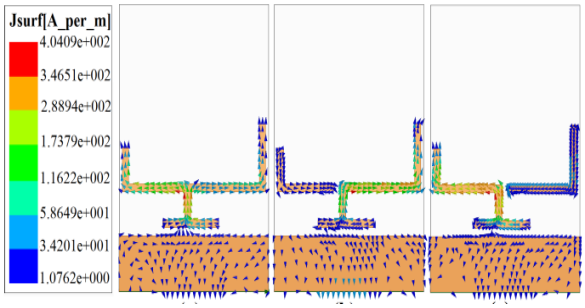

(a) (b) (c)

Fig. 7. Simulated surface current distribution in the ground plane for the proposed antenna (a) at 5.5 GHz (D_1 and D_4 = ON), (b) at 5.25 GHz (D_1 = ON and D_2 = OFF), and (c) 7.5 GHz (D_1 = OFF and D_2 = ON).

The proposed antenna with final design, as shown in Fig. 8 was built and tested. Measured VSWR characteristic of the proposed antenna with multi-resonance and reconfigurable band notched function was shown in Fig .9. The fabricated antenna has the frequency band of 3.05 GHz to 11.5 GHz with a bad-stop function around of 5 GHz - 6 GHz. However, as shown in Fig. 8, there exists a discrepancy between measured data and the simulated results. This discrepancy is mostly due to a number of parameters such as the fabricated antenna dimensions as well as the thickness and dielectric constant of the substrate on which the antenna is fabricated, the wide range of simulation frequencies, and also the effect of the p-i-n diode and its biasing circuit. In order to confirm the accurate return loss characteristics for the designed antenna, it is recommended that the manufacturing and measurement processes need to be performed carefully. Moreover, SMA soldering accuracy and FR4 substrate quality need to be taken into consideration.

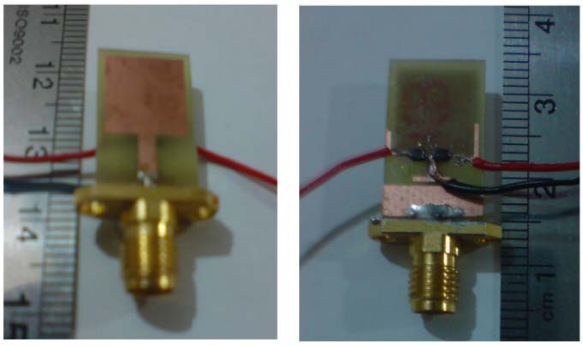

(a) (b)

Fig 8. Photograph of the realized printed monopole antenna, (a) top view and (b) bottom view.

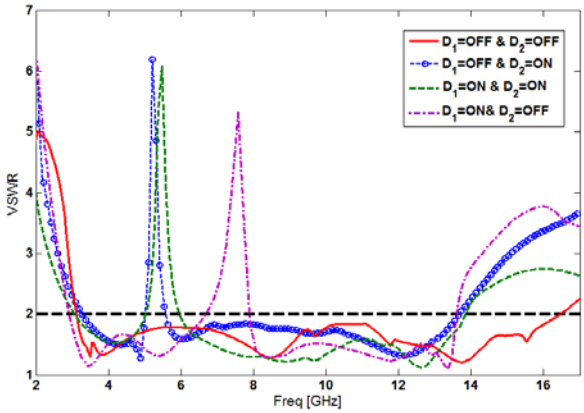

Fig. 9. Measured VSWR characteristics for the proposed antenna with reconfigurable function.

Figure 10 shows the measured radiation patterns at resonances frequencies including the co-polarization and cross-polarization in the H-plane (*x*-*z* plane) and E-plane (*y*-*z* plane). The main purpose of the radiation patterns is to demonstrate that the antenna actually radiates over a wide frequency band. It can be seen that the radiation patterns in the *x*-*z* plane are nearly omni-directional for the four frequencies.

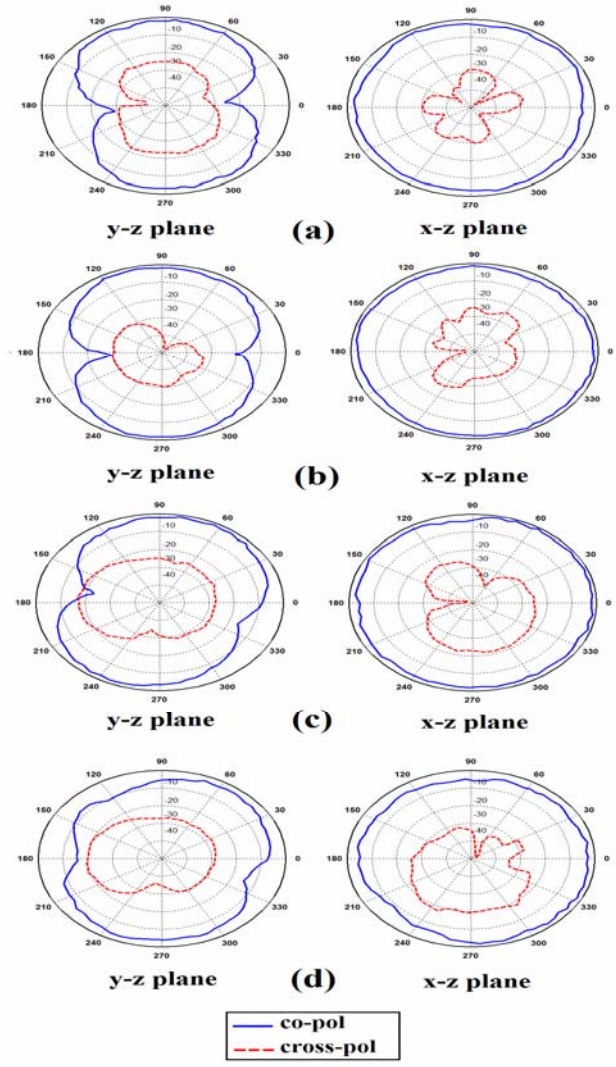

Fig. 10. Measured radiation patterns of the proposed antenna for D_1 and D_2 = OFF, (a) 4 GHz, (b) 7 GHz, (c) 11 GHz, and (d) 14.5 GHz.

IV. CONCLUSION

In this letter, a novel compact printed monopole antenna (PMA) with reconfigurable function has been proposed for UWB applications. In the proposed structure, multi-resonance characteristic is provided by using a pair of L-shaped and an inverted T-shaped conductor-backed plane. By implementing two PIN diodes across the parasitic structures and biasing these active elements, variable frequency band-notched function can be achieved. The fabricated antenna satisfies the 10 dB return loss requirement from 3.05 GHz to 16.51 GHz with variable band-notched function to block interfering signals from 5.15 GHz - 5.35 GHz HiperLAN, 5 GHz - 6 GHz WLAN or 7.25 GHz - 7.75 GHz for downlink of X-band satellite communication systems. The proposed antenna has a simple configuration and is easy to fabricate. Good VSWR and radiation pattern characteristics are obtained in the frequency band of interest. Experimental results show that the proposed antenna could be a good candidate for UWB application.

ACKNOWLEDGMENT

The authors are thankful to Microwave Technology (MWT) company staff for their beneficial and professional help (www.microwave-technology.com).

REFERENCES

[1] H. Schantz, *The Art and Science of Ultra Wideband Antennas*, Artech House, 2005.

[2] Sh. Yazdanifard, R. A. Sadeghzadeh, and M. Ojaroudi, "Ultra-wideband small monopole antenna with variable frequency band-notch function," *Progress In Electromagnetics Research C*, vol. 15, pp. 133-144, 2010.

[3] M. Ojaroudi, Gh. Ghanbari, N. Ojaroudi, and Ch. Ghobadi, "Small square monopole antenna for UWB applications with variable frequency band-notch function," *IEEE Antennas and Wireless Propagation Letters*, vol. 8, pp. 1061-1064, 2009.

[4] D. Piazza, P. Mookiah, M. D'Amico, and K. R. Dandekar, "Experimental analysis of pattern and polarization reconfigurable circular patch antennas for MIMO systems," *IEEE Trans. Veh. Technol.*, vol. 59, pp. 2352-2362, 2010.

[5] S. L. Steven Yang, A. A. Kishk, and K. F. Lee, "Frequency reconfigurable U-slot microstrip patch antenna," *IEEE Antennas and Wireless Propagation Letters*, vol. 7, pp. 127-129, 2008.

[6] J. William and R. Nakkeeran, "CPW-fed UWB slot antenna with reconfigurable rejection bands," *Proc. of Int. Conf. on Control, Communication, and Power Engineering*, 2010.

[7] M. Ojaroudi, Sh. Yzdanifard, N. Ojaroudi, and M. Nasser-Moghaddasi, "Small square monopole antenna with enhanced by using inverted T-shaped slot and conductor-backed plane," *IEEE Transactions on Antenna and Propagation*, vol. 59, no. 2, pp. 670-674, Feb. 2011.

[8] M. Ojaroudi, Sh. Yzdanifard, N. Ojaroudi, and R. A. Sadeghzadeh, " Band-notched small square-ring antenna with a pair of T-shaped strips protruded inside the square ring for UWB applications," *IEEE Antennas and Wireless Propagation Letters*, vol. 10, pp. 227-230, 2011.

[9] S. Nikolaou, N. D. Kingsley, G. E. Ponchak, J. Papapolymerou, and M. M. Tentzeris, "UWB elliptical monopoles with a reconfigurable band notch using MEMS switches actuated without bias lines," *IEEE Transactions on Antenna and Propagation*, vol. 57, no. 8, pp. 2242-2251, August 2009.

[10] N. Ojaroudi, Sh. Amiri, and F. Geran, "Reconfigurable monopole antenna with controllable band-notched performance for UWB communications," *20th Telecommunications Forum*, TELFOR 2012.

[11] G. Zhang, J. S. Hong, B. Z. Wang, and G. Song, "Switched band-notched UWB/ WLAN monopole antenna," *Applied Computational Electromagnetics Society (ACES) Journal*, vol. 27, no. 3, pp. 256-260, March 2012.

[12] Ansoft High Frequency Structure Simulation (HFSS), ver. 13, Ansoft Corporation, 2010.

[13] HPND-4005, "Beam lead PIN diode," Avago Technologies.

Nasser Ojaroudi was born in 1986 in Germi, Iran. He received his B.Sc. degree in Electrical Engineering from Azad University, Ardabil Branch. From 2011, he is working toward the M.Sc. degree in Telecommunication Engineering at Shahid Rajaee Teacher Training University. His research interests include ultra-wideband (UWB) microstrip antennas wireless communications, reconfigurable structures, and electromagnetic theory.

Shervin Amiri was born in Tehran, Iran, in 1966. He received his B.Sc., M.Sc. and Ph.D. from Iran University of Science & Technology (IUST) in communication systems. Now he is a Scientific Member of Electrical Engineering Department in Iranian Research Organization for Science and Technology (IROST). His research interest fields are Antenna and RF subsystems in Microwave and mm-wave Bands and Radar systems. He is supervisor of many Ph.D. and M.Sc. students in the fields of communication system and subsystems.

Fatemeh Geran was born in Ghaemshar, Iran in 1977. She received her B.Sc. degree in Electrical Engineering (Telecommunication) from Tehran University, Tehran, Iran in 1999. Also, she received her M.Sc. and PHD degrees in Electrical Engineering (Telecommunication) from Tarbiat Modares University, Tehran, Iran, in 2003 and 2009, respectively. She is currently as an Assistant Professor in Electrical Engineering at Shahid Rajaee Teacher Training University, Tehran, Iran. Her research interest fields are antenna and RF subsystems in microwave and mm-wave Bands.

Miniaturized Microstrip Lowpass Filter with Ultra-Wide Stopband

Yan Dou [1], Jianpeng Wang [1], Haifei Cui [1], and Jia-Lin Li [2]

[1] Ministerial Key Laboratory of JGMT,
Nanjing University of Science and Technology, Nanjing 210094, China
eleyandou@gmail.com, elejpwang@yahoo.com.cn, elehfc@gmail.com

[2] School of Physical Electronics,
University of Electronic Science and Technology of China, Chengdu 610054, China
jialinuestc@hotmail.com

Abstract ─ A new microstrip lowpass filter with compact size and ultra-wide stopband is presented. Using triangular patch resonators and butterfly resonator with four 45˚ radial "wing" patches, the introduced filter can successfully realize compact design and ultra-wide stopband. To further reduce the circuit size of the filter, the meander transmission lines are also adopted in the design. A demonstration filter with 3 dB cutoff frequency at 1.6 GHz has been designed, fabricated, and measured. Measured results show that the lowpass filter has an ultra-wide stopband bandwidth of 153.9 %, which is able to suppress the 11th harmonic response. Furthermore, it also has a small size of 14 × 15 mm^2, which corresponds to 0.114 λg × 0.122 λg, where λg is the guided wavelength at 1.6 GHz.

Index Terms ─ Lowpass filter and microstrip, ultra-wide stopband.

I. INTRODUCTION

Planar lowpass filters with compact size and high performance are frequently required in many microwave communication systems to suppress harmonics and spurious signals. Conventional method to realize microstrip lowpass filter is to utilize high-low impedance lines with shunt stubs and semi-lumped element for their remarkable characteristics. However, they provide a low stopband rejection and a relative flat roll-off characteristic together with a large size [1]. Therefore, techniques to reduce the filter size and enhance the performance have been widely studied in recent years [2-11].

One method to achieve good stopband performance is by cascading multi-resonators [2-5]. For example, in order to realize sharp roll-off and wide stopband suppression, Li *et al.* designed a lowpass filter by cascading multiple stepped impedance hairpin resonators in [2]. Although sharp roll-off had been achieved, this brings drawbacks in terms of large size and higher loss within the passband. By cascading multiple semi-circle and semi-ellipse patch resonators, Hayati *et al.* designed a lowpass filter with sharp roll-off and 6th harmonic response in [3]. But it is hard to get compact size and high performance simultaneously. Therefore, to further improve the stopband performance, Ma *et al.* proposed a lowpass filter by cascading LC resonant structure and transformed radial stubs in [4]. Although better than 13th harmonic suppression had been realized, this method always results in large circuit size and increases design complexity.

On the other hand, filters with good stopband performance can also be realized by using modified stepped impedance resonators. In [6], the conventional low-impedance stubs are replaced by the radial stubs, which have intrinsic wide stopband characteristic to realize a wide stopband rejection. Although compact design had been realized with this method, the roll-off performance is not ideal and further improvement should be

Submitted On: Dec. 26, 2012
Accepted On: Apr. 13, 2013

carried out in stopband bandwidth. Recently, a compact ellipse function microstrip lowpass filter with ultra-wide stopband is proposed in [7]. The design is based on cascading high-impedance transmission lines and low-impedance butterfly resonators with two 55^0 radial "wing" patches to realize compact size and harmonic suppression. Furthermore, four triangle patch resonators are also utilized to achieve wide stopband. However, the transmission performance in the passband is not ideal due to the increasing of circuit discontinuity in the design. On the other hand, defected ground structure (DGS) and multilayer technique are also utilized to realize lowpass filter in [8-10]. Small size was realized, nevertheless, this method increases the complexity of circuit design.

The motivation of this paper is to design a new compact microstrip lowpass filter with ultra-wide stopband and good transmission performance. Both triangular patches and butterfly resonator with four 45^0 radial "wing" patches are used in the design to achieve compact size and ultra-wide band rejection. Meander transmission lines are also adopted in the design to further reduce the filter size. Results indicate that the proposed filter exhibits an ultra-wide stopband bandwidth from 2.37 GHz to 18.2 GHz with better than 17 dB suppression degree, a good passband performance with less than 0.3 dB passband insertion loss, and a compact electrical size of 0.114 $\lambda g \times 0.122\ \lambda g$, where λg is the guided wavelength at 1.6 GHz.

II. CIRCUIT DESIGN

Figure 1 shows the layout of the proposed lowpass filter. The dimensions of the presented lowpass filter are listed in Table 1. The substrate used here is Duroid 5870 with a relative dielectric constant of 2.33 and a thickness of 0.7874 mm. As can be seen from Fig. 1, the proposed filter consists of high–low impedance microstrip main transmission lines and two types of resonators, i.e., resonators 1 and 2. Resonator 1 is a triangular patch. Resonator 2 is composed of a high impedance transmission line and a butterfly resonator consists of four 45^0 radial "wing" patches, which are connected in series. Figure 2 shows the lumped-element equivalent circuit of the presented lowpass filter. In the circuit, C_a mainly represents the capacitance between the triangular patch and the ground plane while C_b mainly represent the capacitance between one of the "wing" patches of the middle butterfly resonator and the ground plane. C_{bb} mainly contains the coupling capacitance between the two "wing" patches of the butterfly resonator. The capacitance C_{ab} is formed by the capacitive coupling between the triangular patch and the middle butterfly resonator patch. The high impedance line is mainly represented by the inductance L and L'. It is obviously that the location of the 3 dB cutoff frequency and the stopband performance is mainly controlled by the values of L, C_a and C_b, which are determined by the structure parameters of W_2, l_1 and r. And the capacitors and inductors values of the lumped-element equivalent circuit of the proposed lowpass filter are given as follows: C_a = 1.1 PF, C_b = 1 PF, C_{ab} = 0.1 fF, C_{bb} = 0.1 fF, L = 8 nH, and L'= 0.1 fH.

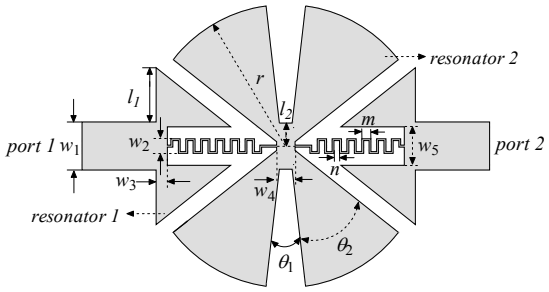

Fig. 1. Layout of the proposed lowpass filter.

Table 1: Structure parameters of the proposed lowpass filter.

l_1	l_2	w_1	w_2	w_3	w_4
3.9	1.1	2.6	1.2	0.6	1
w5	m	n	r	θ1(^{0})	θ2(^{0})
2.1	0.5	0.3	7.5	7	45

Unit: mm, unless specified.

To illustrate the design theory, frequency responses with the two types of resonators are primary studied. Figure 3 (a) shows the frequency response of the filter only with resonator 1. It can be seen that the filter exhibits a wide stopband

with one transmission zero (TZ_1), which is caused by the resonance of the loaded triangular patches, and its frequency location can be controlled by the structure parameters of the triangular patch resonators. However, the roll-off performance is not ideal. Thus, butterfly resonator is also introduced to the filter to improve the roll-off and the stopband performance as shown in Fig. 3 (b). Since the loaded resonator 2 is not only enhanced by the shunt capacitance of the main transmission line but also by the couple with the neighboring triangular patches, i.e., resonator 1, and this will provide an extra finite transmission zero (TZ_2) inside the stopband. And the frequency location of the transmission zero (TZ_2) can be controlled by the structure parameters of the filter properly adjusted. Furthermore, the harmonic suppression responses of the proposed lowpass filter according to different parameter values are compared in Fig. 4. As can be seen from Fig. 4 (a), the length of the triangular patch, i.e., l_1, plays an important role in improving the stopband performance. Good stopband performance is obtained as l_1 is 3 mm. Fig. 4 (b) shows when θ_2 is different from 45^0, an undesired harmonic will be generated in the stopband and the increase of θ_2 will make the first zero (TZ_2) shift closer to the cutoff frequency. So, if we place it close to the fringe of the passband by choosing proper structure parameters, a lowpass filter with a sharp roll-off and wide stopband rejection can be achieved. On the other side, the loaded butterfly resonator can also result in high slow-wave effect as the increasing of shunt capacitance of the main transmission line. So the size of the proposed lowpass filter has been reduced compared with conventional lowpass filters.

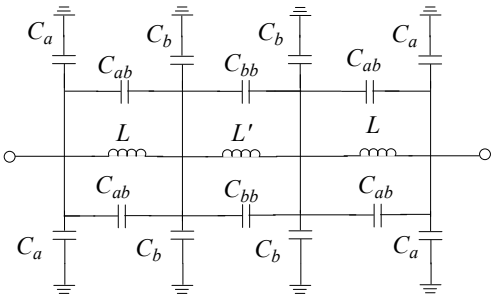

Fig. 2. Lumped-element equivalent circuit of the proposed lowpass filter.

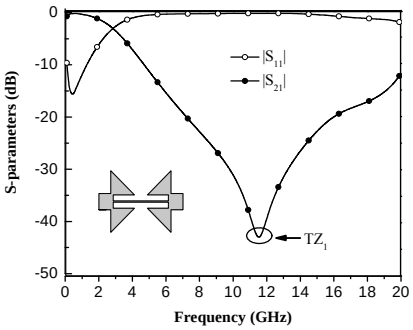

(a)

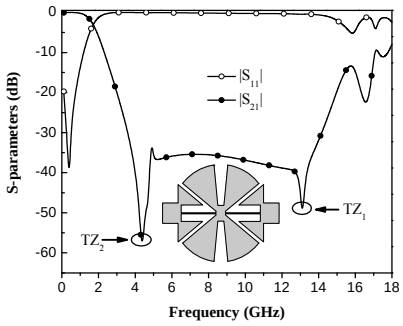

(b)

Fig. 3. Simulated S-parameters of studied resonator for the (a) filter with only resonator 1 and (b) the filter with resonators 1 and 2.

Figure 5 shows the simulated current distributions at different frequencies to display the signal trend in the passband and stopband. The current distribution in passband is shown in Fig. 5 (a). It can be seen that the signals at 0.5 GHz can be transferred from port 1 to port 2 along the high impedance meander lines. Figure 5 (b) shows another case of frequency at 10 GHz, which is in the stopband. It is found that the signals at 10 GHz are blocked by the high impedance lines.

To further reduce the size of the filter in our design, we also use the meander transmission line to replace the high-impedance section of the main transmission line. Therefore, combine the techniques mentioned above, a new microstrip lowpass filter with compact size and high stopband performance is realized. The proposed filter is designed based on the analysis mentioned above. Figure 6 is the photograph of the fabricated fiilter.

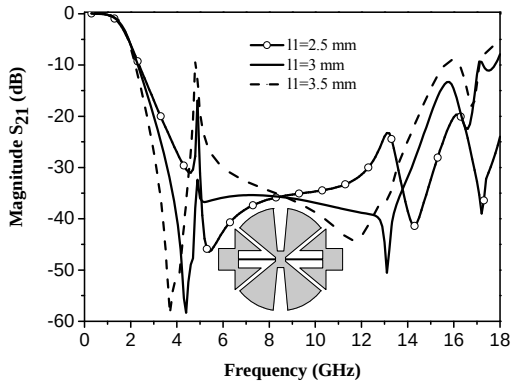

(a)

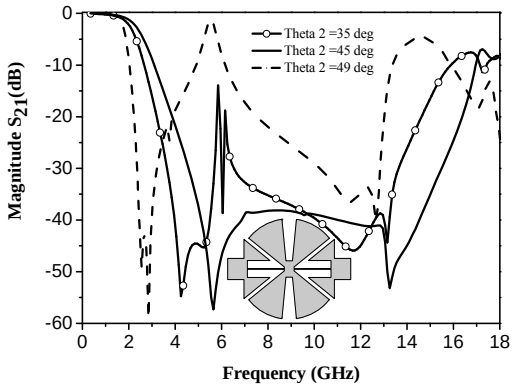

(b)

Fig. 4. Simulated S-parameters of the proposed filter: (a) simulated $|S_{21}|$ with different l and (b) simulated $|S_{21}|$ with different θ_2.

III. SIMULATION AND MEASUREMENT RESULTS

Simulation was accomplished using EM simulation software Ansoft HFSS 12. The comparisons between the circuit model EM simulated results and the equivalent lumped element circuit results are given in Fig. 7. Measurement was carried out on an Agilent 8722ES network analyzer. Figure 8 shows the simulated and measured results. As we can see from Fig. 8, the measured 3 dB cutoff frequency is at 1.6 GHz. Inside the passaband the insertion loss is less than 0.3 dB from DC to 1.05 GHz, which is to ensure the good transmission performance in the passband. In addition, the filter provides 11th harmonic suppression performance, as the spurious frequencies are suppressed from 2.37 GHz to 18.2 GHz with better than 17 dB suppression degree. The measured group delay in the passband is 0.23 ns – 0.5 ns, as shown in Fig. 9. Furthermore, the overall size of the fabricated filter is only 14 × 15 mm^2, which corresponds to a compact electrical size of 0.114 λg × 0.122 λg, where λg is the guided wavelength at 1.6 GHz. For comparison, Table 2 summarizes the performance of some recently published lowpass filters. As can be observed from the table, the presented filter has the properties of compact size, simple circuit topology, and ultra-wide stopband among the quoted filters.

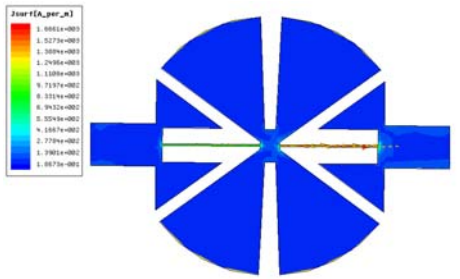

(a)

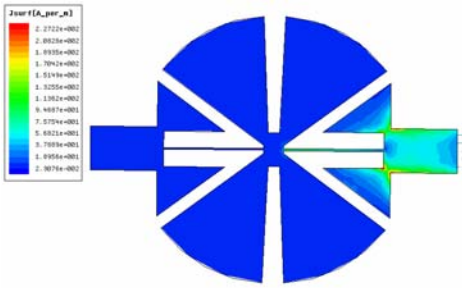

(b)

Fig. 5. Simulated current distribution of the proposed lowpass filter: (a) simulated current distribution at 0.5 GHz and (b) simulated current distribution at 10 GHz.

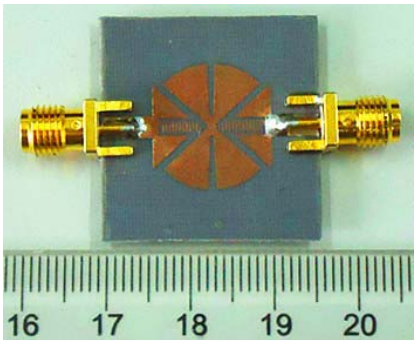

Fig. 6. Photograph of the proposed lowpass filter.

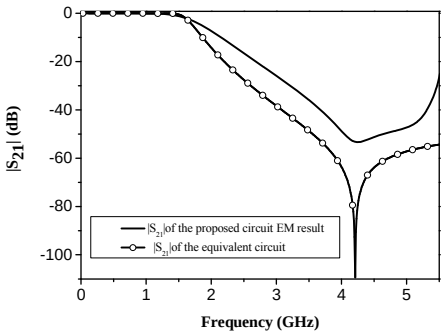

Fig. 7. Comparisons between the equivalent circuit model calculated results and EM simulates results.

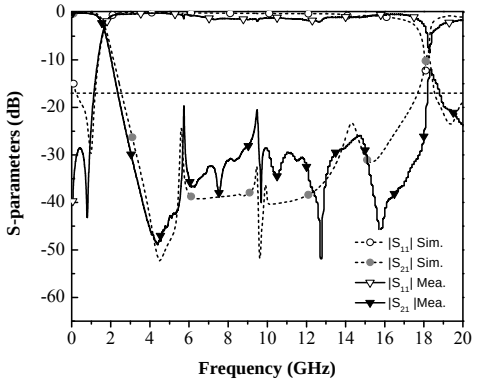

Fig. 8. Simulated and measured performance of proposed filter.

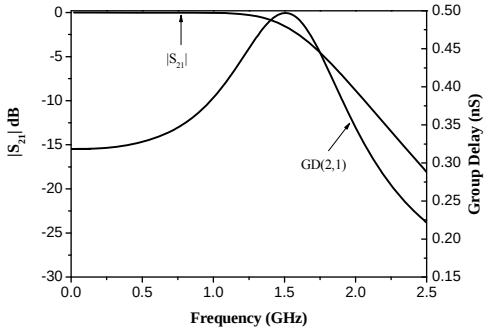

Fig. 9. Measured IL and group delay in the passband range of the proposed lowpass filter.

IV. CONCLUSION

A new microstrip lowpass filter is presented in this letter. One prototype filter with 3 dB cutoff frequency at 1.6 GHz has been demonstrated. Results indicate that the demonstrator exhibits the properties of compact size, good passband performance, and ultra-wide stopband. With all these good features, the proposed filter could be widely applied in microwave communication systems.

Table 2: Performance comparisons among published filters and the proposed one.

Ref.	Circuit size	Insertion loss	Harmonic suppression
2	0.114 λg × 0.105 λg	0.4 dB	6th
3	0.395 λg × 0.151 λg	0.33 dB	6th
4	0.31 λg × 0.24 λg	1 dB	13th
5	0.141 λg × 0.083 λg	0.5 dB	8th
6	0.104 λg × 0.104 λg	1.5 dB	7th
7	0.111 λg × 0.091 λg	0.4 dB	16th
11	0.104 λg × 0.123 λg	0.39 dB	10th
This work	0.114 λg × 0.122 λg	0.3 dB	11th

ACKNOWLEDGEMENT

This work was supported by the Nature Science Foundation of China under Grant No.61101047 and the Specialized Research Fund for the Doctoral Program by the Ministry of Education of China under Grant No.20113219120015.

REFERENCES

[1] D. M. Pozar, *Microwave Engineering*, 3rd ed. New York: Wiley, Ch. 7, pp. 412-415, 2005.

[2] L. Li, Z. -F. Li, and J. -F. Mao, "Compact lowpass filters with sharp and expanded stopband using stepped impedance hairpin units," *IEEE Microw. Wirel. Compon. Lett.,* vol. 20, no. 6, pp. 310-312, June 2010.

[3] M. Hayati, A. Sheikhi, and A. Lotfi, "Compact lowpass filter with wide stopband using modified semi-elliptic and semi-circular microstrip patch

resonator," *IEE Electron. Lett.,* vol. 46, no. 22, pp. 1507-1509, Oct. 2010.

[4] K. -X. Ma and K. -S. Yeo, "New ultra-wide stopband low-pass filter using transformed radial stubs," *IEEE Trans. Microw. Theory Tech.,* vol. 59, no. 3, pp. 604-611, Mar. 2011.

[5] K. -Y. Zhao, L. Li, and Y. -M. Wang, "A novel lowpass filter using three corner-cutting T-shaped compact microstrip resonator cells," *Engineering and Technology (S-CET)*, 2012.

[6] X. -B. Wei, P. Wang, M. -Q. Liu, and Y. Shi, "Compact wide-stopband lowpass filter using stepped impedance hairpin resonator with radial stubs," *IEE Electron. Lett.,* vol. 47, no. 15, pp. 862-863, July 2011.

[7] J. -P. Wang, H. -F. Cui, and G. Zhang, "Design of a compact microstrip lowpass filter with ultra-wide stopband," *IEE Electron. Lett.,* vol. 48, no. 14, pp. 854-856, July 2012.

[8] A. Bouteidar, A. Batmanov, A. Omar, and E. Burte, "Design of compact low-pass filter using cascaded arrowhead-DGS and multilayer-technique," *Asia-Pacific Microwave Conf.,* pp. 1-4, Dec. 2008.

[9] S. Rehman, A. F. Sheta, and M. A. Alkanhal, "Compact bandpass filters with bandwidth control using defected ground structure (DGS)," *Appl. Comp. Electro. Society (ACES) Journal,* vol. 26, no. 7, pp. 624-630, July 2010.

[10] F. Karshenas, A. R. Mallahzadeh, and J. Rashed-Mohassel, "Size reduction and harmonic suppression of parallel coupled-line bandpass filters using defected ground structure," *Appl. Comp. Electro. Society (ACES) Journal*, vol. 25, no. 2, pp. 149-155, Feb. 2010.

[11] M. Hayati, H. Asadbeigi and A. Sheikhi "Microstrip lowpass filter with high and wide rejection band," *IEE Electron. Lett.,* vol. 48, no. 19, pp. 1217-1219, Sep. 2012.

Yan Dou received the B.Sc. degree in Electronics and Information Engineering from Anhui University, Hefei, China, in 2011. She is currently working toward the Master's degree in Electromagnetic Field and Microwave Technology in NJUST. Her research interest is the design of miniaturized high performance microwave passive device.

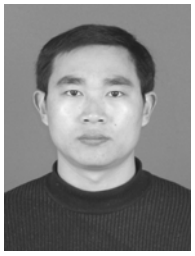

Jianpeng Wang received the M.Sc. and Ph.D. degree from UESTC, Chengdu, China, in 2004, and 2007, respectively, both in Electronic Engineering. Since January 2008, he has been with the Ministerial Key Laboratory of JGMT, School of Electronic and Optical Engineering, NJUST, where he is currently an Associate Professor. His research interests include the high performance microwave/millimeter-wave passive components, circuits and systems realized on PCB, LTCC, etc.

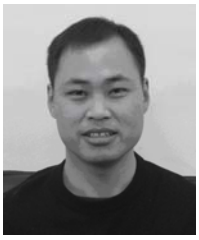

Haifei Cui received the B.Sc. degree in Electronics and Information Engineering from Anhui University, Hefei, China, in 2008. He is currently working toward the Ph.D. degree in Electromagnetic Field and Microwave Technology in NJUST. His research interest is the design of miniaturized high performance microwave passive device.

Jia-Lin Li received the M.Sc. degree from UESTC, Chengdu, China, in 2004, and the Ph.D. degree from the City University of Hong Kong, Hong Kong, in 2009, both in Electronic Engineering. Since Sept. 2009, he has been with the Institute of Applied Physics, School of Physical Electronics, UESTC, where he is currently a Professor. His research interests include the high performance active/passive microwave/millimeter-wave antennas, circuits and systems realized on PCB, multilayer PCB, LTCC, etc.

2013 INSTITUTIONAL MEMBERS

DTIC-OCP LIBRARY
8725 John J. Kingman Rd, Ste 0944
Fort Belvoir, VA 22060-6218

AUSTRALIAN DEFENCE LIBRARY
Northcott Drive
Canberra, A.C.T. 2600 Australia

BEIJING BOOK CO, INC
701 E Linden Avenue
Linden, NJ 07036-2495

DARTMOUTH COLLEGE
6025 Baker/Berry Library
Hanover, NH 03755-3560

DSTO EDINBURGH
AU/33851-AP, PO Box 830470
Birmingham, AL 35283

SIMEON J. EARL – BAE SYSTEMS
W432A, Warton Aerodome
Preston, Lancs., UK PR4 1AX

ENERGY KEN LIBRARY
PO Box 300613
Jamaica, NY, 11430

ENGINEERING INFORMATION, INC
PO Box 543
Amsterdam, Netherlands 1000 Am

ETSE TELECOMUNICACION
Biblioteca, Campus Lagoas
Vigo, 36200 Spain

GA INSTITUTE OF TECHNOLOGY
EBS-Lib Mail code 0900
74 Cherry Street
Atlanta, GA 30332

TIMOTHY HOLZHEIMER
Raytheon
PO Box 1044
Rockwall, TX 75087

HRL LABS, RESEARCH LIBRARY
3011 Malibu Canyon
Malibu, CA 90265

IEE INSPEC
Michael Faraday House
6 Hills Way
Stevenage, Herts UK SG1 2AY

INSTITUTE FOR SCIENTIFIC INFO.
Publication Processing Dept.
3501 Market St.Philadelphia, PA
19104-3302

LIBRARY – DRDC OTTAWA
3701 Carling Avenue
Ottawa, Ontario, Canada K1A OZ4

LIBRARY of CONGRESS
Reg. Of Copyrights
Washington DC, 20559

LINDA HALL LIBRARY
5109 Cherry Street
Kansas City, MO 64110-2498

MISSOURI S&T
400 W 14th Street
Rolla, MO 56409

MIT LINCOLN LABORATORY
244 Wood Street
Lexington, MA 02420

NATIONAL CHI NAN UNIVERSITY
Lily Journal & Book Co, Ltd
20920 Glenbrook Drive
Walnut, CA 91789-3809

JOHN NORGARD
UCCS
20340 Pine Shadow Drive
Colorado Springs, CO 80908

OSAMA MOHAMMED
Florida International University
10555 W Flagler Street
Miami, FL 33174

NAVAL POSTGRADUATE SCHOOL
Attn:J. Rozdal/411 Dyer Rd./ Rm 111
Monterey, CA 93943-5101

NDL KAGAKU
C/0 KWE-ACCESS
PO Box 300613 (JFK A/P)
Jamaica, NY 11430-0613

OVIEDO LIBRARY
PO BOX 830679
Birmingham, AL 35283

DAVID PAULSEN
E3Compliance
1523 North Joe Wilson Road
Cedr Hill, TX 75104-1437

PENN STATE UNIVERSITY
126 Paterno Library
University Park, PA 16802-1808

DAVID J. PINION
1122 E Pike Street #1217
SEATTLE, WA 98122

KATHERINE SIAKAVARA
Gymnasiou 8
Thessaloniki, Greece 55236

SWETS INFORMATION SERVICES
160 Ninth Avenue, Suite A
Runnemede, NJ 08078

YUTAKA TANGE
Maizuru Natl College of Technology
Maizuru, Kyoto, Japan 625-8511

TIB & UNIV. BIB. HANNOVER
Welfengarten 1B
Hannover, Germany 30167

UEKAE
PO Box 830470
Birmingham, AL 35283

UNIV OF CENTRAL FLORIDA
4000 Central Florida Boulevard
Orlando, FL 32816-8005

UNIVERSITY OF COLORADO
1720 Pleasant Street, 184 UCB
Boulder, CO 80309-0184

UNIVERSITY OF KANSAS – WATSON
1425 Jayhawk Blvd 210S
Lawrence, KS 66045-7594

UNIVERSITY OF MISSISSIPPI
JD Williams Library
University, MS 38677-1848

UNIVERSITY LIBRARY/HKUST
Clear Water Bay Road
Kowloon, Honk Kong

CHUAN CHENG WANG
8F, No. 31, Lane 546
MingCheng 2nd Road, Zuoying Dist
Kaoshiung City, Taiwan 813

THOMAS WEILAND
TU Darmstadt
Schlossgartenstrasse 8
Darmstadt, Hessen, Germany 64289

STEVEN WEISS
US Army Research Lab
2800 Powder Mill Road
Adelphi, MD 20783

YOSHIHIDE YAMADA
NATIONAL DEFENSE ACADEMY
1-10-20 Hashirimizu
Yokosuka, Kanagawa,
Japan 239-8686

APPLIED COMPUTATIONAL ELECTROMAGNETICS SOCIETY JOURNAL
http://www.aces-society.org

INFORMATION FOR AUTHORS

PUBLICATION CRITERIA

Each paper is required to manifest some relation to applied computational electromagnetics. **Papers may address general issues in applied computational electromagnetics, or they may focus on specific applications, techniques, codes, or computational issues.** While the following list is not exhaustive, each paper will generally relate to at least one of these areas:

1. **Code validation.** This is done using internal checks or experimental, analytical or other computational data. Measured data of potential utility to code validation efforts will also be considered for publication.

2. **Code performance analysis.** This usually involves identification of numerical accuracy or other limitations, solution convergence, numerical and physical modeling error, and parameter tradeoffs. However, it is also permissible to address issues such as ease-of-use, set-up time, run time, special outputs, or other special features.

3. **Computational studies of basic physics.** This involves using a code, algorithm, or computational technique to simulate reality in such a way that better, or new physical insight or understanding, is achieved.

4. **New computational techniques** or new applications for existing computational techniques or codes.

5. **"Tricks of the trade"** in selecting and applying codes and techniques.

6. **New codes, algorithms, code enhancement, and code fixes.** This category is self-explanatory, but includes significant changes to existing codes, such as applicability extensions, algorithm optimization, problem correction, limitation removal, or other performance improvement. **Note: Code (or algorithm) capability descriptions are not acceptable, unless they contain sufficient technical material to justify consideration.**

7. **Code input/output issues.** This normally involves innovations in input (such as input geometry standardization, automatic mesh generation, or computer-aided design) or in output (whether it be tabular, graphical, statistical, Fourier-transformed, or otherwise signal-processed). Material dealing with input/output database management, output interpretation, or other input/output issues will also be considered for publication.

8. **Computer hardware issues.** This is the category for analysis of hardware capabilities and limitations of various types of electromagnetics computational requirements. Vector and parallel computational techniques and implementation are of particular interest.

Applications of interest include, but are not limited to, antennas (and their electromagnetic environments), networks, static fields, radar cross section, inverse scattering, shielding, radiation hazards, biological effects, biomedical applications, electromagnetic pulse (EMP), electromagnetic interference (EMI), electromagnetic compatibility (EMC), power transmission, charge transport, dielectric, magnetic and nonlinear materials, microwave components, MEMS, RFID, and MMIC technologies, remote sensing and geometrical and physical optics, radar and communications systems, sensors, fiber optics, plasmas, particle accelerators, generators and motors, electromagnetic wave propagation, non-destructive evaluation, eddy currents, and inverse scattering.

Techniques of interest include but not limited to frequency-domain and time-domain techniques, integral equation and differential equation techniques, diffraction theories, physical and geometrical optics, method of moments, finite differences and finite element techniques, transmission line method, modal expansions, perturbation methods, and hybrid methods.

Where possible and appropriate, authors are required to provide statements of quantitative accuracy for measured and/or computed data. This issue is discussed in "Accuracy & Publication: Requiring, quantitative accuracy statements to accompany data," by E. K. Miller, *ACES Newsletter*, Vol. 9, No. 3, pp. 23-29, 1994, ISBN 1056-9170.

SUBMITTAL PROCEDURE

All submissions should be uploaded to ACES server through ACES web site (http://www.aces-society.org) by using the upload button, journal section. Only pdf files are accepted for submission. The file size should not be larger than 10MB, otherwise permission from the Editor-in-Chief should be obtained first. Automated acknowledgment of the electronic submission, after the upload process is successfully completed, will be sent to the corresponding author only. It is the responsibility of the corresponding author to keep the remaining authors, if applicable, informed. Email submission is not accepted and will not be processed.

EDITORIAL REVIEW

In order to ensure an appropriate level of quality control, papers are peer reviewed. They are reviewed both for technical correctness and for adherence to the listed guidelines regarding information content and format.

PAPER FORMAT

Only camera-ready electronic files are accepted for publication. The term **"camera-ready" means that the material is neat, legible, reproducible, and in accordance with the final version format listed below.**

The following requirements are in effect for the final version of an ACES Journal paper:

1. The paper title should not be placed on a separate page.

The title, author(s), abstract, and (space permitting) beginning of the paper itself should all be on the first page. The title, author(s), and author affiliations should be centered (center-justified) on the first page. The title should be of font size 16 and bolded, the author names should be of font size 12 and bolded, and the author affiliation should be of font size 12 (regular font, neither italic nor bolded).

2. An abstract is required. The abstract should be a brief summary of the work described in the paper. It should state the computer codes, computational techniques, and applications discussed in the paper (as applicable) and should otherwise be usable by technical abstracting and indexing services. The word "Abstract" has to be placed at the left margin of the paper, and should be bolded and italic. It also should be followed by a hyphen (—) with the main text of the abstract starting on the same line.

3. All section titles have to be centered and all the title letters should be written in caps. The section titles need to be numbered using roman numbering (I. II. ….)

4. Either British English or American English spellings may be used, provided that each word is spelled consistently throughout the paper.

5. Internal consistency of references format should be maintained. As a guideline for authors, we recommend that references be given using numerical numbering in the body of the paper (with numerical listing of all references at the end of the paper). The first letter of the authors' first name should be listed followed by a period, which in turn, followed by the authors' complete last name. Use a coma (,) to separate between the authors' names. Titles of papers or articles should be in quotation marks (" "), followed by the title of journal, which should be in italic font. The journal volume (vol.), issue number (no.), page numbering (pp.), month and year of publication should come after the journal title in the sequence listed here.

6. Internal consistency shall also be maintained for other elements of style, such as equation numbering. Equation numbers should be placed in parentheses at the right column margin. All symbols in any equation have to be defined before the equation appears or right immediately following the equation.

7. The use of SI units is strongly encouraged. English units may be used as secondary units (in parentheses).

8. Figures and tables should be formatted appropriately (centered within the column, side-by-side, etc.) on the page such that the presented data appears close to and after it is being referenced in the text. When including figures and tables, all care should be taken so that they will appear appropriately when printed in black and white. For better visibility of paper on computer screen, it is good to make color figures with different line styles for figures with multiple curves. Colors should also be tested to insure their ability to be distinguished after black and white printing. Avoid the use of large symbols with curves in a figure. It is always better to use different line styles such as solid, dotted, dashed, etc.

9. A figure caption should be located directly beneath the corresponding figure, and should be fully justified.

10. The intent and meaning of all text must be clear. For authors who are not masters of the English language, the ACES Editorial Staff will provide assistance with grammar (subject to clarity of intent and meaning). However, this may delay the scheduled publication date.

11. Unused space should be minimized. Sections and subsections should not normally begin on a new page.

ACES reserves the right to edit any uploaded material, however, this is not generally done. It is the author(s) responsibility to provide acceptable camera-ready files in pdf and MSWord formats. Incompatible or incomplete files will not be processed for publication, and authors will be requested to re-upload a revised acceptable version.

COPYRIGHTS AND RELEASES

Each primary author must execute the online copyright form and obtain a release from his/her organization vesting the copyright with ACES. Both the author(s) and affiliated organization(s) are allowed to use the copyrighted material freely for their own private purposes.

Permission is granted to quote short passages and reproduce figures and tables from and ACES Journal issue provided the source is cited. Copies of ACES Journal articles may be made in accordance with usage permitted by Sections 107 or 108 of the U.S. Copyright Law. This consent does not extend to other kinds of copying, such as for general distribution, for advertising or promotional purposes, for creating new collective works, or for resale. The reproduction of multiple copies and the use of articles or extracts for commercial purposes require the consent of the author and specific permission from ACES. Institutional members are allowed to copy any ACES Journal issue for their internal distribution only.

PUBLICATION CHARGES

All authors are allowed for 8 printed pages per paper without charge. Mandatory page charges of $75 a page apply to all pages in excess of 8 printed pages. Authors are entitled to one, free of charge, copy of the printed journal issue in which their paper was published. Additional reprints are available for $50. Requests for additional re-prints should be submitted to the managing editor or ACES Secretary.

Corresponding author is required to complete the online form for the over page charge payment right after the initial acceptance of the paper is conveyed to the corresponding author by email.

ACES Journal is abstracted in INSPEC, in Engineering Index, DTIC, Science Citation Index Expanded, the Research Alert, and to Current Contents/Engineering, Computing & Technology.